Akita University

Descriptive Petrology and Geochemical Study of New Basalt Volcanic Activity in Palawan Island, Northern Province, Philippines

フィリピン、北部パラワン島における新期玄武岩質火山活動の記載岩石学及び地球化学的研究--

2020

James Cesar Avisado Refran

レフラン ジェームス セザー アヴィサド

6517108

秋田大学大学院

国際資源学研究科

資源地球科学専攻

Abstract

Manguao Basalt is a basalt-basaltic andesite lava flow field found on the northeast end of Palawan Island, Philippines. The relatively stable nature of the Palawan Continental Block seemingly contradicts the presence of the geomorphologically young lava flow field. This study investigates the occurrence and origin of Manguao Basalt, and its relation to the evolution of the Palawan microcontinent.

Good exposures of the Manguao Basalt lava flow field are found nearshore. Lava flow structures and features (i.e., levees, channels, and tumuli) are still intact and observable in several locations. The lava flow is generally blocky and vesicular, with observable phenocrysts and large chert xenoliths. Macroscopic observations of obtained samples show identifiable olivine and pyroxene phenocrysts. Petrographic observations show olivine dominance in the phenocryst assemblage and plagioclase dominance in the groundmass. Pyroxenes are found both in phenocryst and groundmass assemblages. Mineral textures observed from petrography show the earlier formation of pyroxene phenocrysts from olivine. Plagioclase laths, on the other hand, show earlier crystallization from the anhedral groundmass pyroxenes. Volcanic glass fills the interstices between plagioclase and pyroxene, forming intersertal textures. A general overview of the crystallization sequence (pyroxenes → olivine → plagioclase → groundmass pyroxenes) is presented.

Major element chemistry from bulk-rock compositions characterizes the Manguao Basalt as subalkaline and tholeiitic. Bivariate diagrams show the fractionation of ferromagnesian minerals (i.e., olivine and pyroxenes) but limited fractionation in later-formed minerals (i.e., plagioclase). Total iron over magnesium (FeO^t/MgO) versus silica (SiO_2) plots (Miyashiro, 1974) of Manguao Basalt shows 'straddling' tholeiite and calc-alkaline character. The presence of the chert xenoliths, however, may have affected bulk silica concentrations, shifting the plots towards the calc-alkaline field. AFM ternary plots show a diagnostic early iron enrichment, reflecting a tholeiitic trend. Trace element chemistry confirms the early ferromagnesian fractionation from nickel and cobalt trends. Tectonic discrimination diagrams of Manguao Basalt show resemblance with different basalts from other known tectonic settings (i.e.,

continental flood basalts, island-arc basalts, continental-arc basalts, and within-plate basalts). However, the association of Manguao Basalt with ocean-island basalts (OIB) or mid-ocean ridge basalts (MORB) appeared inconclusive [i.e., plotting outside MORB-OIB array defined by Pearce (2008)]. These inconsistencies that accompany the trace element discrimination diagrams have been pointed out by Li et al. (2015). Nevertheless, their utility is in constraining the possible tectonic processes that influence melt generation and evolution. Trace element patterns in spider diagrams show the enriched melt character of Manguao Basalt. Characteristic Nb-Ta depletion is absent for Manguao Basalt, indicating source melting that is unrelated to subduction. Positive anomalies in continent-derived trace elements (e.g., Th and Pb) are observable and consistent in any spider diagram presented (Primitive Mantle-, MORB-, NMORB-, EMORB-, and OIB-normalized).

Mineral chemistry data (olivine, orthopyroxene, clinopyroxene, and plagioclase) confirm the crystallization sequence inferred from petrography. The highest Mg# was obtained from orthopyroxene phenocrysts (Mg# > 80). Calculations using orthopyroxene barometer also yielded the highest pressures (~5 kbar), while orthopyroxene thermometers (i.e., opx-liquid) yielded the highest temperatures (~1260 °C). These obtained pressure and temperature conditions were used as benchmarks for simulations of source melting and crystallization.

Melting simulations of different upper mantle sources (e.g., fertile and depleted) were done using the MELTS program. Equilibrium and fractional melting from depressurization (15 kbar → 5 kbar; T = 1350 °C and at QFM buffer) of any mantle source produce liquids that are saturated in pyroxene components. Subsequent crystallization of melt, while being at equilibrium with source and at elevated pressures (~5 kbar) produce orthopyroxenes with similar compositions to orthopyroxenes in Manguao Basalt. The formation of olivine and the rest of the groundmass cannot be reconciled with any of the simulations due to the assumption of complete crystallization at depth. The model for magmatic underplating is presented here as a possible setup for the origin of Manguao Basalt.

Table of Contents

Akita University

List of Tables

List of Figures

Akita University

Akita University

Chapter 1: Introduction

Volcanism has always played an integral part in understanding the tectonics and geologic history of a region. Conversely, tectonics have simplified our understanding of volcanism because of the growing scientific knowledge in mantle dynamics, melt production, and crystallization. Thus, studies on volcanic phenomena are often explained from the perspectives of regional tectonics and geologic history.

Most of young and recent volcanic events in the Philippines have always been associated with nearby subduction zones bounding the archipelago (Aurelio, 2000). As such, volcanism in the country is often connected with a nearby active trench. There are few cases, however, where a magmatic activity is not associated with a recognizable subduction zone (i.e., Central Mindanao lavas; Sajona et al. 2000). Hence, such peculiar volcanic events merit reinvestigation and thorough study.

Magmatic arcs in the Philippines run from north (Batanes Group of Islands) to south (Cotabato Arc and East Philippine Arc; Fig. 1), within a region of active volcanism and tectonics called the Philippine Mobile Belt (PMB; Aurelio, 2000). Active and potentially active volcanic centers, including their corresponding effusive products and seismic activity, are mostly found within the PMB. In contrast to such manifestations of unrest within PMB, the western region of Palawan Island seemingly displays quiescence. Geologically distinct from the rest of the archipelago, the Palawan Continental Block (PCB) exhibits fewer magmatic units, limited seismic activity compared to PMB, and absence of nearby active trench. Notable igneous units found in the region are the Early Oligocene Palawan Ophiolite in the south (Encarnación et al., 2001), the Eocene Central Palawan Granite (Suggate et al., 2014), and the Miocene Capoas/Kapoas Granite (Suggate et al., 2014).

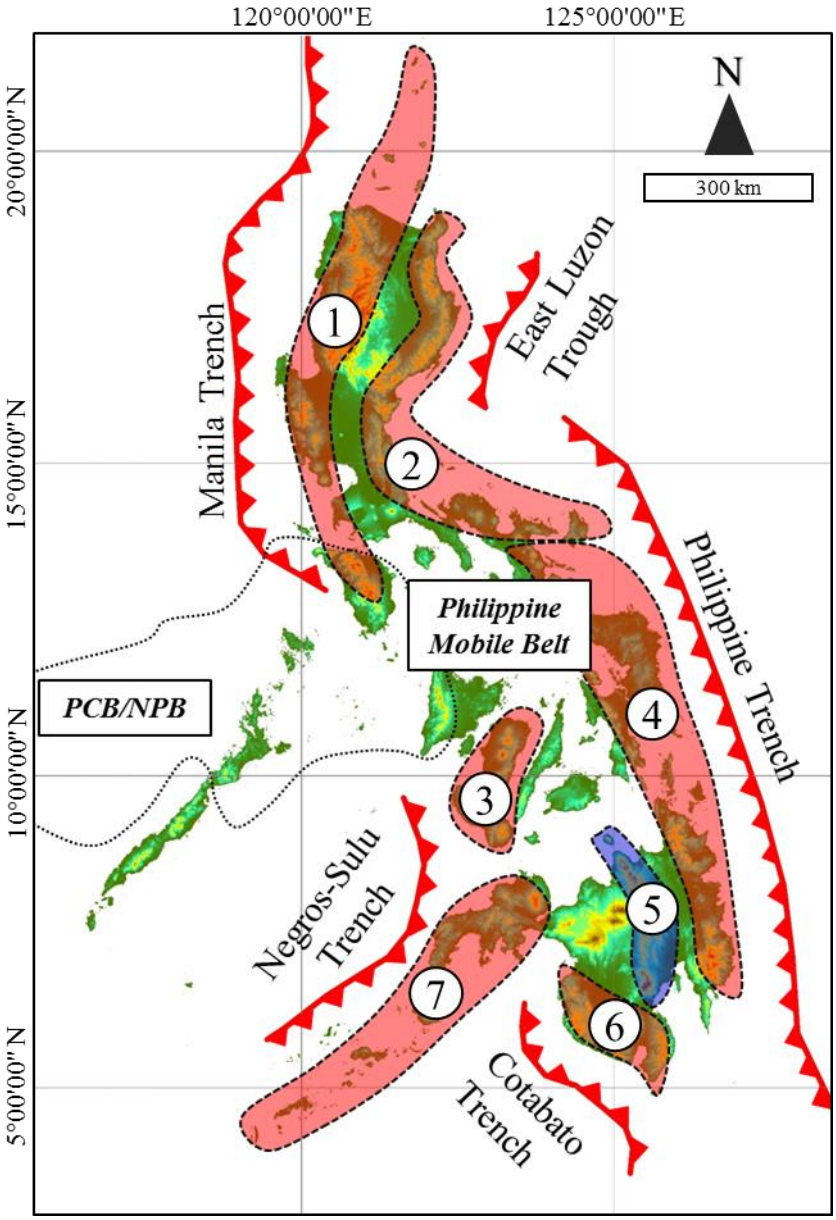

Figure 1. Simplified tectonic map of the Philippines showing the distribution of volcanic arcs (red shaded regions in dashed outline) and adjacent active trenches. Tectonic features were modified from Magro et al. (2013) and Aurelio (2000). ① Luzon Central Cordillera Arc is controlled by activity of the Manila Trench in the west. ② Volcanic activity in the northern and southern Sierra Madre-Catanduanes are related to the Philippine Trench in the east and former activity of the East Luzon Trough. ③ The Negros Arc is related to the Negros-Sulu Trench. ④ The East Philippine Arc is related to the Philippine Trench. ⑤ Magmatic activity in the Central Mindanao Arc (shaded blue) is related to a completely subducted oceanic slab with partial influence from the activity of the Philippine Trench. ⑥ The Cotabato Arc is related to the Cotabato Trench. ⑦ The Sulu-Zamboanga Arc is related to Negros-Sulu Trench. Boundaries of Palawan Continental Block were derived from Liu et al. (2014). Base Philippine image was generated from Shuttle Radar Topography Mission (SRTM; 90-m resolution) data from philgis.org.

East of Mt. Capoas, overlying the Permian Liminangcong Chert (Peña, 2008), a large basaltic lava flow field exposure (Manguao Basalt) can be found lining the coast of Calauag Bay (Fig. 2). Lava flow structures are exceptionally preserved for an initially reported Plio-Pleistocene age. The absence of

active trench surrounding the Palawan region challenges the longstanding notion of young Philippine volcanic activity being primarily driven by subduction.

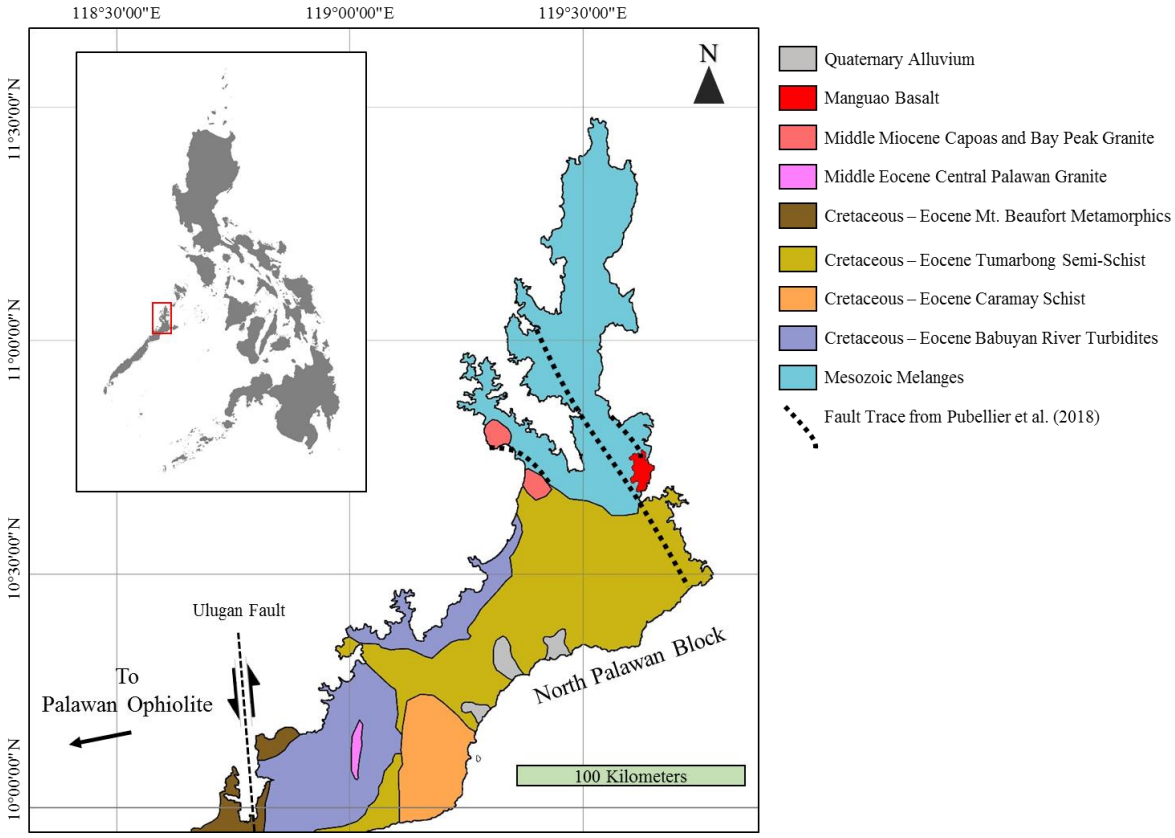

Figure 2. Simplified geologic map of North Palawan Island showing the distribution of lithologies with continental affinity. Red, light red, and pink indicate igneous units. Manguao Basalt is assigned with a Plio-Pleistocene age. Other magmatic units include the Middle Miocene Capoas and Bay Peak Granite, and the Middle Eocene Central Palawan Granite. Cretaceous-Eocene units included in the map are members of the Palawan Ophiolite. The Ulugan Fault is a structural boundary separating the Palawan Continental Block from the Palawan Ophiolite. Map reconstructed from Suggate et al. (2014) and Almasco et al. (2000). Base image generated from SRTM DEM (90-m resolution from philgis.org).

Scientific Problem

The occurrence and origin of Manguao Basalt strikingly differ from other young and recent lava units found in the Philippines. This thesis aims to understand the origin of the basaltic lava, to characterize its possible mantle source, and to give insights into the tectonic influences that induce melt generation beneath the Palawan microcontinent. In addition, the connection of the distinct magmatic phenomena with the region's tectonic setup is not yet fully understood. Therefore, the insights provided in this study will be useful in linking the PCB's geologic history to the bigger context of the South China Sea evolution.

Objectives of the Study

This thesis aims to produce a more detailed petrographic and geochemical record of Manguao Basalt, as well as to contribute to the further understanding of the mantle state beneath the PCB. The results of this study also serve as approach to describing and characterizing Philippine magmatic events that are unrelated to any present subduction zone.

While the idea of magma generation beneath Palawan microcontinent is not a common theme in the context of Philippine geology, this study will provide new insights into the complex geologic history of the Palawan microcontinent. The results from this study will further enrich our understanding of the origin, processes, and influences of magmatic events in Palawan.

Significance of the Study

The study provides detailed information about the occurrence and origin of Manguao Basalt. The ideas presented in this study will serve as foundation for succeeding investigations on magmatism in the Palawan microcontinent, and help link the geologic history of PCB with the South China Sea.

Outline of Thesis

The first chapter of this manuscript presents the introductory overview of the thesis problem, the general scientific background, the objectives, and the significance of the study. Chapter 2 summarizes previous reports on the tectonic setting of the Philippines, the geology of Palawan Island, and the occurrence of Manguao Basalt. The ideas presented in chapter 2 act as framework for the discussions presented in this thesis. The succeeding chapters are significant and relevant ideas to the study that have been submitted for publication or are considered as key chapters for the overall discussion in the manuscript. Chapter 3 presents the bulk-rock chemistry and petrographic analyses of samples taken from the lava field. Discussions on the major and trace element chemistry, classification, and the corresponding implications on the tectonic setting are included in this chapter. Chapter 4 discusses further the details regarding crystallization, magmatic conditions, melt source, and mineral chemistry. Ideas presented in chapter 4 were submitted to the Journal of Mineralogical and Petrological Sciences (under review).

Chapter 5 presents the significant findings of this thesis, including scientific ideas that will be carried unto future investigations of Manguao Basalt.

References

Almasco, J.N., Rodolfo, K., Fuller, M. and Frost, G. (2000) Paleomagnetism of Palawan, Philippines. Journal of Asian Earth Sciences, 18, 369–389.

Aurelio, M. (2000) Tectonics of the Philippines revisited. Journal of the Geological Society of the Philippines, 55, 119–183.

Encarnación, J., Fernandez, D. and Mattinson, J. (2001) Subduction Initiation by Extrusion Tectonics? Evidence from the Palawan Ophiolite, Philippines. American Geophysical Union Fall Meeting Abstracts.

Liu, W.N., Li, C.F., Li, J., Fairhead, D. and Zhou, Z. (2014) Deep structures of the Palawan and Sulu Sea and their implications for opening of the South China Sea. Marine and Petroleum Geology, 58, 721–735.

Magro, G., Gherardi, F. and Bayon, F.E. (2013) Noble and reactive gases of Palinpinon geothermal field (Philippines): Origin, reservoir processes and geodynamic implications. Chemical Geology, 339, 4–15.

Peña, R.E. (2008) Lexicon of Philippine Stratigraphy. The Geological Society of the Philippines, pp. 364, Mandaluyong, Philippines.

Sajona, F.G., Maury, R.C., Pubellier, M., Leterrier, J., Bellon, H. and Cotten, J. (2000) Magmatic source enrichment by slab-derived melts in a young post-collision setting, central Mindanao (Philippines). Lithos, 54, 173–206.

Suggate, S.M., Cottam, M.A., Hall, R., Sevastjanova, I., Forster, M.A., White, L.T., Armstrong, R.A., Carter, A. and Mojares, E. (2014). South China continental margin signature for sandstones and granites from Palawan, Philippines. Gondwana Research, 26, 699–718.

Chapter 2: Background of the Study and Lava Field Occurrence

Tectonic Setting of the Philippines

The Philippine archipelago is the product of collision of three major tectonic plates: Eurasia, Pacific, and Indo-Australia (Fig. 3). Subduction zones that line the boundaries of these collisions induce active volcanism and fault movement in the archipelago. In general, the Philippines is divided into two distinct geologic units: (1) the Philippine Mobile Belt (PMB), and (2) the Palawan Continental Block (PCB). The Philippine Mobile Belt represents the seismically active block, while the Palawan Continental Block represents the aseismic region (Yumul et al., 2009). Magmatic arcs are pervasive in the Philippine Mobile Belt because of the activity in nearby subduction zones. Ancient magmatic arcs, such as the Cretaceous dioritic rocks in Cebu (Walther et al., 1981 in Aurelio, 2000) display mountain chains that are generally less prominent than younger (e.g., Oligo-Miocene) arcs along Central Luzon and East Mindanao (Aurelio, 2000). On the other hand, recent Plio-Quaternary volcanic arcs reflect the trends of the ongoing subduction. Aurelio in 2000 defined five distinct active volcanic arcs and their related subduction zones:

1. Luzon Arc: related to the southeasterly subduction of the Eurasian Plate along the Manila Trench

2. East-Philippine Arc: related to northwesterly subduction of Philippine Plate along the Philippine Trench

3. Negros-Panay Arc: related to subduction of Sulu Sea along the Negros Trench

4. Sulu-Zamboanga Arc: related to subduction of Sulu Sea along the Sulu Trench

5. Cotabato Arc: related to subduction of Celebes Sea along the Cotabato Trench

It should be noted, however, that even though it appears seemingly efficient to categorize the magmatic arcs in the country based on subduction relation and temporal classification, there are several magmatic events have been identified which are not included in the mentioned categories (e.g., Mt. Apo and

related volcanic cones in Mindanao; Aurelio, 2000). Such peculiar magmatic events need further investigation and study.

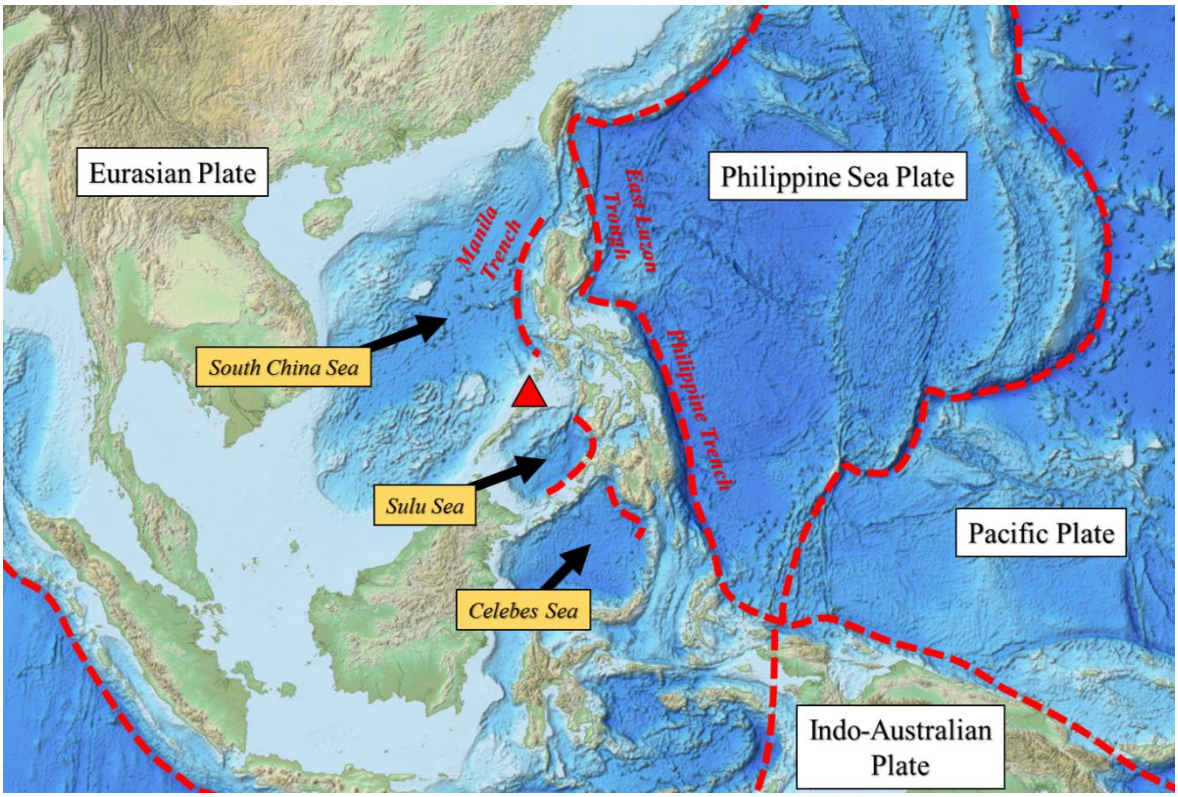

Figure 3. The Philippines and surrounding tectonic features. Boundaries of the major tectonic plates are outlined in red dash. The Philippine Sea Plate subducts westward along the East Luzon Trough and Philippine Trench. The westward subduction forms the East Philippine Arc. The South China Sea, Sulu Sea, and Celebes Sea subduct eastwards and form the western magmatic arcs (Luzon Arc, Negros-Panay Arc, Sulu-Zamboanga, and Cotabato Arc). Location of the study area is marked with a red triangle. Base image from NOAA National Centers for Environmental Information (NOAA-NCEI) is available from https://noaa.maps.arcgis.com

Geology of Palawan Island

Palawan is an island province located on the western side of the Philippine archipelago, separating the South China Sea (SCS) from the Sulu Sea. The island rests on the extended oceanic crust of the Eurasian plate, which separated from the mainland during the opening of the South China Sea (Yumul et al., 2009). The northern half of the island (from Ulugan Bay) is composed of continent-derived sedimentary and metamorphic rocks, while the southern half is dominated by the Palawan Ophiolite (Militante-Matias et al., 2000; Aurelio, 2000; Yumul et al., 2009; Aurelio et al., 2013).

The geologic history of Palawan Island has been heftily summarized in numerous works (e.g., Williams, 1997; Almasco et al., 2000; Aurelio, 2000; Militante-Matias et al., 2000; Yumul et al., 2009; Aurelio et al., 2013; Guan et al., 2016). Upper Paleozoic-Mesozoic cherts, clastics and carbonates, which predate the South China Sea opening, are found on the northeast end of the island (Fig. 4). Rifting of SCS and transport of the Palawan microcontinent southwards (Oligocene-Early Miocene) induced metamorphism of clastic sedimentary rocks and emplaced ophiolitic rocks in the southwestern end. Collision of the transported Palawan block with the Philippine Mobile Belt during the Miocene locked the island close to its present configuration (Aurelio et al. 2013). Plio-Quaternary volcanism, including the emplacement of Manguao Basalt, then followed the collision (Almasco et al., 2000; Aurelio et al., 2013).

No subduction activity can be observed in Palawan Island (i.e. absence of active trenches). Previous subduction activity in Palawan was inferred to have occurred in the Mesozoic (preceding SCS opening; Yumul et al., 2009; Aurelio et al., 2013; Liu et al., 2014) and sometime before the Miocene (i.e. Palawan Trench; Williams, 1997; Aurelio et al., 2013). Nevertheless, the recent tectonic setup of the island, as well as records of earlier magmatism (e.g., Capoas Granite; Encarnación and Mukasa, 1997), do not show direct evidence of subduction influence on post-collision Palawan Island.

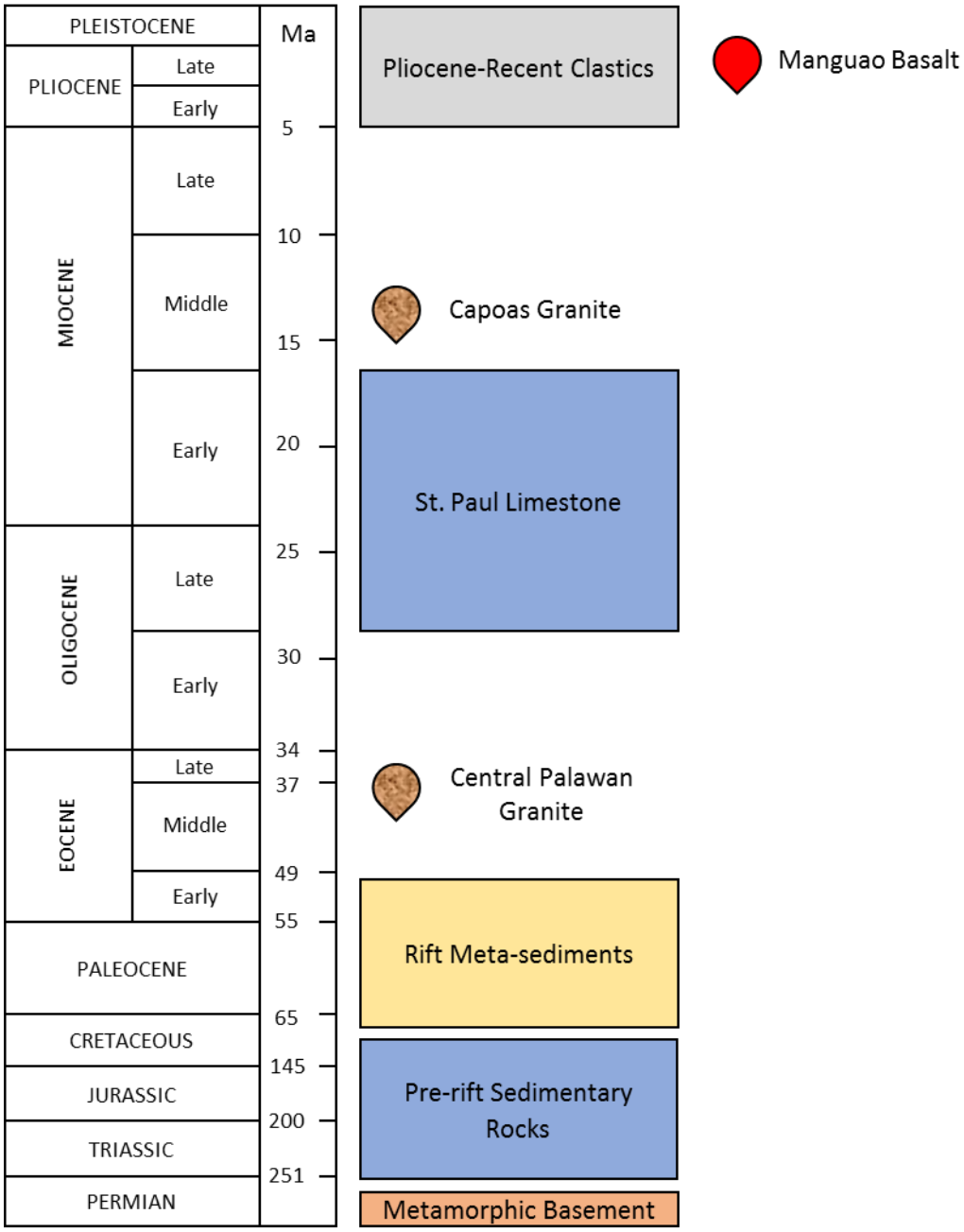

Figure 4. General stratigraphy of the Palawan Continental Block from Peña (2008). Oldest rocks in the region are from Bacuit Formation, which serves as the metamorphic basement (Suggate et al., 2014). Limestones (Minilog and Coron Formation), cherts (Liminangcong), and clastic sedimentary rocks (Guinlo) dominate pre-rift sedimentary sequences. Boayan Formation (Babuyan River Turbidite), Conception Phyllite, and Caramay Schist represent the rift-related sedimentation and metamorphism in the region (Suggate et al., 2014). Central Palawan and Capoas/Kapoas Granite represent intrusions in a "post-rifting, non-collisional tectonic setting unrelated to any subduction zone" (Encarnación and Mukasa, 1997; as in Suggate et al., 2014). Manguao Basalt is assigned a Plio-Pleistocene age.

Manguao Basalt

The Manguao Basalt is a Plio-Pleistocene (reported; MMAJ-JICA, 1990; Peña, 2008) basaltic lava flow field located on the northeastern edge of Palawan Island. Formerly known as Manguao Volcanics, Manguao Basalt consists of porphyritic vesicular basalts, shales, siltstones, conglomerates, and related pyroclastic rocks. Exposures of the lava flow are observable southeast of Lake Manguao (Fig. 5), in the municipality of Taytay, Palawan, Philippines. The lava field is well-exposed in low-lying areas, with observable phenocrysts of olivine and pyroxene (Peña, 2008).

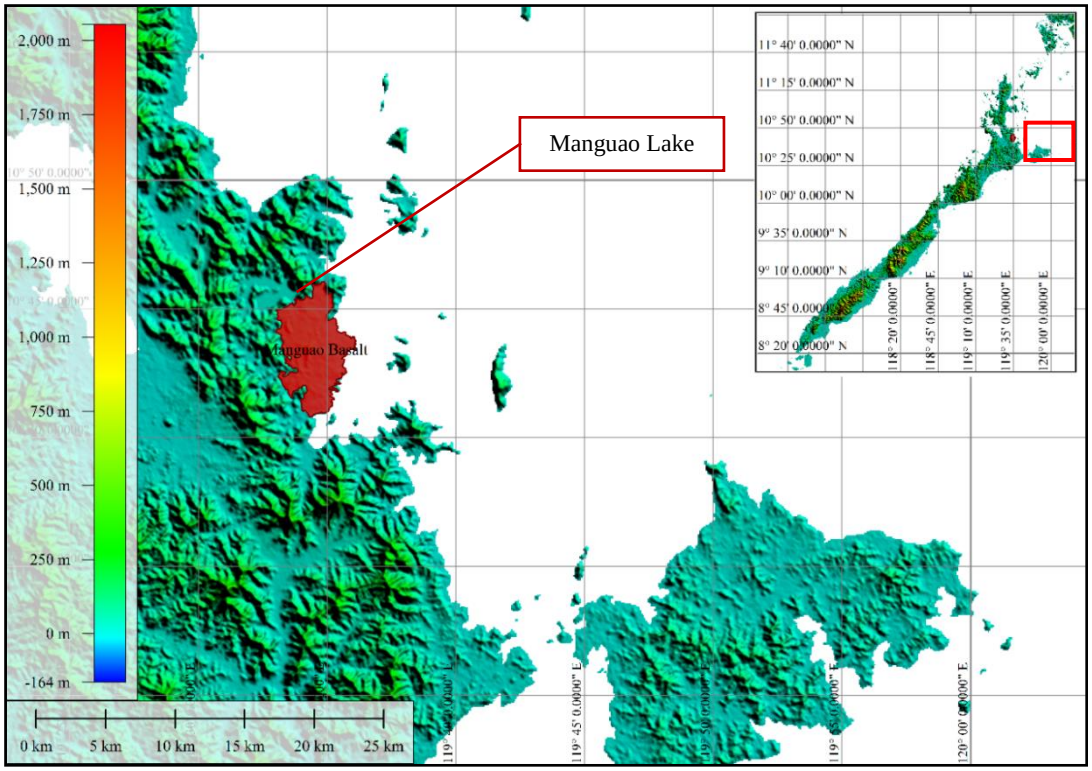

Figure 5. Terrain map showing the location of the Manguao Basalt lava field (red shaded region). Immediate northwest of the lava field is Manguao Lake. A noticeable contrast in relief can be observed between the chert hills to the west and the Manguao Basalt lava field.

Initial reports and studies on the lava field are only limited to its occurrence and its relation to the regional stratigraphy of the northern Palawan block (Peña, 2008). Examining melt generation beneath Palawan, investigating the crystallization of the melt, and further linking the occurrence of Manguao Basalt to the geologic history of Palawan (and the bigger context of South China Sea) are the significant contributions of this thesis to the greater understanding of magmatic events in the Philippines.

Akita University

References

Almasco, J.N., Rodolfo, K., Fuller, M. and Frost, G. (2000) Paleomagnetism of Palawan, Philippines. Journal of Asian Earth Sciences, 18, 369–389.

Aurelio, M. (2000) Tectonics of the Philippines revisited. Journal of the Geological Society of the Philippines, 55, 119–183.

Aurelio, M.A., Peña, R.E. and Taguibao, K.J.L. (2013) Sculpting the Philippine archipelago since the Cretaceous through rifting, oceanic spreading, subduction, obduction, collision and strike-slip faulting: Contribution to IGMA5000. Journal of Asian Earth Sciences, 72, 102–107.

Encarnación, J. and Mukasa, S.B. (1997) Age and geochemistry of an "anorogenic" crustal melt and implications for I-type granite petrogenesis. Lithos, 42, 1–13.

Guan, D., Ke, X. and Wang, Y. (2016) Basement structures of East and South China Seas and adjacent regions from gravity inversion. Journal of Asian Earth Sciences, 117, 242–255.

Metal Mining Agency of Japan – Japan International Cooperation Agency (MMAJ-JICA). (1990) Report on the Mineral Exploration, Mineral deposits and Tectonics of two contrasting Geologic Environments in the Republic of the Philippines, Terminal report, pp. 83, Tokyo, Japan.

Militante-Matias, P.J., de Leon, M.M. and Marquez, E.J. (2000) Cretaceous environments of the Philippines. Developments in Palaeontology and Stratigraphy, 17, 181–199.

Peña, R.E. (2008) Lexicon of Philippine Stratigraphy. The Geological Society of the Philippines, pp. 364, Mandaluyong, Philippines.

Suggate, S.M., Cottam, M.A., Hall, R., Sevastjanova, I., Forster, M.A., White, L.T., Armstrong, R.A., Carter, A. and Mojares, E. (2014). South China continental margin signature for sandstones and granites from Palawan, Philippines. Gondwana Research, 26, 699–718.

Walther, H.W., Forster, H., Harre, W., Kreuzer, H., Lenz, H., Muller, P. and Raschka, H. (1981) Early Cretaceous porphyry copper mineralization on Cebu island, Philippines, dated with K-Ar and Sb-Sr methods. Geologische Jahrbuch Reihe D, 48, 21-35.

Williams, H.H. (1997) Play concepts-northwest Palawan, Philippines. Journal of Asian Earth Sciences, 15, 251–273.

Yumul, G.P., Dimalanta, C.B., Marquez, E.J. and Queaño, K. L. (2009) Onland signatures of the Palawan microcontinental block and Philippine mobile belt collision and crustal growth process: A review. Journal of Asian Earth Sciences, 34, 610–62.

Chapter 3: Petrography and Geochemistry

Introduction

This chapter includes data from petrographic, geochemical, and petrochemical analyses done on Manguao Basalt samples. Information in this chapter are essential for setting the geological context (i.e., non-subduction influence for melt generation) that is critical for several assumptions made in the succeeding chapters. Key points presented here also serve as groundwork for discussion of the tectonic framework of Palawan Continental Block, and its relation to the South China Sea evolution.

Methodology

Samples from the Manguao Basalt lava field were acquired during fieldwork conducted in 2018. Petrographic thin sections were prepared at the Department of Earth Resource Science, Akita University. Petrochemical analyses were done using a scanning electron microscope with energy dispersive spectroscope (SEM-EDS) and an electron probe microanalyzer (EPMA). Modal mineralogy, mineral textures and relationships, and rock textures were observed using a binocular polarizing microscope. Detailed mineral and rock textures, as well as semi-quantitative and quantitative mineral chemistry were done using SEM-EDS (JEOL JSM-IT300 + Oxford EDS detector X-MaxN) and EPMA (JEOL JXA-8800 SuperProbe). Operating conditions of SEM-EDS are at high vacuum conditions, 10 mm working distance, 15 kV accelerating voltage, and probe current of 2.20 nA. Acquisition time of fifty (50) seconds for semi-quantitative point analyses were done on carbon-coated petrographic thin sections (~30 nm thickness at 2.25 g/cm^3 carbon coat density). EPMA operating conditions are at 15.0 kV accelerating voltage, 5 µm probe diameter, and at 20 nA current. Quantitative mineral chemistry analyses of the modal assemblage (e.g., olivine, pyroxenes, plagioclases, and volcanic glass) were obtained using EPMA. A JEOL silicate standards set (for SiO_2, CaO, FeO, Al_2O_3, MgO, TiO_2, MnO, Na_2O, K_2O, Cr_2O_3, and NiO) was used. Weight percent oxide (wt%) totals within 99-101 wt% were included and recorded for stoichiometric, geothermometry, and geobarometry calculations.

Data of bulk-rock major and trace element geochemistry were obtained from samples sent to a commercial testing laboratory (Intertek Testing Services Philippines). Prepared powdered samples were sent for X-ray Fluorescence Spectroscopy (XRF) and Inductively-Coupled Plasma Mass and Optical Emission Spectrometry analyses (ICP-MS/OES). For XRF, a wavelength-dispersive instrumentation Panalytical AxiosMax PW: 4400/40 was used. For ICP-MS/OES, ICP-MS Agilent Technologies 7700x and ICP-OES Agilent Technologies 5100 Radial were used.

Petrography

Manguao Basalt samples are porphyritic and vesicular. Phenocrysts are dominated by olivine, set in a groundmass of plagioclase and pyroxenes. Other coarse-grained units identified are large xenoliths of chert and mineral clusters. Volcanic glass is also observed as blebby, intersertal units in the groundmass.

(1) Olivine

Discernible even at macroscopic observations, olivines only exist in (and dominate; >90%) the phenocryst assemblage (0.5-2.0 mm). Crystals are euhedral to subhedral, some with edges that are partially resorbed. Skeletal texture is also a common feature but is not found in all crystals. Olivine phenocrysts occur as discrete individual units, or as tight cluster of few crystals. Spinel and crystallized melt are commonly found in olivine, but some crystals are free of inclusions.

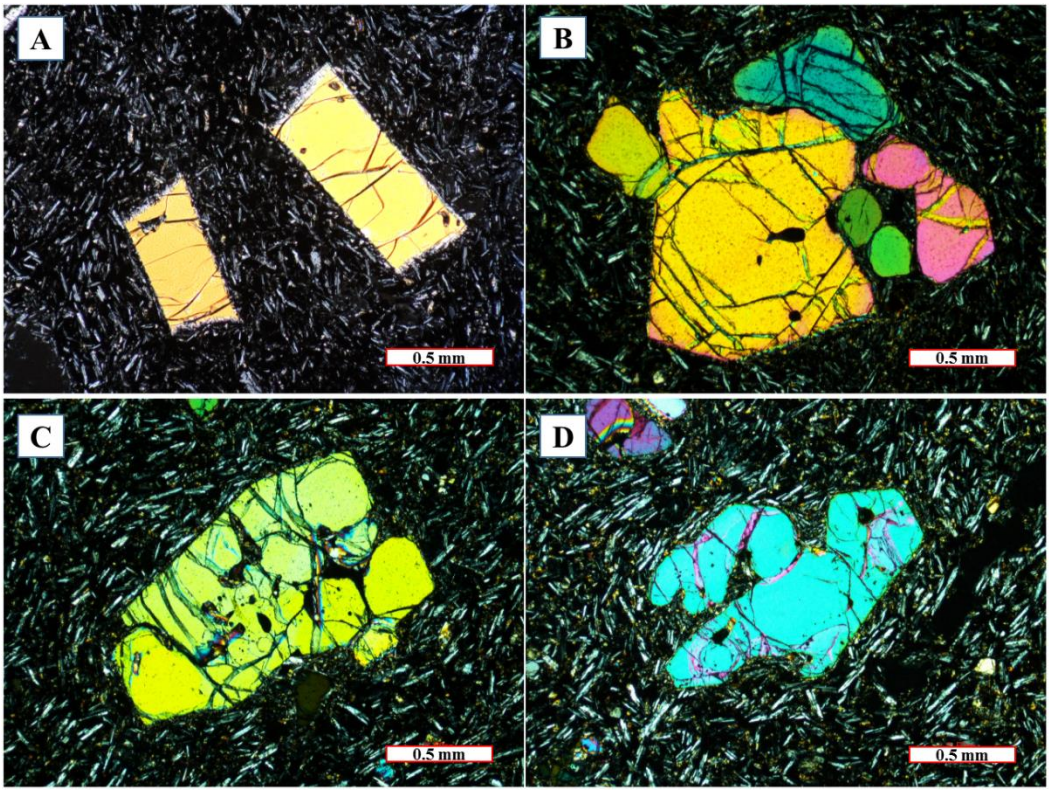

Figure 6. Occurrence of olivine phenocryst in Manguao Basalt. (A) Olivine phenocrysts as individual crystals. (B) Cluster of olivine phenocrysts. (C) Crystal edges of some olivine phenocrysts are partially resorbed. (D) Skeletal and resorbed olivine phenocryst.

(2) Pyroxenes

Pyroxenes can be found as phenocrysts, in distinct clusters, or as components in the groundmass. Some pyroxene phenocrysts are larger (>4.0 mm) than average olivine crystals. Pyroxene clusters are also noticeable in several samples as distinct aggregates of crystals spanning a few millimeters (>4.0 mm) in length. While the large pyroxene phenocrysts commonly occur as rigid individual crystals, the pyroxene clusters appear as bulbous units with volcanic glass and smaller crystals at the center. Groundmass pyroxenes, on the other hand, occur as anhedral-subhedral masses (<0.1 mm) between larger plagioclase laths.

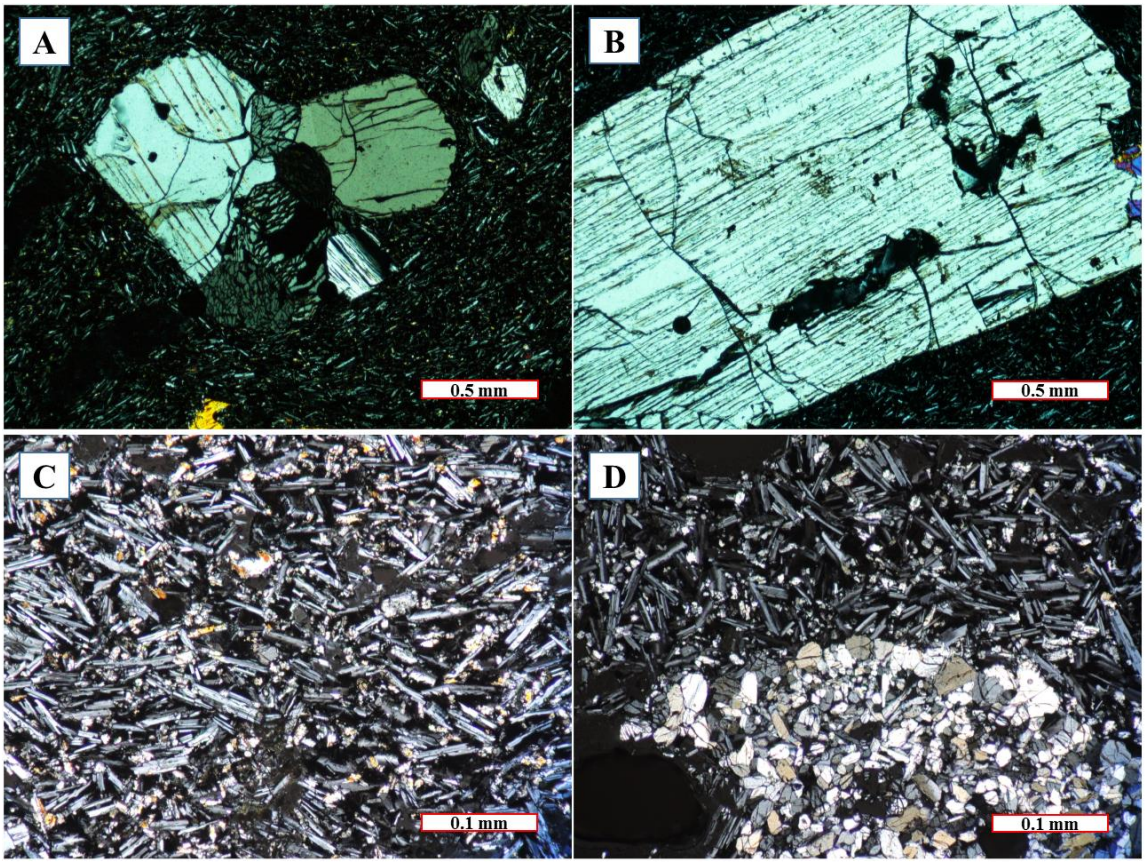

Figure 7.Pyroxene occurrences in Manguao Basalt. (A) Large pyroxene phenocryst in a plagioclase-dominated groundmass. (B) Large single pyroxene phenocryst. (C) Pyroxenes in groundmass exist as anhedral grains between plagioclase laths. (D) Pyroxene cluster in Manguao Basalt.

(3) Plagioclase

In contrast to olivine, plagioclase laths dominate the groundmass. Crystals are generally subhedral to euhedral (0.1-0.5 mm) and shows trachytic texture in several samples. Plagioclase laths commonly show twinning (in large enough crystals for observation) and often contain inclusions of vapour.

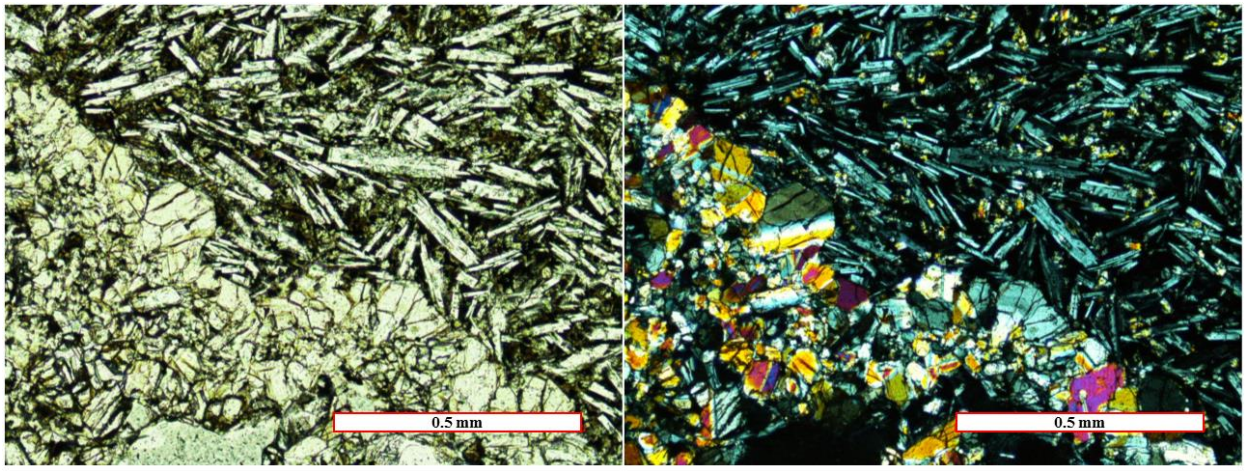

Figure 8. Plagioclase laths in groundmass showing trachytic texture. (Left) Plane-Polarized Light. (Right) Cross-Polarized Light; pyroxenes are visible in clusters and in the groundmass.

(4) Other identified components

Xenoliths, volcanic glass, and oxide minerals (e.g., ilmenite, magnetite) are also observable in Manguao Basalt samples. Chert xenoliths are easily noticeable in hand specimens. Observed chert xenoliths are surrounded by thin pyroxene reaction rims. Volcanic glass is visible in the groundmass between plagioclase laths and pyroxene grains, forming intersertal textures. Opaque oxide minerals are also present in the groundmass, between pyroxene grains, plagioclase laths, and volcanic glass.

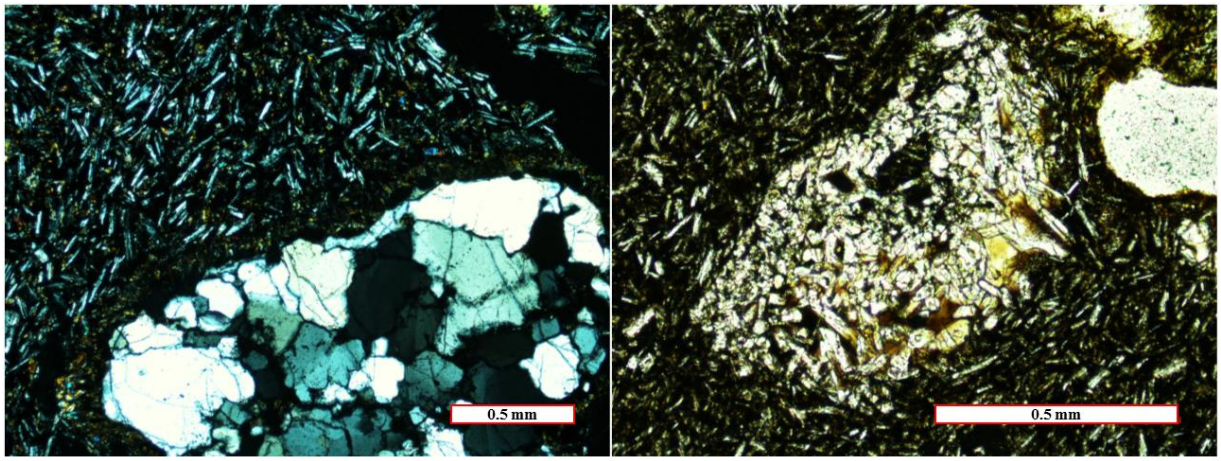

Figure 9. (Left) Chert xenolith in Manguao Basalt. Xenoliths are surrounded by thin pyroxene reaction rims. (Right) Volcanic glass (brown regions) in between pyroxene clusters.

Crystallization sequence from observed mineral relationships

Olivine and pyroxene phenocrysts represent earliest-formed phases in Manguao Basalt. Despite olivine prevalence in the phenocryst assemblage, observations of olivine-pyroxene relationship in petrographic thin sections show the earlier crystallization of the pyroxenes. Olivine is the last crystallizing phase in the phenocryst assemblage. The presence of skeletal textures in olivine reflects the shift in crystallization rate prior to the formation of the groundmass. Euhedral to subhedral plagioclase laths dominate the groundmass over any other identified component (i.e., anhedral pyroxene or volcanic glass). The re-emergence of pyroxenes in the succession is reflected by its reappearance in the groundmass. Lastly, solidification of the remaining melt trapped between plagioclase laths and pyroxene grains formed the interstitial volcanic glass.

Crystallization sequence observed in Manguao Basalt does not seem to show characteristic succession common to near-surface basaltic melts (i.e., Poldervaart and Hess, 1951), where olivine typically precedes pyroxene formation. Hence, a more detailed study on mineral chemistry can greatly supplement in this discussion (in chapter 4).

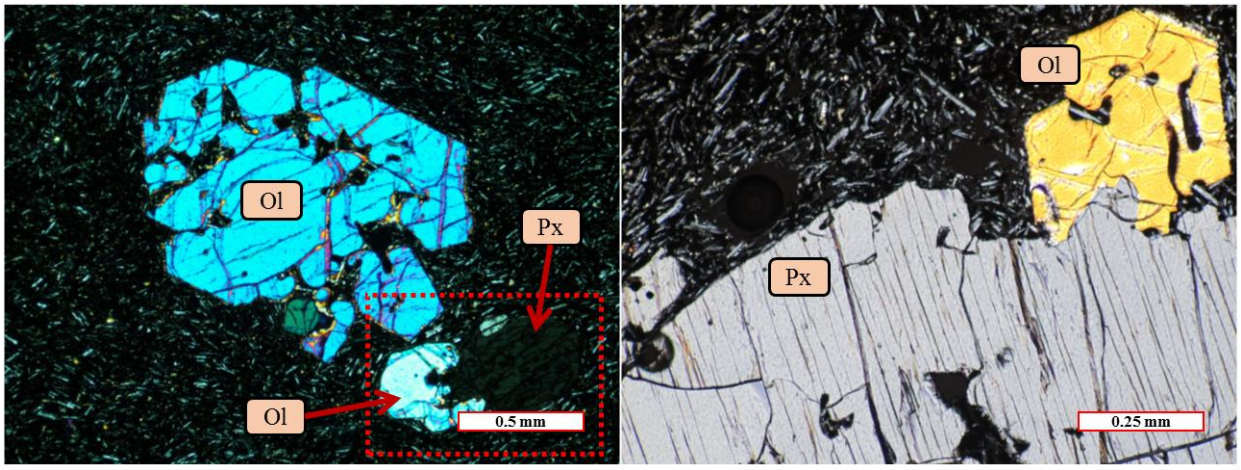

Figure 10. (Left) Skeletal olivine beside an olivine-pyroxene phenocryst (red dotted box). (Right) Similar olivine-pyroxene phenocryst. Olivine is clearly seen here attached to the larger pyroxene crystal, possibly implying a later formation.

Major Element Geochemistry

Analyzed whole-rock major element compositions of Manguao Basalt shows a narrow range of values (SiO_2 = 48-53%; TiO_2 = 2%; Al_2O_3 = 14-15%; FeO^t = 9-11%; CaO = 7-8%; MgO = 8-10%). Comparing with average compositions of common tholeiitic and calc-alkali basalts of Wilkinson (1986; Table 1) shows similarities with olivine tholeiites. Normative compositions (CIPW; based from methods of Johannsen, 1931) show generally quartz-normative compositions (silica-oversaturated; Fig. 6), with plagioclase and hypersthene comprising more than 50% of the norm. Magnesium-number (Mg#) calculated from bulk-rock compositions (Mg# = Mg/Mg+Fe+Mn) shows evolved character (Mg# = 59-64).

Manguao Basalt is characterized as a subalkaline, basalt-basaltic andesite based on Total Alkali vs. Silica (TAS; Fig. 7) classification of Le Maître et al. (2002). AFM diagram plots of Manguao Basalt samples show inclination towards iron enrichment during early fractionation (Fig. 8), characteristic of tholeiitic melts. Total iron and magnesium ratio (FeO^t/MgO) versus silica (SiO_2; Miyashiro, 1974) of Manguao Basalt samples (Fig. 9), on the other hand, plot within the calc-alkaline field. The presence of chert xenoliths, however, is a likely cause for this shift.

Table 1. Manguao Basalt major element composition range and other common basalts from Wilkinson (1986)

Manguao Basalt	No. of Analyses	SiO_2 (wt%)	TiO_2 (wt%)	Al_2O_3 (wt%)	FeO^t (wt%)	MnO (wt%)	MgO (wt%)	CaO (wt%)	Na_2O (wt%)	K_2O (wt%)	P_2O_5 (wt%)	Total
Highest Value	16	52.95	2.13	15.00	10.62	0.17	9.52	8.27	2.74	1.03	0.41	98.97
Lowest Value	16	48.37	1.94	13.69	9.05	0.14	8.03	7.72	2.46	0.55	0.28	97.61
Average		51.71	2.04	14.22	9.64	0.15	8.62	8.01	2.62	0.86	0.34	98.21
Wilkinson (1986)	No. of Analyses	SiO_2 (wt%)	TiO_2 (wt%)	Al_2O_3 (wt%)	FeO^t (wt%)	MnO (wt%)	MgO (wt%)	CaO (wt%)	Na_2O (wt%)	K_2O (wt%)	P_2O_5 (wt%)	Total
MORB-type, low K, low-Al Olivine-Tholeiite	530	50.08	1.55	15.07	9.89	0.10	8.12	11.51	2.53	0.14	0.13	98.21
MORB-type, low K, high-Al Olivine-Tholeiite	309	49.88	1.17	16.95	8.65	0.08	7.95	11.89	2.42	0.13	0.10	98.43
Olivine Tholeiite	458	49.22	2.16	14.10	11.05	0.17	8.75	10.34	2.39	0.56	0.25	97.97
Calc-Alkaline, Low-K/Na, Olivine-Basalt	395	50.15	1.35	17.89	9.23	0.14	6.57	10.05	2.82	0.76	0.21	98.32
Calc-Alkaline, Medium-K/Na, Olivine-Basalt	53	50.58	1.27	18.57	8.81	0.34	5.73	9.07	2.73	1.78	0.35	98.42

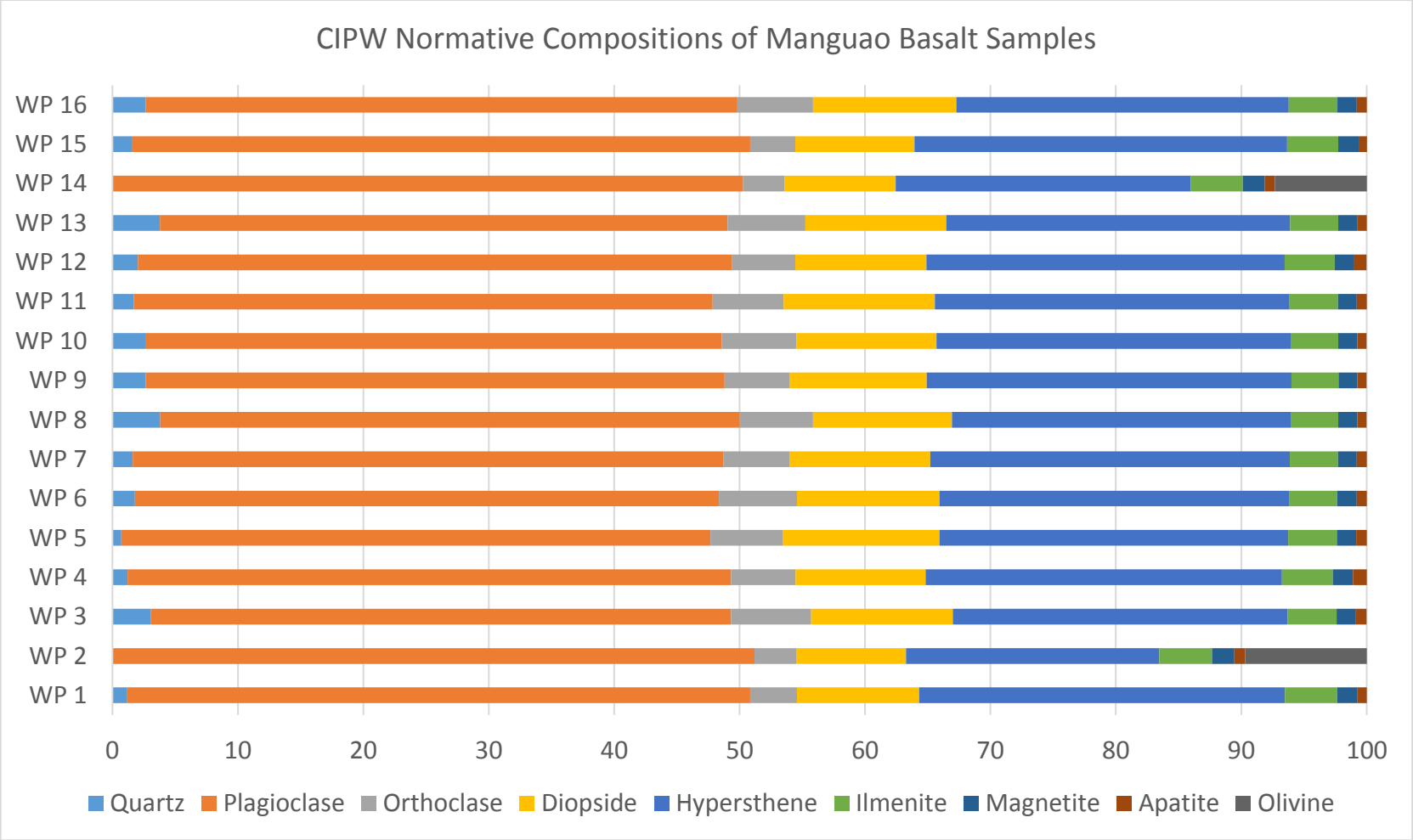

Figure 11. CIPW normative compositions calculated from Manguao Basalt compositions (Fe^{3+}/Total Iron = 0.1).

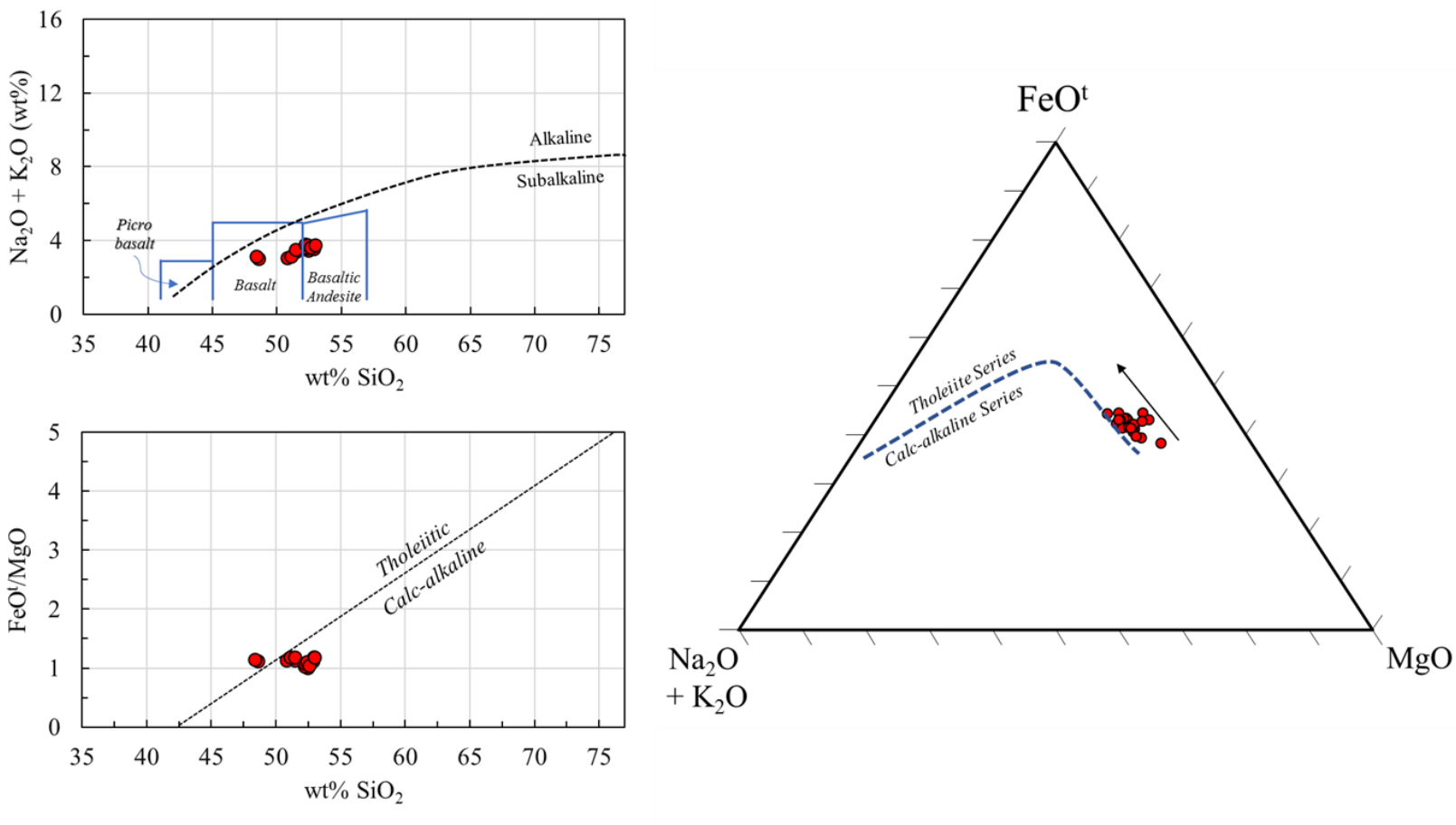

Figure 12. (a) Total Alkali vs. Silica (TAS; Peccerillo and Taylor, 1976), (b) FeOt/MgO vs SiO_2 (Miyashiro, 1974), and (c) AFM ternary plots (Kuno, 1968) of Manguao Basalt samples. Total iron expressed as FeO^t. TAS diagram shows plotting of Manguao Basalt samples within the basalt to basaltic-andesite fields (subalkaline). Manguao Basalt plots in the Miyashiro (1974) diagram shows the 'straddling' between tholeiitic and calc-alkaline affinities. The presence of chert xenoliths, however, may have affected SiO_2 bulk concentrations. AFM ternary diagram shows inclination towards Fe-enrichment; diagnostic feature of tholeiitic melts. Arrow approximates Fe-enrichment during evolution.

Selected major element bivariate diagrams (SiO_2, FeO^t, TiO_2, Al_2O_3, CaO, $Na_2O + K_2O$) reflect the early fractionation of ferromagnesian minerals (Figs. 10 and 11). Calcium and aluminum ratios (CaO/Al_2O_3), on the other hand, are relatively constant, reflecting the limited removal of feldspars. Mineral-compatible trace elements (Ni and Co) also reflect the early fractionation of olivines.

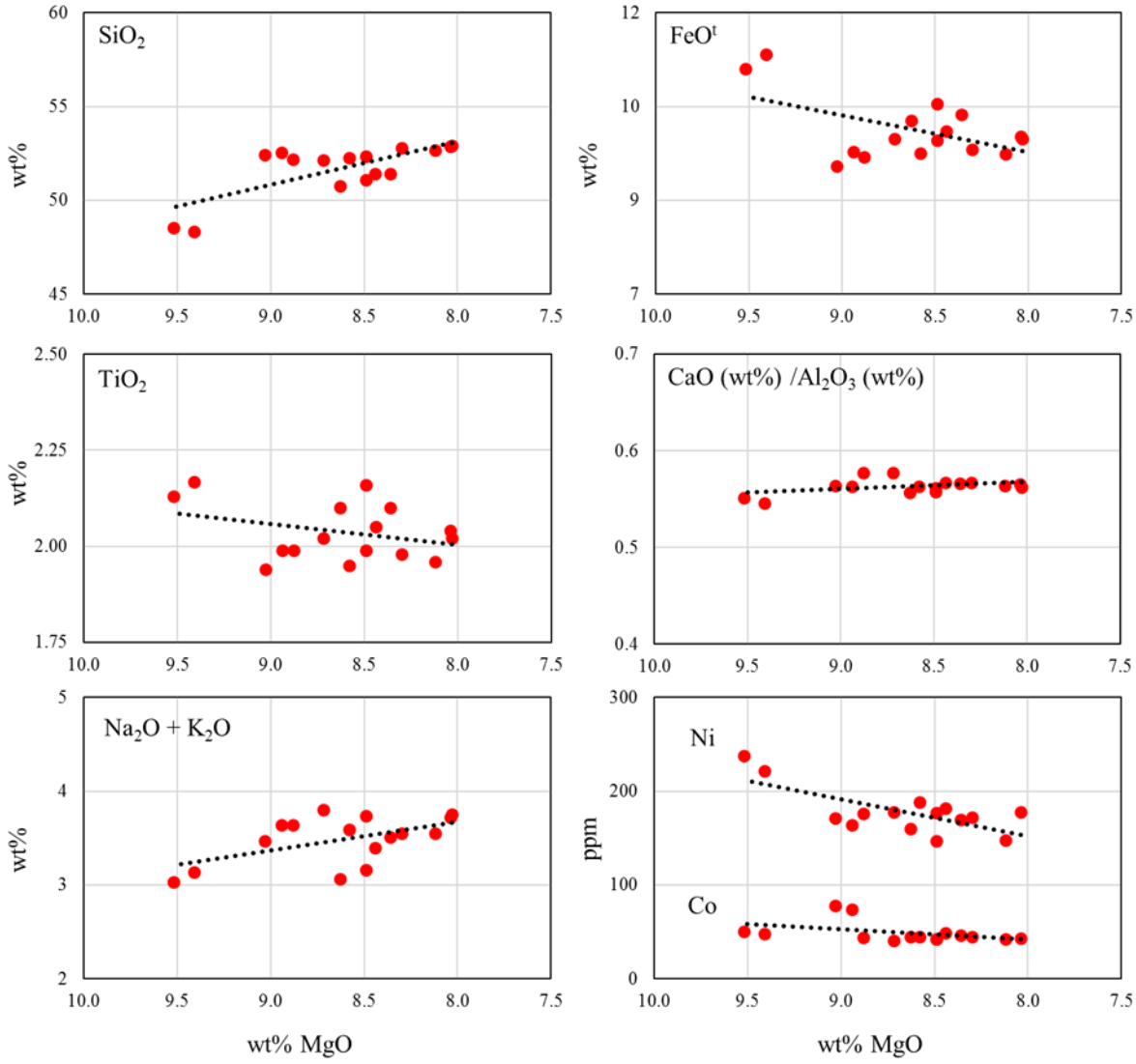

Figure 13. Selected major (SiO_2, FeO^t, TiO_2, CaO/Al_2O_3, $Na_2O + K_2O$; in wt% oxide) and trace elements (Ni and Co; in ppm) plotted on bivariate diagrams. Abscissa of all plots are in MgO (wt%). Silica (SiO_2) and alkalis ($Na_2O + K_2O$) show strong increasing trend with decreasing MgO. Total iron (FeO^t), titanium (TiO_2) and olivine-compatible trace elements (Ni and Co) show decreasing trend with decreasing MgO; possibly indicating fractionation of the ferromagnesians. CaO/Al_2O_3 ratios appear to be unaffected by decreasing MgO; possibly indicating limited plagioclase fractionation.

Trace Element Geochemistry

The selective partitioning of trace elements, with respect to mineral constituents, is essential for constraining physical-chemical melt conditions for the characterization of magma source (Pearce and Norry, 1979; Halliday et al., 1995; Salters and Longhi, 1999; Bebout, 2007; Li et al., 2015; Spandler, 2017). Tectonic discrimination using trace elements is a common method employed for providing initial information on the environment that produces basalts and other volcanic rocks (Pearce and Cann, 1973). There are numerous tectonic discrimination diagrams that are widely published and utilized (e.g., Pearce and Norry, 1979; Shervais, 1982; Pearce, 2008), but careful consideration must be applied in order not to overgeneralize with limited trace element data (Li et al., 2015).

Manguao Basalt samples plot within the 'within-plate basalts' field defined by (1) Pearce and Norry (1979), outside any field (Island-Arc basalts and Continental Flood Basalts) defined by (2) Shervais (1982), and slightly above the MORB-OIB array defined by (3) Pearce (2008). These deviations observed reiterates the danger and inconsistencies of using only trace element tectonic discrimination diagrams (Li et al., 2015). However, these observed deviations from the defined fields are reflective of some processes operating within known tectonic systems (i.e., elevated Th from continental crust contamination show vertical shift from MORB-OIB array in Th/Yb vs. Nb/Yb diagram of Pearce, 2008) and hence, may provide some utility as supplementary information.

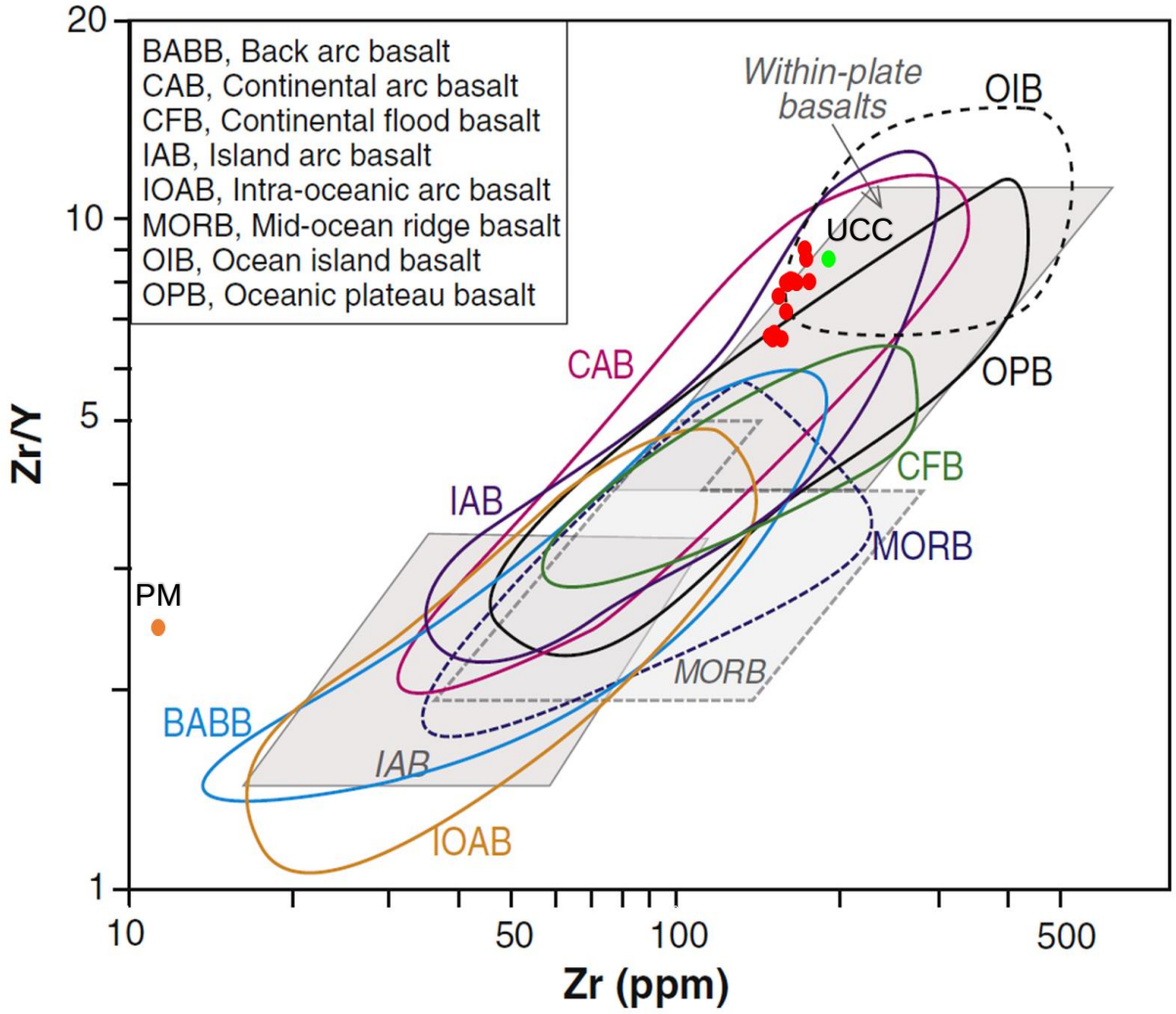

Figure 14. Zr/Y vs. Zr plots of Manguao Basalt samples (red). Gray shaded regions (Within-plate basalts, MORB, and IAB) are defined by Pearce and Norry (1979). Base diagram and all other defined regions (e.g., colored ellipsoid and dashed regions) are from Li et al. (2015). Manguao Basalt samples plot within Pearce and Norry (1979) definition of 'within-plate basalts'. At the same time, the samples also plot within continental- and island-arc basalts of Li et al. (2015). Primitive mantle (PM; orange dot) and upper continental crust (UCC; green dot) are also plotted. PM, Primitive Mantle of Sun and McDonough (1989); UCC, Upper Continental Crust of Taylor and McLennan (1995)

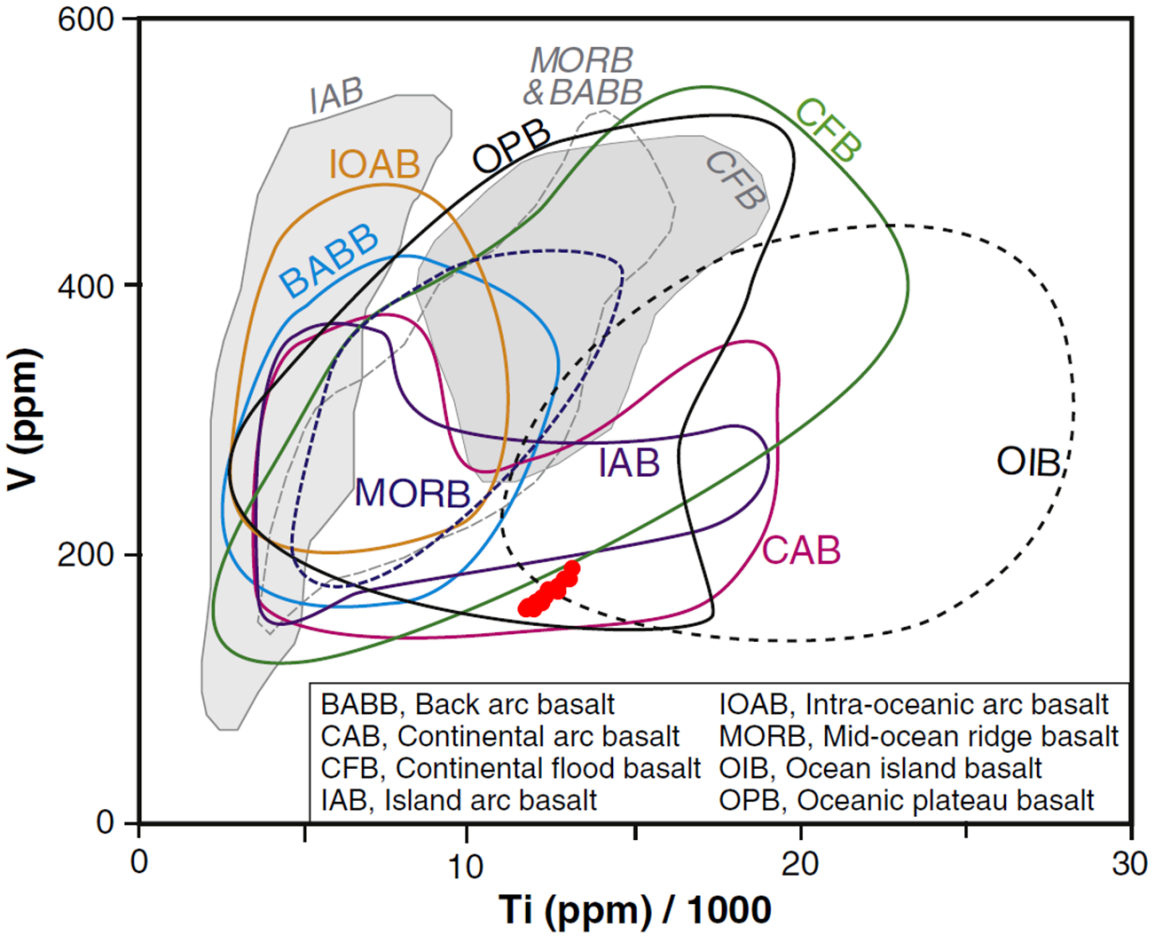

Figure 15. V vs. Ti plots of Manguao Basalt samples (red). Gray shaded regions (Island-arc and Continental Flood Basalts) are defined by Shervais (1982). Base diagram and all other defined regions (e.g., colored ellipsoid and dashed regions) are from Li et al. (2015). Manguao Basalt samples plot outside any field defined by Shervais (1982). Li et al. (2015) modified the diagram; Manguao Basalt now plots within continental-arc basalts and continental flood basalts. Vanadium data for PM, UCC, and Depleted Mantle are unavailable for plotting.

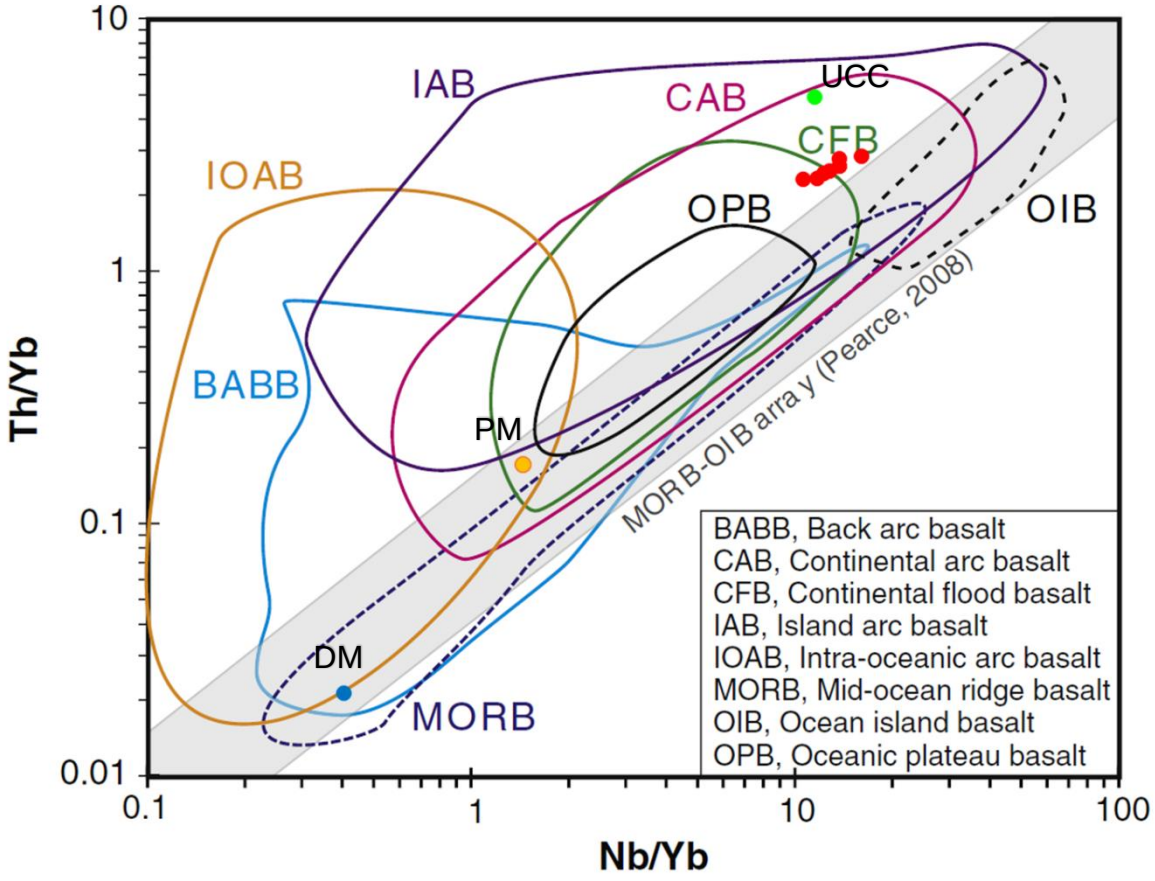

Figure 16. Th/Yb vs. Nb/Yb plots of Manguao Basalt samples (red). Gray shaded region is the MORB-OIB array defined by Pearce (2008). Base diagram and all other defined regions (e.g., colored ellipsoid and dashed regions) are from Li et al. (2015). Manguao Basalt samples plot outside the array. The diagram also classifies Manguao Basalt as having trace element signatures similar with continental-arc, island-arc, and continental flood basalts; defined by Li et al. (2015). Depleted mantle (DM, blue dot), primitive mantle (PM; orange dot) and upper continental crust (UCC; green dot) are also plotted. DM, Depleted Mantle of Workman and Hart (2005); PM, Primitive Mantle of Sun and McDonough (1989); UCC, Upper Continental Crust of Taylor and McLennan (1995).

Other than bivariate diagrams, trace element spider diagrams show multi-element ratios compared to a known and established standard (e.g., MORB). Standard trace element concentrations may vary slightly from author to author (i.e., Thompson, 1982; Sun, 1980; Sun and McDonough, 1989), but will always be arranged according to some known chemical trend (i.e., trace element compatibility). Hence, trace element spider diagrams are often used to enrich discussions on melt production, evolution, and crystallization.

Primitive mantle (PM) normalized spider diagram of Manguao Basalt samples show a negative sloping pattern, where the most incompatible trace elements (i.e., Cs and Rb) show higher ratios compared with the most compatible trace elements (i.e., Yb and Lu). Positive trace element anomalies in Th and Pb are clearly seen in this spider diagram. This negative sloping pattern reflects the enriched character of Manguao Basalt.

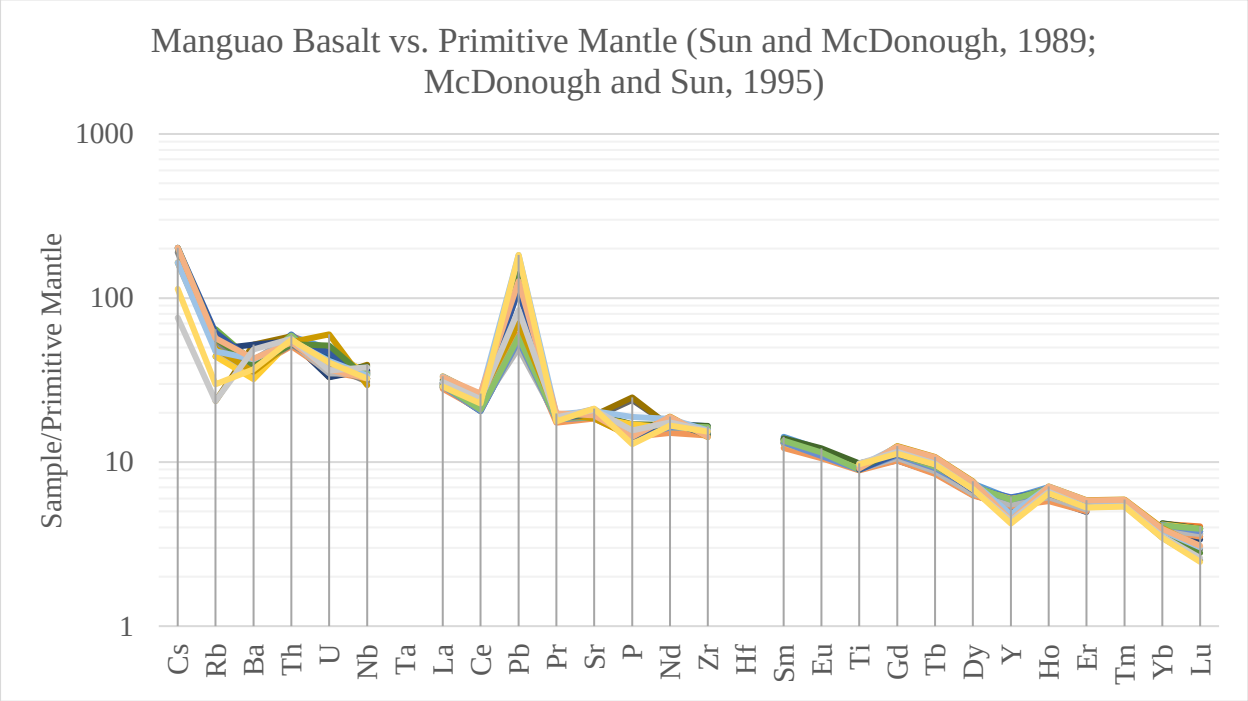

Figure 17. Primitive mantle-normalized trace element spider diagram of Manguao Basalt samples. A negative sloping pattern can be observed, indicating enriched character. Positive trace element anomalies in Th and Pb are clearly seen. Primitive mantle trace element data from Sun and McDonough (1989) and McDonough and Sun (1995). Ta and Hf data are unavailable.

Manguao Basalt samples also show the enriched character in MORB- (Pearce, 1983), NMORB- (Sun and McDonough, 1989), and EMORB-normalized (Sun and McDonough, 1989) trace element spider diagrams. Subduction influence is unlikely for Manguao Basalt based on the absence of the diagnostic Nb-Ta depletion (negative anomaly). Most incompatible elements, on the other hand, show highest concentrations in Manguao Basalt. High-field strength elements (HFSE; yttrium and ytterbium), on the other hand, are slightly lower for Manguao Basalt.

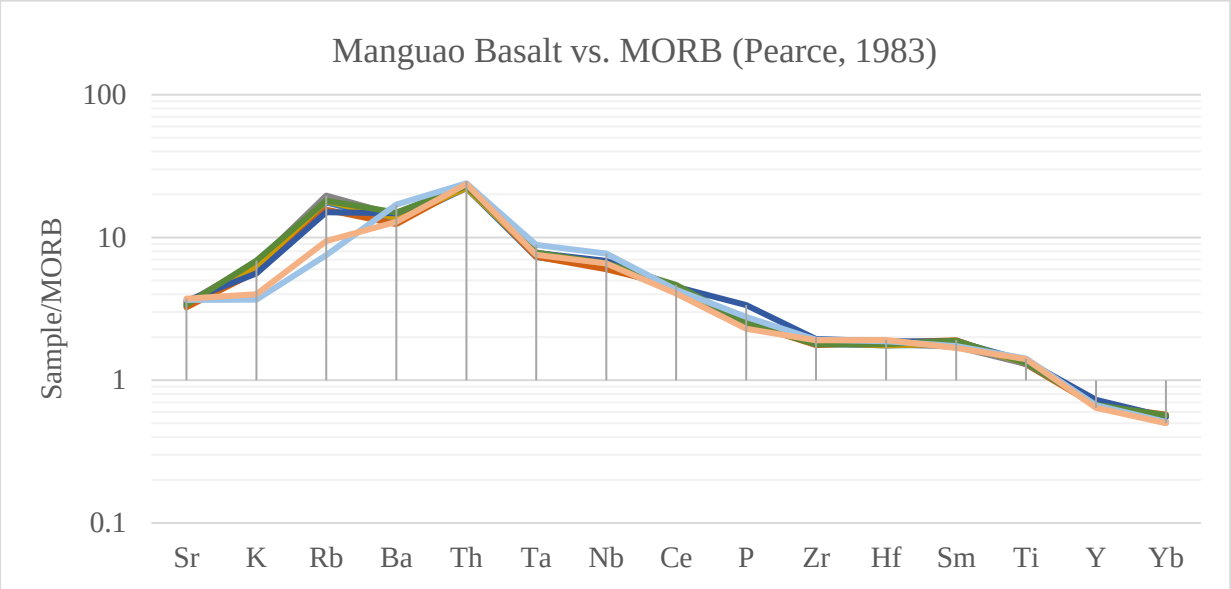

Figure 18. MORB-normalized trace element spider diagram of Manguao Basalt samples. A diagnostic 'humpback' pattern can be observed, which reflects the 'enriched' character of the basalt. Highest ratios are observed for thorium. High-field strength elements are depleted for Manguao Basalt.

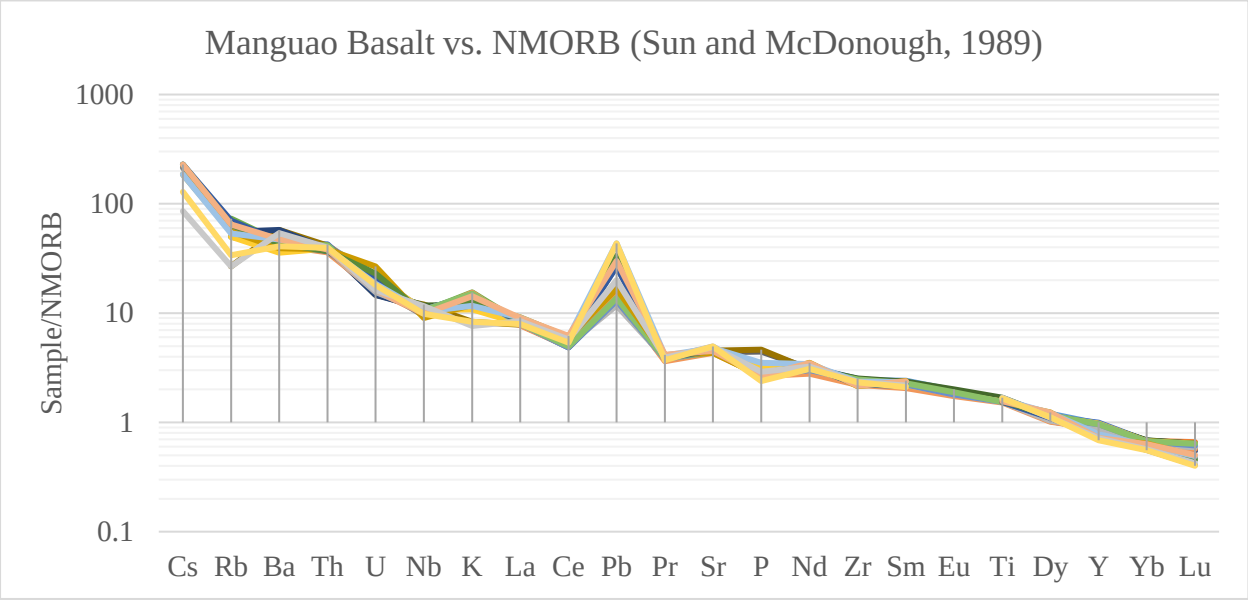

Figure 19. NMORB-normalized trace element spider diagram of Manguao Basalt samples. General sloping pattern can be observed, reflecting enriched character. Highest ratios are observed for most incompatible trace elements. High-field strength elements are lower for Manguao Basalt. Lead concentration of Manguao Basalt shows positive anomaly (minor in K and Th). Supplementary data for Eu is included (C. Arcilla, unpublished).

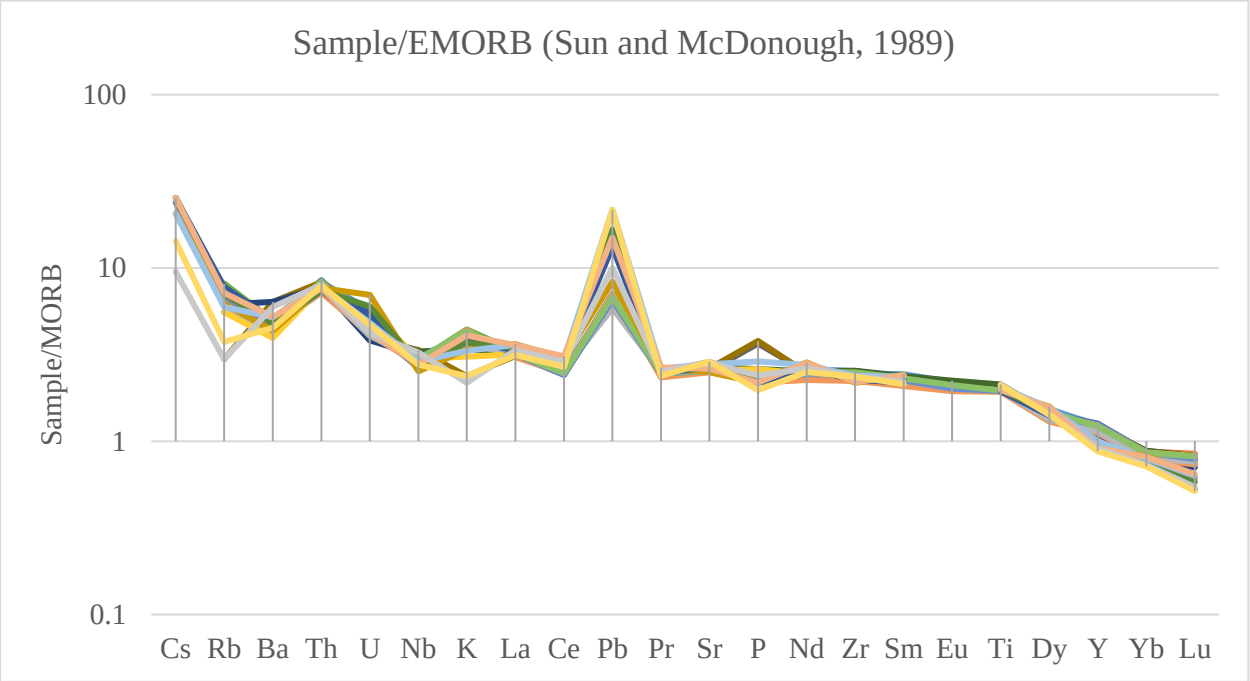

Figure 20. EMORB-normalized trace element spider diagram of Manguao Basalt samples. Trace element ratios show less sloping pattern, but still indicating enriched character. Thorium, potassium, and lead anomalies are still observed. Supplementary data for Eu is included (C. Arcilla, unpublished).

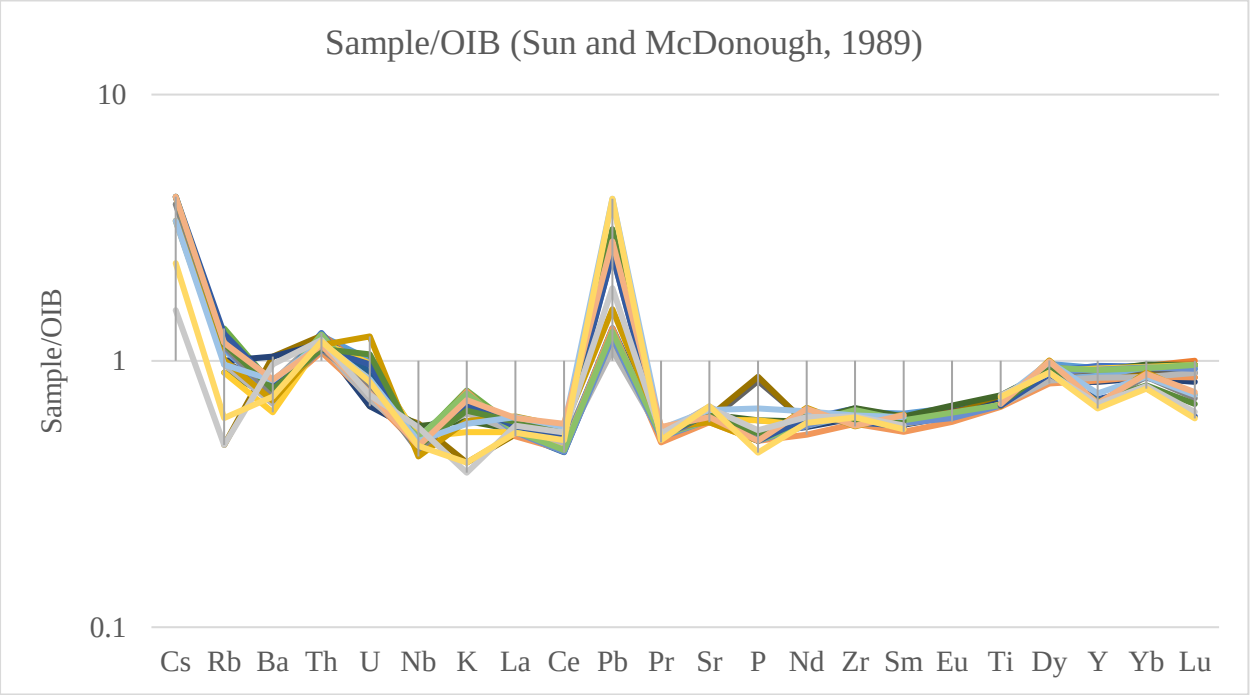

Figure 21. OIB-normalized trace element spider diagram of Manguao Basalt samples. Most trace element ratios plot below 1, reflecting lower concentrations in Manguao Basalt compared to OIBs. Positive anomalies in Th, K, and Pb are also observable.

Trace element spider diagram of Manguao Basalt compared to OIB (Sun and McDonough, 1989), on the other hand, shows a relatively flat pattern. Rare earth elements (REE) to high-field strength elements (HFSE) reflect the flat pattern, while the large-ion lithophile elements still show enrichment. Most trace element ratios plot below 1, indicating concentrations lower than average OIB compositions. Positive trace element anomalies in Th, K, and Pb are observable.

Trace element geochemistry provides excellent supplementary information to understanding petrogenetic conditions affected by tectonic influences:

(1) Bivariate diagrams of nickel and cobalt (vs. MgO) show fractionation of olivines, and possibly other ferromagnesian minerals (e.g., pyroxenes).

(2) Tectonic discrimination diagrams using trace elements (Zr/Y vs. Zr of Pearce and Norry,1979; V vs. Ti of Shervais, 1982; Th/Yb vs Nb/Yb of Pearce, 2008) show enriched character of Manguao Basalt and similarities with 'within-plate basalts' (in Pearce and Norry, 1979). Other tectonic discrimination diagrams do not work well for Manguao Basalt (i.e., Shervais, 1982 and Pearce, 2008). Even with modifications of Li et al. (2015), Manguao Basalt can still be associated with different tectonic settings (i.e., with continental-arc basalts, island-arc basalts, and continental flood basalts). Furthermore, discriminating between MORB and OIB influences still prove to be inaccurate in some diagrams (i.e., plotting outside the MORB-OIB array).

(3) Trace element spider diagrams further testify to the enriched character of Manguao Basalt. Primitive mantle-, NMORB- and EMORB-normalized spider diagrams show negative sloping patterns that reflect typical enriched character. Positive anomalies in some continent-derived trace elements (e.g., Th and Pb) are consistent in any spider diagram presented. Comparing Manguao Basalt to OIB, on the other hand, shows a relatively flat pattern for REE, but still showing negative slopes in LILE. Positive anomalies in Th and Pb possibly reflect enrichment

Akita University

that is unrelated to source (i.e., crustal contamination). The presence of chert xenoliths further testifies to the idea of incorporating continent-derived material to the Manguao Basalt melt.

(4) The absence of characteristic Nb-Ta depletion (Kelemen et al., 1993) in spider diagrams attests to the idea of a non-subduction influence for generating melt of Manguao Basalt. This evidence, alongside absence of recent or active subduction in the area, put constraints on the possible tectonic influences responsible for inducing magmatism in Northern Palawan.

References

Bebout, G. (2007) Trace Element and Isotopic Fluxes/ Subducted Slab. In Treatise on Geochemistry (R. Rudnick, Eds.). pp. 1–50, Elsevier, USA.

Halliday, A., Lee, D., Tommasini, S., Davies, G., Paslick, C., Fitton, J. and James, D. (1995) Incompatible trace elements in OIB and MORB and source enrichment in the sub-oceanic mantle. Earth and Planetary Science Letters, 133, 379–395.

Johannsen, A. (1931) A Descriptive Petrography of the Igneous Rocks, Vol. 1. Introduction, Textures, Classification, and Glossary. The Journal og Geology, 40, 182–185.

Kelemen, P.B., Shimizu, N. and Dunn, T. (1993) Relative depletion of niobium in some arc magmas and the continental crust: partitioning of K, Nb, La and Ce during melt/rock reaction in the upper mantle. Earth and Planetary Science Letters, 120, 111–134.

Kuno, H. (1968) Differentiation of Basalt Magmas. In Basalts: The Poldervaart treatise on rocks of basaltic composition (Hess, H.H. and Poldervaart, A., Eds.). pp. 862, Interscience Publishers, New York and London, 623–688.

Le Maitre, R.W., Streckeisen, A., Zanettin, B., Le Bas, M.J., Bonin, B. and Bateman, P. (2002) Igneous Rocks: A Classification and Glossary of Terms (Recommendations of the IUGS Subcommission on the Systematics of Igneous Rocks). pp. 263, Cambridge University Press.

Li, C., Arndt, N., Tang, Q. and Ripley, E. (2015) Trace element indiscrimination diagrams. Lithos, 232, 76–83.

McDonough, W.F. and Sun, S.S. (1995) The composition of the Earth. Chemical Geology, 67 (5), 1050–1056.

Miyashiro, A. (1974) Volcanic rock series in island arcs and active continental margins. American Journal of Science, 274, 321–355.

Pearce, J.A. and Cann, J.R. (1973) Tectonic setting of basic volcanic rocks determined using trace element analyses. Earth and Planetary Science Letters, 19 (2), 290–300.

Pearce, J.A. and Norry, M. (1979) Petrogenetic Implications of Ti, Zr, Y, and Nb Variations in Volcanic Rocks. Contributions to Mineralogy and Petrology, 69, 33–47.

Pearce, J.A. (2008) Geochemical fingerprinting of oceanic basalts with applications to ophiolite classification and the search for Archean oceanic crust. Lithos, 100 (1-4), 14–48.

Peccerillo, A. and Taylor, S.R. (1976) Geochemistry of Eocene Calc-Alkaline Volcanic Rocks from the Kastamonu area, Northern Turkey. Contributions to Mineralogy and Petrology, 58, 63–81.

Poldervaart, A. and Hess, H.H. (1951) Pyroxenes in the Crystallization of Basaltic Magma. The Journal of Geology, 59 (5), 472–489.

Salters, V. and Longhi, J. (1999) Trace element partitioning during the initial stages of melting beneath mid-ocean ridges. Earth and Planetary Science Letters, 166, 15–30.

Shervais, J.W. (1982) Ti-V plots and the petrogenesis of modern and ophiolitic lavas. Earth and Planetary Science Letters, 59 (1), 101-118.

Spandler, C., Hammerli, J. and Yaxley, G. (2017) An experimental study of trace element distribution during partial melting of mantle heterogeneities. Chemical Geology, 462, 74–87.

Sun, S.S. (1980) Lead isotopic study of young volcanic rocks from mid-ocean ridges, ocean islands and island arcs. Philosophical Transactions of the Royal Society A: Mathematical, Physical and Engineering Sciences, 297 (1431), 409-445.

Sun, S.S. and McDonough, W.F. (1989) Chemical and isotopic systematics of oceanic basalts: Implications for mantle composition and processes. Geological Society Special Publications, 42, 313-345.

Taylor, S.R. and McLennan, S.M. (1995) The geochemical evolution of the continental crust. Reviews of Geophysics, 33(2), 241–265.

Thompson, R.N. (1982) Magmatism of the British Tertiary Volcanic Province. Scottish Journal of Geology, 18, 49–107.

Wilkinson, J.F.G. (1986) Classification and Average Chemical Compositions of Common Basalts and Andesites. Journal of Petrology, 27, 31–62.

Chapter 4: Insights on Crystallization of Tholeiite Melts

Introduction

This chapter investigates in detail the whole-rock major element and mineral chemistry of Manguao Basalt to give insights to the (1) character of possible mantle source, and (2) source melting/crystallization conditions leading to its formation. The results and discussions included in this chapter were submitted for publication to the Journal of Mineralogical and Petrological Sciences (JMPS).

Scientific Background

The Philippines is an archipelagic country located on the western side of the Pacific. The formation of the Philippine islands is generally interpreted as the amalgamation of arc-derived units, ophiolitic suites, and transported continental blocks (e.g., Mindoro and Palawan islands). Tectonic activity in the country is the result of the interaction between three major plates: Eurasian, Pacific, and Indo-Australian (Karig, 1983; Aurelio, 2000). Geologically, the Philippines is divided into two distinct units (Fig. 1): (1) the Philippine Mobile Belt (PMB) and (2) the Palawan Continental Block (PCB)/North Palawan Block (NPB). Active volcanism and major strike-slip faulting occur more frequently in PMB, which contrasts to the relatively more stable PCB (Taylor and Hayes, 1980; Holloway, 1982; Aurelio, 2000; Aurelio et al., 2013).

The Philippine Mobile Belt owes its active nature to the surrounding subduction zones (East Luzon Trough and Philippine Trench in the east. Manila Trench, Negros-Sulu Trench, and Cotabato Trench in the west). Young (Plio-Quaternary) magmatic arcs generally reflect the activity in these nearby subduction zones and defines the different volcanic belts that are found in the country (Luzon Central-Cordillera Arc, Northern Sierra Madre-Catanduanes Arc, Negros Arc, East Philippine Arc, Cotabato Arc, and Sulu-Zamboanga Arc; Aurelio, 2000).

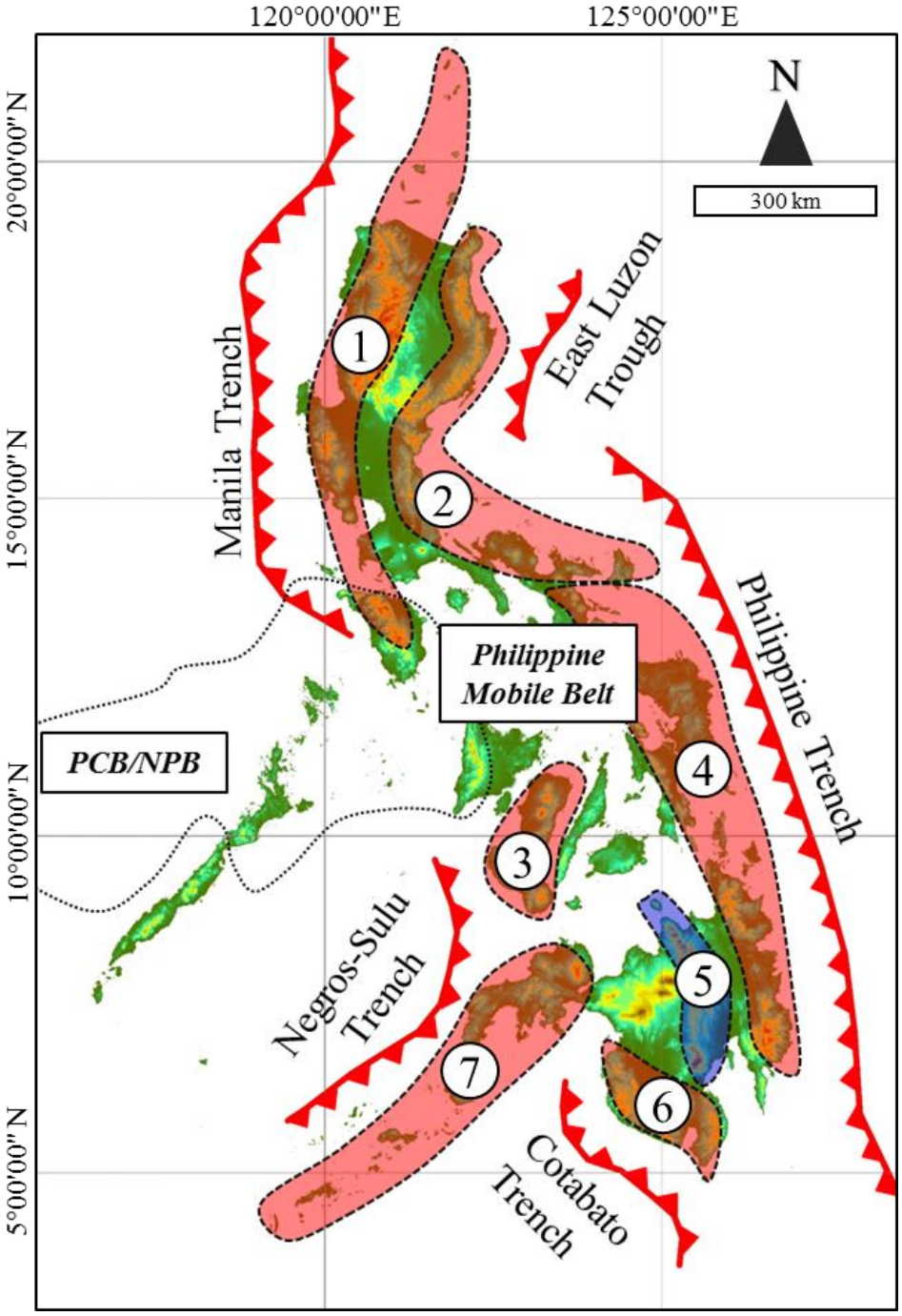

Figure 22. Simplified tectonic map of the Philippines showing the distribution of volcanic arcs (red shaded regions in dashed outline) and adjacent active trenches. Tectonic features modified from Magro et al. (2013) and Aurelio (2000). ① Luzon Central Cordillera Arc is controlled by activity of the Manila Trench in the west. ② Northern and Southern Sierra Madre-Catanduanes activity is related to the Philippine Trench in the east and former activity of the East Luzon Trough. ③ Negros Arc is related to the Negros-Sulu Trench. ④ East Philippine Arc is related to the Philippine Trench. ⑤ Magmatic activity in the Central Mindanao Arc (shaded blue) are related to a completely subducted oceanic slab with influence from partial activity of the Philippine Trench. ⑥ Cotabato Arc is related to the Cotabato Trench. ⑦ Sulu-Zamboanga Arc is related to Negros-Sulu Trench. Boundaries of Palawan Continental Block derived from Liu et al. (2014). Base Philippine image generated from Shuttle Radar Topography Mission (SRTM; 90-m resolution) data from philgis.org.

Akita University

The Palawan region (Fig. 2), on the other hand, contrasts the character of the PMB (i.e., active volcanism is absent in the entire island). No active subduction zone surrounds Palawan Island and igneous units in the region are very few (i.e., Palawan Ophiolite and Kapoas Granite). Manguao Basalt represents the youngest igneous unit in the Northern Palawan stratigraphic group. Formerly known as Manguao Volcanics, Manguao Basalt is a Plio-Pleistocene formation consisting of porphyritic vesicular basalts, shales, siltstones, conglomerates and associated pyroclastic rocks (Peña, 2008). Exposures of the lava flow are distributed in low-lying areas, particularly along the east bank of Lake Manguao and southeast end of Taytay reaching Calauag Bay (Fig. 3). Equivalent lava flow units dated Plio-Pleistocene (Fontaine, 1979) are also reported in nearby islands of Cuyo Group, east of Palawan (Peña, 2008). Report of mineral deposits including Manguao Basalt by the Japan International Cooperation Agency (MMAJ-JICA, 1990) assigns a Pleistocene age for the lava flow.

Brief geologic history of Palawan Island and associated magmatism

The northern half of Palawan Island rests on the extended oceanic portion of the Eurasian plate, which separated from the mainland during the opening of the South China Sea (Taylor and Hayes, 1980; Hall, 2002; Yumul et al., 2009; Aurelio et al., 2013; Guan et al., 2016). The transport of this separated block resulted in the emplacement of the Palawan Ophiolite in the southern end of the island (Encarnación and Mukasa, 1997; Militante-Matias et al., 2000; Yumul et al., 2009; Aurelio et al., 2013), while regional metamorphism was developing in the northern end (Williams, 1997; Almasco et al., 2000; Aurelio, 2000; Yumul et al., 2009). Rifting of the South China Sea and following southward migration of Palawan eventually lead to its collision with the PMB in the Early Miocene (Taylor and Hayes, 1980; Karig, 1983; Almasco et al., 2000; Yumul et al., 2009; Aurelio et al., 2013; Liu et al., 2014). Plio-Quaternary volcanism, including Manguao Basalt, commenced after the collision (Taylor and Hayes, 1980; Karig, 1983; Almasco et al., 2000; Aurelio et al., 2013; Liu et al., 2014).

The limited occurrence of magmatic events in the northern Palawan region is reflected in the stratigraphic record (Williams, 1997; Almasco et al., 2000; Aurelio, 2000; Militante-Matias et al., 2000; Yumul et al., 2009; Aurelio et al., 2013; Guan et al., 2016). Continent-derived sedimentary and

metamorphic rocks are the oldest (Permian) and the dominant lithologies found in the northern Palawan region (Holloway, 1982; Hall, 1997). Magmatic intrusions, like the Capoas Granite (Middle Miocene), represent the post-rifting melt formation during the Cenozoic (Encarnación and Mukasa, 1997; Williams, 1997; Almasco et al., 2000; Aurelio, 2000; Yumul et al., 2009). Manguao Basalt, on the other hand, is the youngest and latest volcanic activity in the Palawan region.

At present, no active trench is found surrounding Palawan Island. P-wave tomography study of Fan et al. (2017) shows the absence of a subducting slab underneath. Instead, a low velocity region appears to underlie the continental crust. Geophysical investigation of Liu et al. (2014) describes PCB as a "hyper-extended continental crust intruded with magmatic bodies". The structural map of Pubellier et al. (2018) seems to agree with this idea, showing numerous NW-trending extensional faults that coincide with the locations of the different magmatic intrusions/units found in the north Palawan region. The origin of other igneous units in the area (e.g., Capoas Granite) attests to the presence of magmatism in a "post-rifting, non-collisional tectonic setting" (Encarnación and Mukasa, 1997).

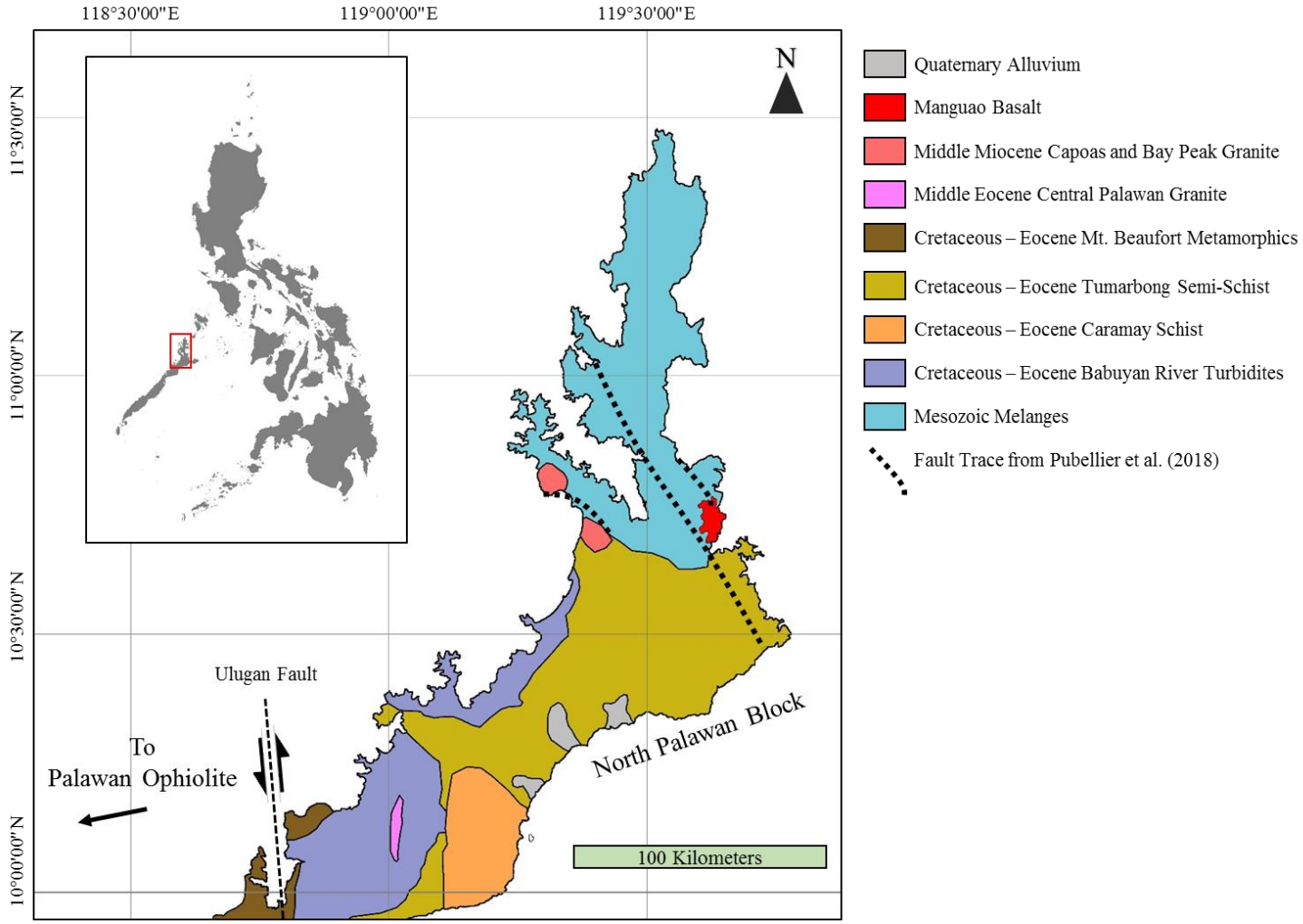

Figure 23. Simplified geologic map of North Palawan Island showing distribution of lithologies with continental affinity. Red, light red, and pink indicate igneous units. Manguao Basalt is assigned with a Plio-Pleistocene age. Other magmatic units include the Middle Miocene Capoas and Bay Peak Granite, and the Middle Eocene Central Palawan Granite. Cretaceous-Eocene units included in the map are members of the Palawan Ophiolite. The Ulugan Fault is a structural boundary separating the Palawan Continental Block from the Palawan Ophiolite. Map reconstructed from Suggate et al. (2014) and Almasco et al. (2000). Base image generated from SRTM DEM (90-m resolution; from philgis.org).

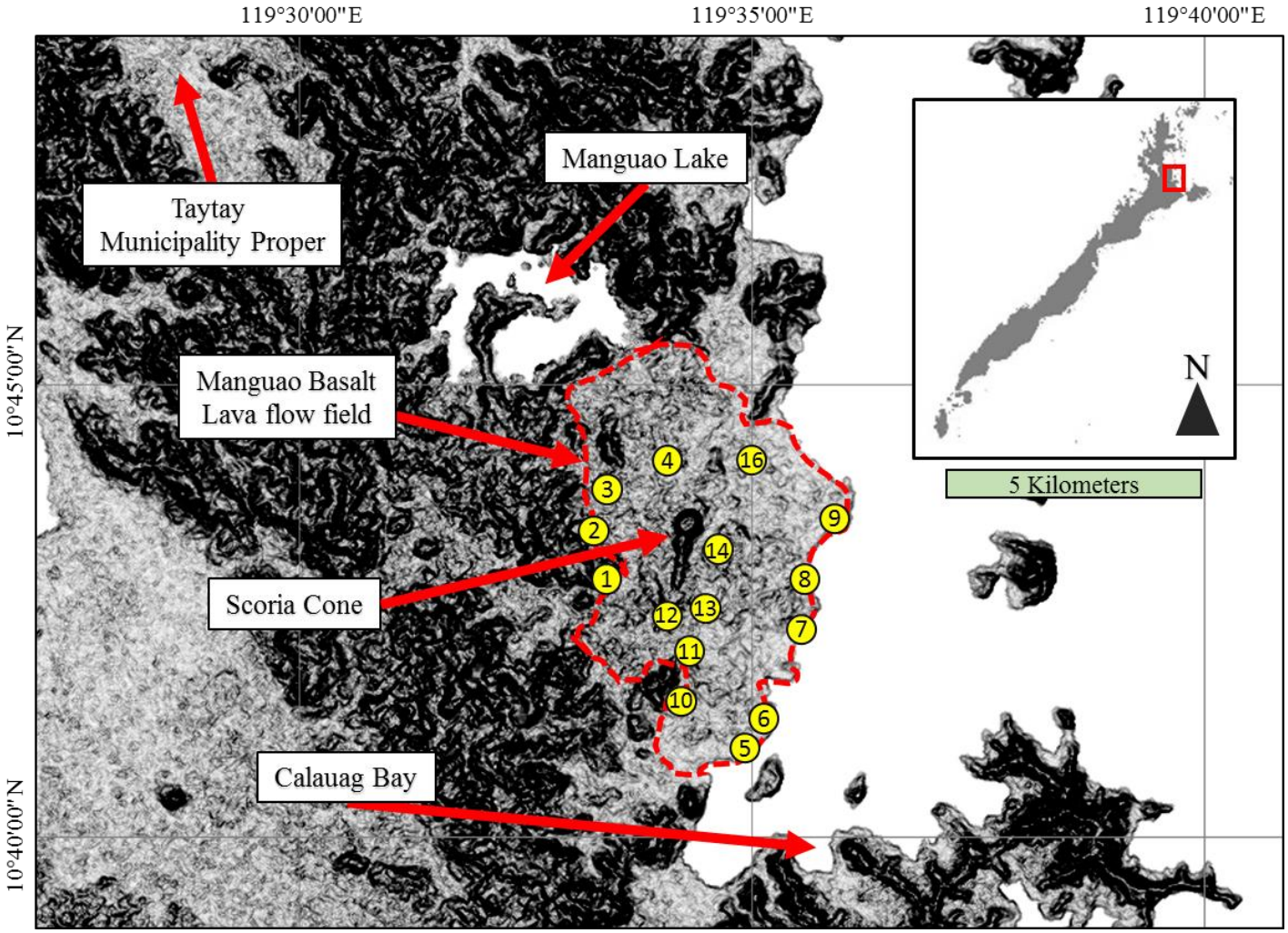

Figure 24. Palawan Island (Inset) and Manguao Basalt lava field (dashed region). Yellow circles denote sampling locations (WP 1–16; Point 14 are two samples taken at proximity, WP 14–15). Tadpole-shaped feature in the middle of the lava field is a scoria cone. Manguao Lake is found northwest of the lava field exposure. Map generated using Landsat 7 ETM+ (15-m spatial resolution; 3-spectral bands) and SRTM DEM (90-m resolution) from philgis.org.

Methodology

Manguao Basalt lava flow samples were obtained from nearshore and inland surface exposures in Taytay, North Palawan, Philippines. Thin sections of the basaltic rocks were prepared at the National Institute of Geological Sciences-University of the Philippines Diliman (NIGS-UPD), Philippine Department of Energy (DOE), and Akita University, Japan. Whole-rock geochemical analyses were done using X-ray fluorescence spectroscopy (XRF), Inductively-coupled plasma mass spectrometer (ICP-MS), and Inductively-coupled plasma optical emission spectrometer (ICP-OES) at Intertek Testing Services Philippines. Wavelength-dispersive instrument, Panalytical AxiosMax PW: 4400/40 was used for XRF, while Agilent Technologies 7700x and Agilent Technologies 5100 Radial were used for ICP-MS and ICP-OES, respectively. The resulting major and trace element compositions are provided in Table 1.

Mineral chemistry analyses were done using a scanning electron microscope with energy dispersive spectroscopy (SEM-EDS) and electron probe microanalysis (EPMA) at Akita University. We used a JEOL JSM-IT300 with Oxford EDS detector X-MaxN for SEM-EDS and JEOL JXA-8230 for EPMA. Operating conditions of SEM-EDS for all semi-quantitative point analyses were done at high vacuum conditions, 10 mm working distance, 15 kV accelerating voltage, and probe current of 2.20 nA. A 50-second acquisition time for point analyses was done on carbon coated samples (~ 30 nm thickness at 2.25 g/cm^3 carbon coat density). EPMA operating conditions for all point analyses were done at 15 kV accelerating voltage, 5 μm probe diameter, and at 20 nA probe current. Quantitative mineral analyses of samples were obtained from EPMA using the JEOL silicate standards set (for SiO_2, CaO, FeO^t, Al_2O_3, MgO, TiO_2, MnO, Na_2O, K_2O, Cr_2O_3, and NiO). EPMA results with weight percent oxide (wt%) totals within 99 to 101 wt% were included for stoichiometric, geothermometry, and geobarometry calculations. A list of all pertinent equations used is provided as supplementary material (Appendix-Table 1).

Akita University

Table 2. Major and trace element chemistry of Manguao Basalt samples

Equipment/Procedure	XRF	XRF	XRF	XRF	XRF	XRF	XRF	XRF	XRF	XRF	XRF	ICP	ICP	ICP	ICP
Element	SiO_2	TiO_2	Al_2O_3	FeO^t	MnO	MgO	CaO	Na_2O	K_2O	P_2O_5	Total	Ni	Co	Zn	Cr
Units	wt%	wt%	wt%	wt%	wt%	wt%	wt%	wt%	wt%	wt%	wt%	ppm	ppm	ppm	ppm
Detection Limit	0.01	0.01	0.01	0.01	0.01	0.01	0.01	0.01	0.01	0.01	0.01	1	0.1	1	5
WP 1	51.11	2.16	14.97	10.05	0.15	8.49	8.35	2.54	0.62	0.31	98.75	147	42	123	335
WP 2	48.37	2.17	15.27	10.85	0.17	9.41	8.34	2.58	0.56	0.38	98.09	222	48	117	333
WP 3	52.90	2.04	14.05	9.53	0.15	8.04	7.94	2.65	1.07	0.36	98.73	178	43	115	340
WP 4	51.45	2.10	14.47	9.88	0.15	8.36	8.19	2.65	0.86	0.46	98.58	170	46	124	327
WP 5	52.19	2.02	13.94	9.50	0.15	8.72	8.06	2.83	0.97	0.36	98.74	178	41	110	336
WP 6	52.37	1.99	13.99	9.47	0.15	8.49	7.86	2.71	1.03	0.35	98.40	177	42	110	306
WP 7	52.58	1.99	14.03	9.29	0.14	8.94	7.90	2.75	0.89	0.34	98.85	164	74	110	309
WP 8	52.73	1.96	13.85	9.25	0.14	8.12	7.81	2.58	0.97	0.31	97.72	148	42	112	282
WP 9	52.45	1.94	13.69	9.05	0.14	9.03	7.72	2.61	0.86	0.31	97.8	171	78	114	279
WP 10	52.31	1.95	13.72	9.27	0.15	8.58	7.73	2.60	0.99	0.31	97.61	188	45	113	276
WP 11	52.23	1.99	13.69	9.21	0.15	8.88	7.91	2.70	0.94	0.33	98.03	176	44	115	275
WP 12	51.45	2.05	14.15	9.62	0.15	8.44	8.04	2.56	0.84	0.41	97.71	182	49	129	300
WP 13	52.84	1.98	13.71	9.32	0.15	8.30	7.79	2.52	1.03	0.31	97.95	172	45	119	275
WP 14	48.59	2.13	15.00	10.62	0.17	9.52	8.27	2.48	0.55	0.34	97.67	238	50	121	296
WP 15	50.79	2.10	14.70	9.78	0.15	8.63	8.18	2.46	0.60	0.28	97.67	160	45	125	305
WP 16	52.95	2.02	14.23	9.50	0.15	8.03	8.00	2.74	1.01	0.34	98.97	146	40	111	312

XRF, X-ray Fluorescence Spectrometer; ICP, Inductively-coupled Plasma Mass Spectrometer and Inductively-coupled Plasma Optical Emission Spectrometer. All samples were analyzed by Intertek Testing Services Philippines Laboratory (PNS ISO/IEC 17025:2005 LA-2010-167B)

Akita University

MELTS Parameters

Simulations of melting and crystallization processes were done using the MELTS program of Gualda et al. (2012) and Ghiorso and Gualda (2015). Melting was primarily induced by depressurization of the upper mantle. This is following the idea of a thinned continental lithosphere (Liu et al., 2014), the presence of melting within the upper mantle (low-velocity region; Fan et al., 2017), and the extensional features observed in the region (Pubellier et al., 2018). Fertile (KLB-1 Peridotite of Davis et al., 2009) and depleted (Depleted Mantle of Workman and Hart, 2005) mantle sources were used as starting compositions for the upper mantle. Melting experiments of dry peridotites by Hirose and Kushiro (1993) provided the initial pressure and temperature conditions of a fertile upper mantle source (KLB-1) at equilibrium; 15 kbar and 1350 °C, respectively. Initial input of the mantle compositions and parameters in the MELTS program produced a solid mantle. In addition, the modal compositions of mantle produced in the simulations resembled the respective calculated modes of KLB-1 and depleted mantle (Table 2).

From the initially solid upper mantle, simulations of depressurization melting were done at isothermal conditions (1350 °C) and QFM buffer. The pressure was lowered every 0.1 kbar until the system reached the highest obtained pressures from geobarometry (pressure conditions during the crystallization of the first crystals, orthopyroxenes; ~ 5 kbar). Two melting scenarios were done on both fertile and depleted mantle sources: (1) retaining equilibrium between source and melt, and (2) liquid fractionation. The resulting primitive melt compositions are recorded and summarized in Table 3.

On the other hand, all crystallization simulations were done at isobaric conditions (~ 5 kbar) and QFM buffer. Pressure was kept constant to simplify the conditions during the formation of the first crystals. The temperature was lowered every 10 °C until the liquid completely solidified. Two crystallization scenarios were done: (1) retaining the equilibrium between melt and crystals, and (2) crystal fractionation. The resulting simulated pyroxene compositions (orthopyroxenes and clinopyroxenes) were compared with the compositions of pyroxenes in Manguao Basalt. The evolving melt compositions were also recorded and summarized in Table 3. Supplementary data for melt evolution

and compositions of other mineral components (olivine and plagioclase) are provided in the Appendix (Tables 2–6).

Table 3. Composition of fertile and depleted mantle sources

KLB-1 Spinel Lherzolite (Davis et al., 2009)					Depleted Mantle Source (Workman and Hart, 2005)				
Oxide Composition (wt%)		Modal Composition (%) from Davis et al. (2009)		Modal Composition (%) obtained from MELTS	Oxide Composition (wt%)		Modal Composition (%) from Workman and Hart (2005)		Modal Composition (%) obtained from MELTS
SiO_2	44.84	Ol	60	58.26	SiO_2	44.71	Ol	57	53.70
TiO_2	0.11	Opx	23	22.60	TiO_2	0.13	Opx	28	27.18
Al_2O_3	3.51	Cpx	14	15.49	Al_2O_3	3.98	Cpx	13	15.13
FeO^t	8.20	Sp	2	2.56	FeO^t	8.18	Sp	2	3.95
MnO	0.12				MnO	0.13			
MgO	39.52				MgO	38.73			
CaO	3.07				CaO	3.17			
Na_2O	0.30				Na_2O	0.13			
K_2O	0.02				K_2O	0.01			
Cr_2O_3	0.32				Cr_2O_3	0.57			

Table 4. Primitive and evolved melt compositions

		Isothermal Decompression Melting (15–5 kbar; 1350 °C)				Equilibrium Crystallization (T_i = 1350 °C; 1260–1230 °C)			
	Manguao Basalt (Ave)	KLB-1 Eq. Melt	KLB-1 Frac. Melt	DMM Eq. Melt	DMM Frac. Melt	KLB-1 Eq. Melt	KLB-1 Frac. Melt	DMM Eq. Melt	DMM Frac. Melt
SiO_2 (wt%)	51.71	49.62	46.87	48.42	46.07	48.15–48.51	47.05–47.94	43.70–45.80	43.25–44.85
TiO_2 (wt%)	2.04	0.51	0.63	0.61	0.76	1.03–1.73	0.84–1.11	1.88–3.31	1.68–3.22
FeO^t (wt%)	9.64	8.01	8.39	8.13	8.56	7.95–9.51	7.84–9.37	9.49–10.54	10.00–12.54
MgO (wt%)	8.62	13.85	13.1	14.37	14.11	7.00–8.73	6.68–8.99	8.60–9.65	8.48–10.13
CaO (wt%)	8.01	12.7	13.22	13.44	14.71	8.74–10.83	8.20–10.90	11.33–12.35	10.69–12.09
Melt Produced (total %)	-	19.96	18.36	19.40	17.14	-	-	-	-
Melt Remaining (%)	-	-	-	-	-	11–38	29–61	6–22	5–30

Table 4. (Continued)

Fractional Crystallization (T_i = 1350 °C; 1260–1230 °C)			
KLB-1 Eq. Melt	KLB-1 Frac. Melt	DMM Eq. Melt	DMM Frac. Melt
44.46–46.97	46.25–45.93	40.86–44.19	41.50–44.11
0.92–1.66	0.82–1.22	1.51–2.82	1.48–2.76
10.17–14.96	9.29–12.12	12.43–18.70	11.92–17.67
7.77–9.01	7.11–9.12	8.70–9.96	8.61–10.19
9.04–11.00	8.51–11.18	10.55–12.13	10.31–11.99
-	-	-	-
25–49	40–68	17–35	21–43

Results

Exposures of the lava flow are preserved in several areas near the coast (Fig. 4). The lava flow generally appears blocky and constrained within channels. Lava flow features and structures, such as levees and tumuli, are still intact and identifiable. Sixteen (16) samples were obtained from different sites in the lava flow field (WP 1-16). All basalt samples are porphyritic, vesicular, and contain numerous xenoliths.

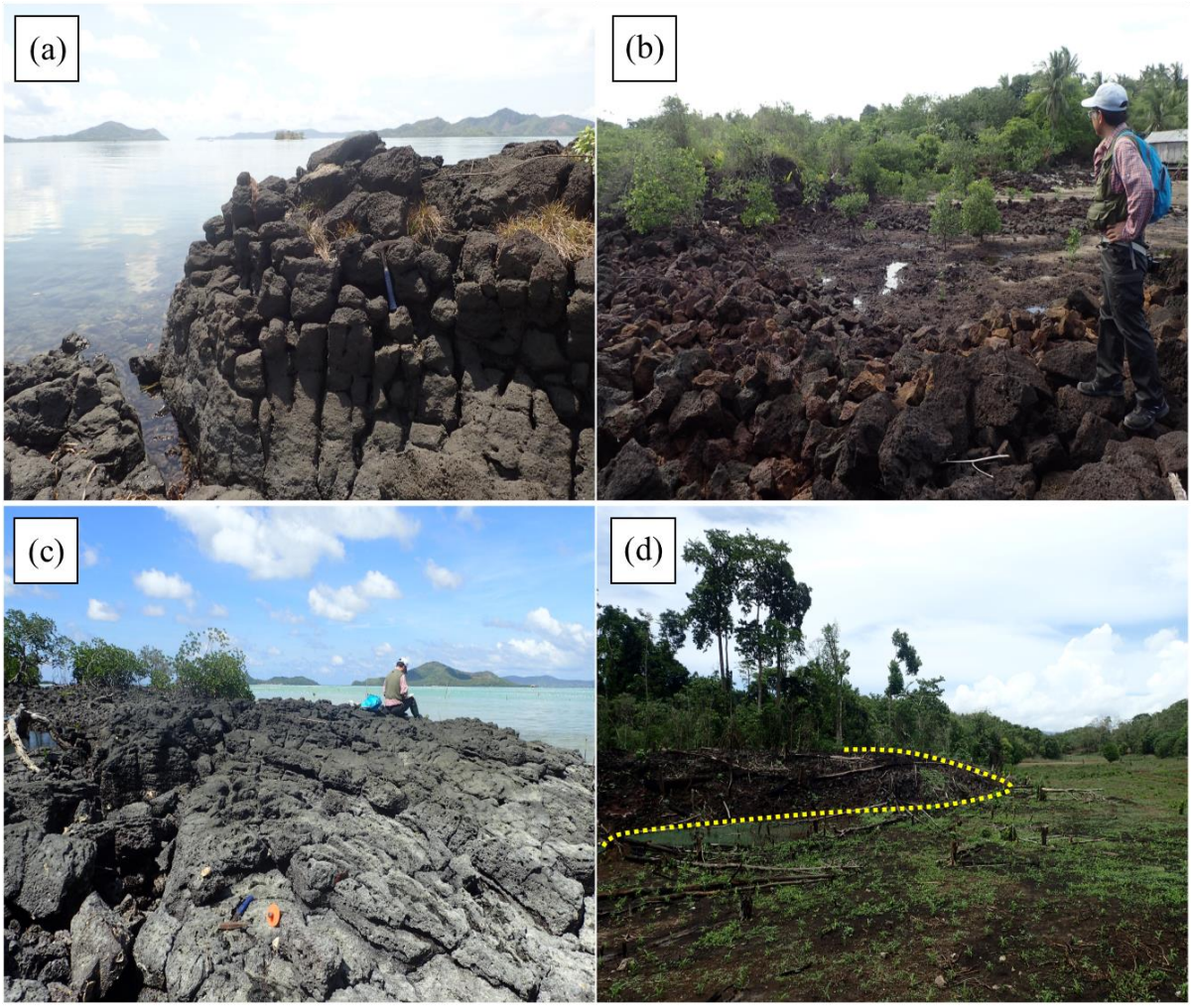

Figure 25. Manguao Basalt lava field surface exposures. (a) Near-shore exposures show good preservation of lava flow structures; side of lava channel leading towards the sea. (b) Preserved lava tumulus. (c) Pahoehoe lava flow structures. (d) Preserved lava front.

Petrography and Mineral Chemistry

Manguao Basalt samples are porphyritic and vesicular. Phenocryst size ranges from 0.5 to 2 mm. The phenocryst assemblage is composed of mostly olivine (> 90%; Fig. 5a) and minor pyroxenes (Fig. 5b and 5c). Chert xenoliths and mineral clusters (Fig. 5d) are also present in most samples. The fine-grained fraction is composed of the microcrystalline groundmass (Fig. 5d) and volcanic glass. The groundmass assemblage is composed mainly of plagioclase, pyroxenes, and opaque minerals (e.g., Ilmenite). Plagioclase laths are the largest units in the groundmass (0.3–0.5 mm). Smaller (0.1–0.3 mm) anhedral pyroxenes are found between the plagioclase laths. Blebby volcanic glass fills the interstitial spaces between the plagioclases and groundmass pyroxenes. Classification of the identified mineral components (olivine, pyroxenes, and plagioclase) are summarized in Fig. 6.

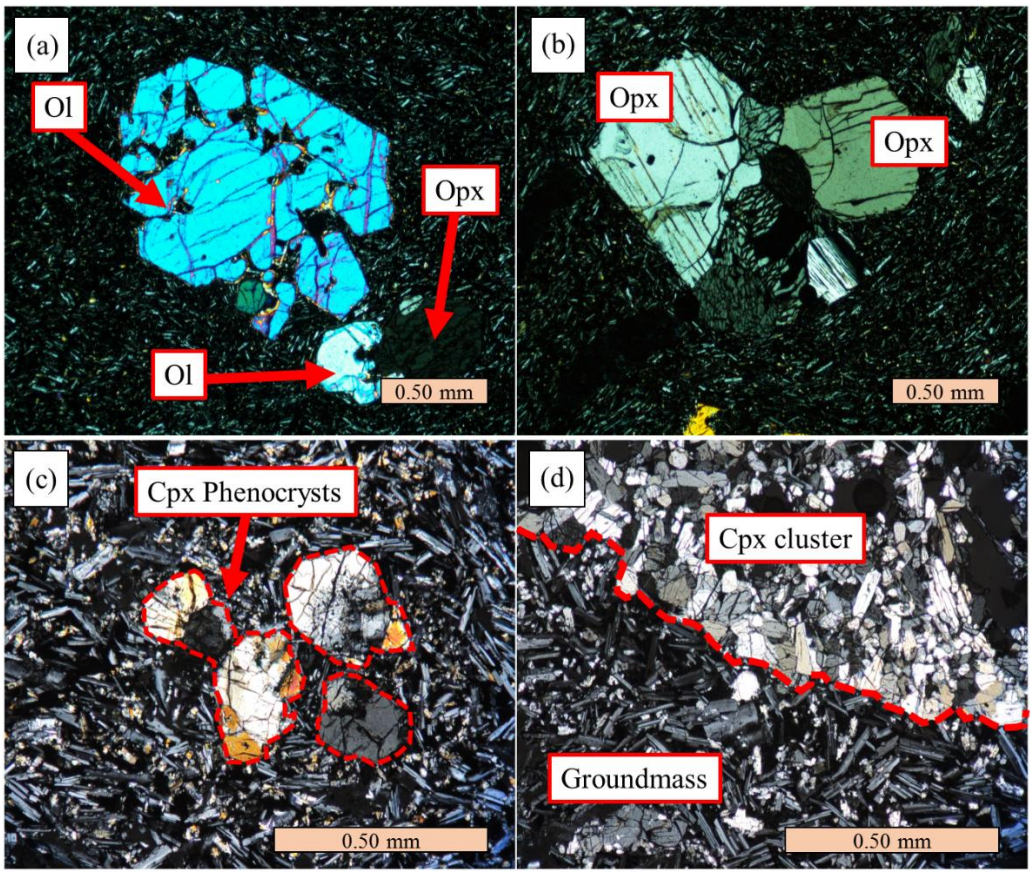

Figure 26. Coarse-grained units in Manguao Basalt. (a) Ol phenocryst with skeletal and embayed textures. Smaller phenocrysts below show an Ol grain (illuminated) partially 'engulfing' Opx (near extinction). (b) Large Opx crystal surrounded by a Pl-dominated groundmass. (c) Cpx phenocrysts. (d) Cluster of Cpx crystals.

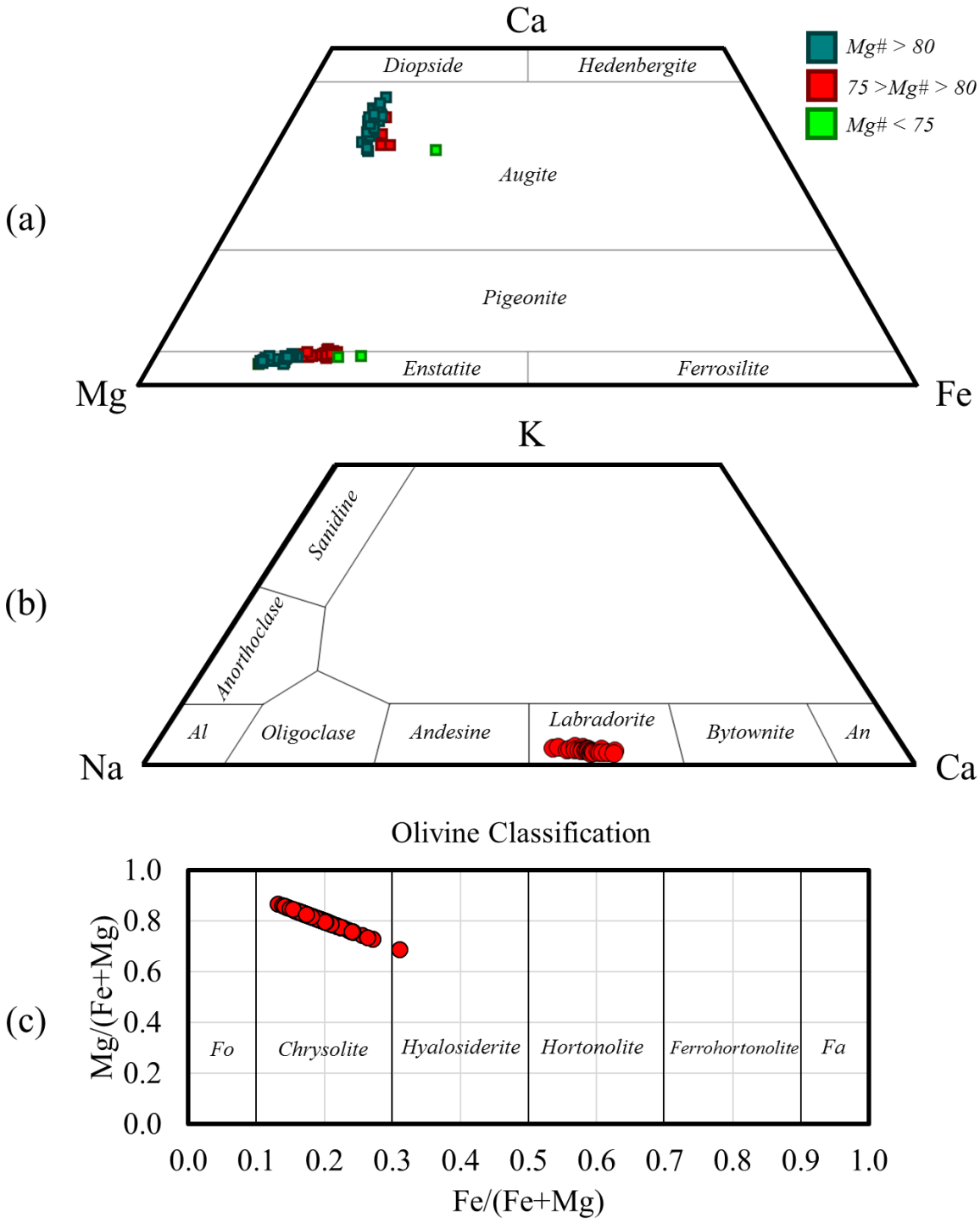

Figure 27. Classification diagrams of different mineral phases present in Manguao Basalt. (a) Pyroxenes ternary diagram. Pyroxene phenocrysts generally have high Mg# (>80). Groundmass pyroxenes have lower Mg# (65–80). Pyroxene clusters vary in Mg# (65–83). Pyroxene fields from Morimoto (1988). (b) Feldspars ternary classification diagram. Feldspar fields derived and modified from Deer et al. (2013). Al, Albite; An, Anorthite (c) Olivine species are plotted within the chrysolite field. Olivine fields derived and modified from Deer et al. (2013). Fo, Forsterite; Fa, Fayalite

Olivine

Olivine (Ol) occurrence appears to be generally restricted in the phenocrysts (0.5–1.0 mm). Observed Ol phenocrysts are typically euhedral to subhedral (Fig. 5a). Most crystals show skeletal texture and resorbed edges. Few observed Ol crystals are attached to the edge of a larger pyroxene phenocryst. This is petrographic evidence of a pyroxene forming much earlier than Ol in the crystallization sequence (Fig. 7a-c).

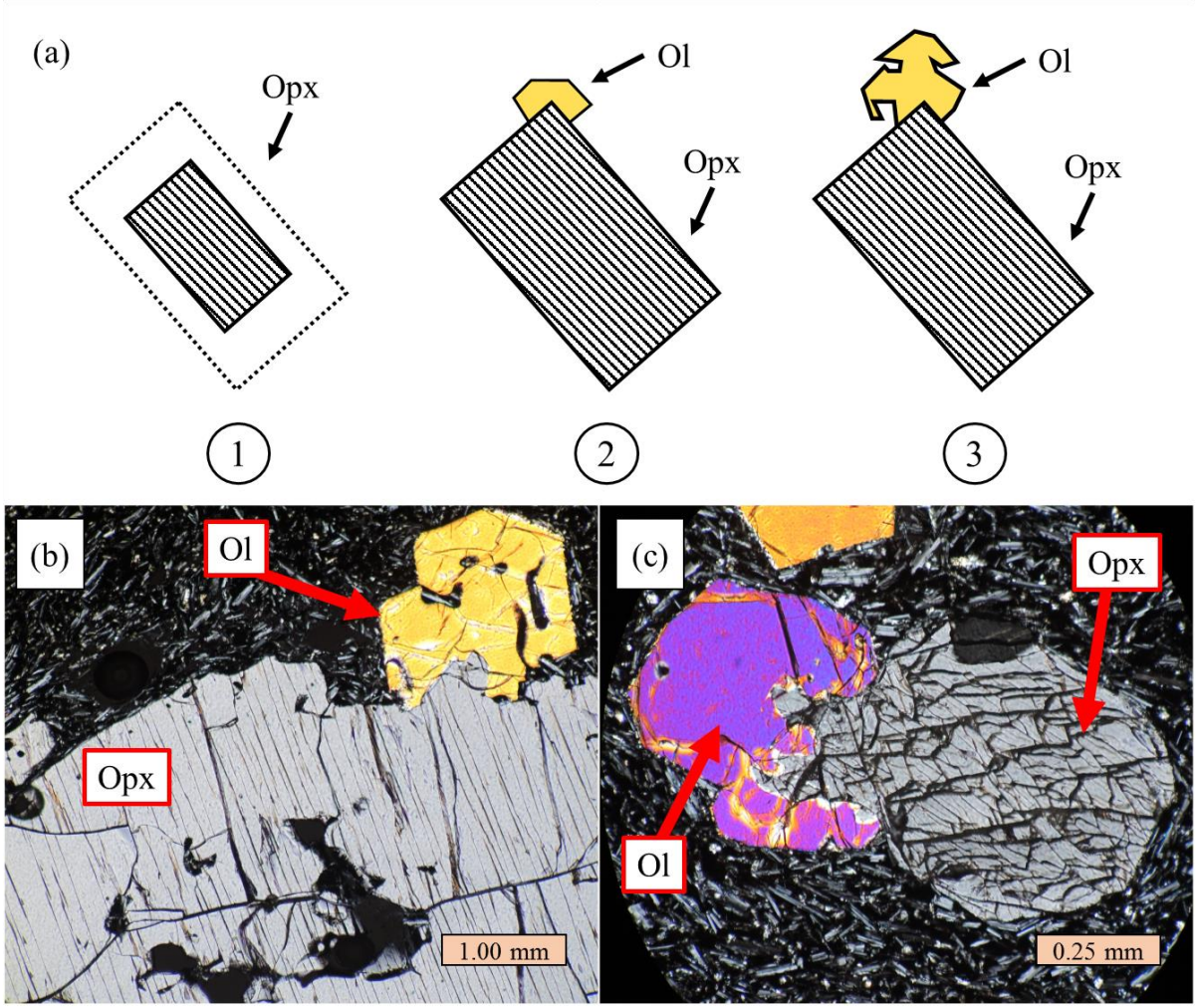

Figure 28. (a) Illustrations of Opx and Ol growth as seen in petrography; ① Growth of large euhedral Opx. ② The start of Ol formation, using Opx as a nucleation site ③ Interruption during Ol growth creates skeletal texture. Bottom images (b) and (c) are the actual Opx and Ol phenocrysts observed in Manguao Basalt.

Core Ol magnesium number $\{Mg\#^{Ol} = 100[X^{Ol}_{Mg}/(X^{Ol}_{Mg} + X^{Ol}_{Fe} + X^{Ol}_{Mn})]\}$ ranges from 71 to 83. Zoning is only observable from backscattered electron imagery (Fig. 8a-b). Majority of the crystal

interiors (core to mantle) have uniform Mg# and only the outermost edges (rim) show a distinctly lower Mg# zone (66–76; Fig. 8a). Ol with lower core Mg# (<80) also show more pronounced pyroxene reaction rims (Fig. 8b).

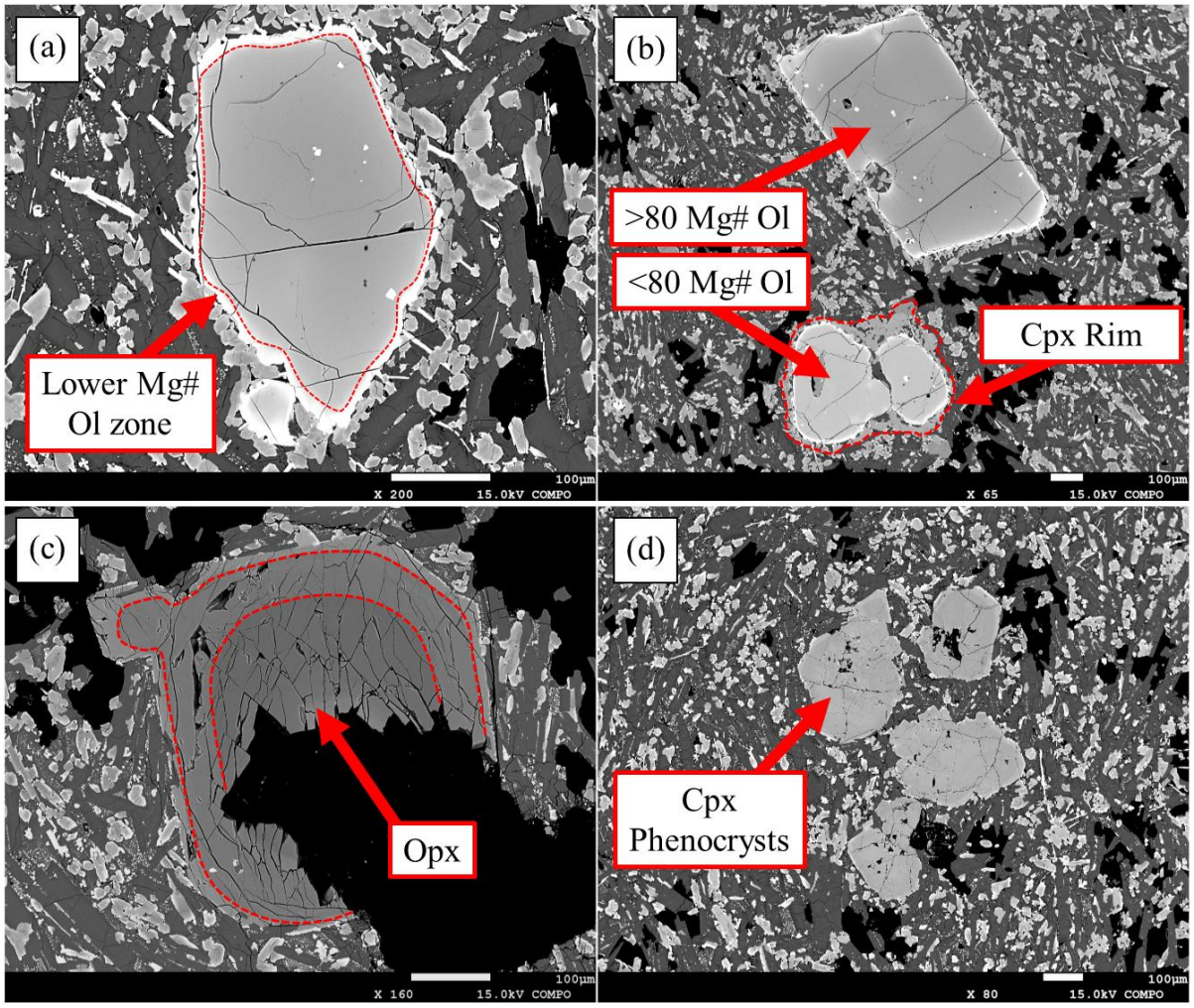

Figure 29. Backscattered electron images (BSE) of representative phenocrysts in Manguao Basalt. (a) Ol phenocryst with resorbed edges. Brighter rim attributed to a lower Mg#. (b) Two kinds of Ol present in Manguao Basalt; darker with higher Mg# (>80) and lighter with less Mg# (<80). Higher-Mg# olivines are more polygonal and rarely show pyroxene reaction rims. (c) Zones in Opx phenocrysts. Unlike regular polygonal zones, opx zoning shows smooth boundaries; indicating resorption during growth of the crystal. (d) Cpx phenocrysts with 'wispy' zones. Unlike Opx phenocrysts, Cpx commonly form clusters and rarely occur as large single crystals.

Pyroxenes

Pyroxenes exist in both phenocryst and groundmass assemblages. Pyroxenes are subdivided into two groups: (1) orthopyroxene-dominated phenocrysts, and (2) clinopyroxene-dominated groundmass.

Orthopyroxene (Opx) phenocrysts (Fig. 8c) represent the largest (i.e., with some crystals exceeding 2 mm) and highest Mg# (76–86) of any major silicate phase present. Zoning patterns observed in large Opx crystals show 'rounded' magnesian core (Mg# = 82–86) surrounded by less magnesian region (Mg# = 80–82) and least magnesian edge (Mg# = 76–80). The presence of this rounded zoning pattern possibly reflects the melt evolution and Opx resorption during crystal growth.

Clinopyroxene (Cpx) phenocrysts are smaller (100–300 μm; Fig. 8d) and less abundant than Opx. Cpx Mg# shows the widest range from 65 to 83, as it is present in both phenocryst (>80) and groundmass assemblages (<80). Like Opx, few observed Cpx phenocrysts also show evidence of earlier formation from Ol (Fig. 9a). While Opx and Ol phenocrysts occur as individual crystals, Cpx phenocrysts occur in aggregates. 'Rounded' zones are also found in Cpx phenocrysts but are not as distinct as those found in Opx.

Mineral clusters observed from petrography were identified as Cpx clusters (Fig. 5d). These clusters occur as large (>4 mm) distinct bulbous aggregates, possibly cumulate in origin. The Mg# of Cpx in the cluster varies from 65 to 83, similar with the ranges of phenocryst and groundmass Cpx.

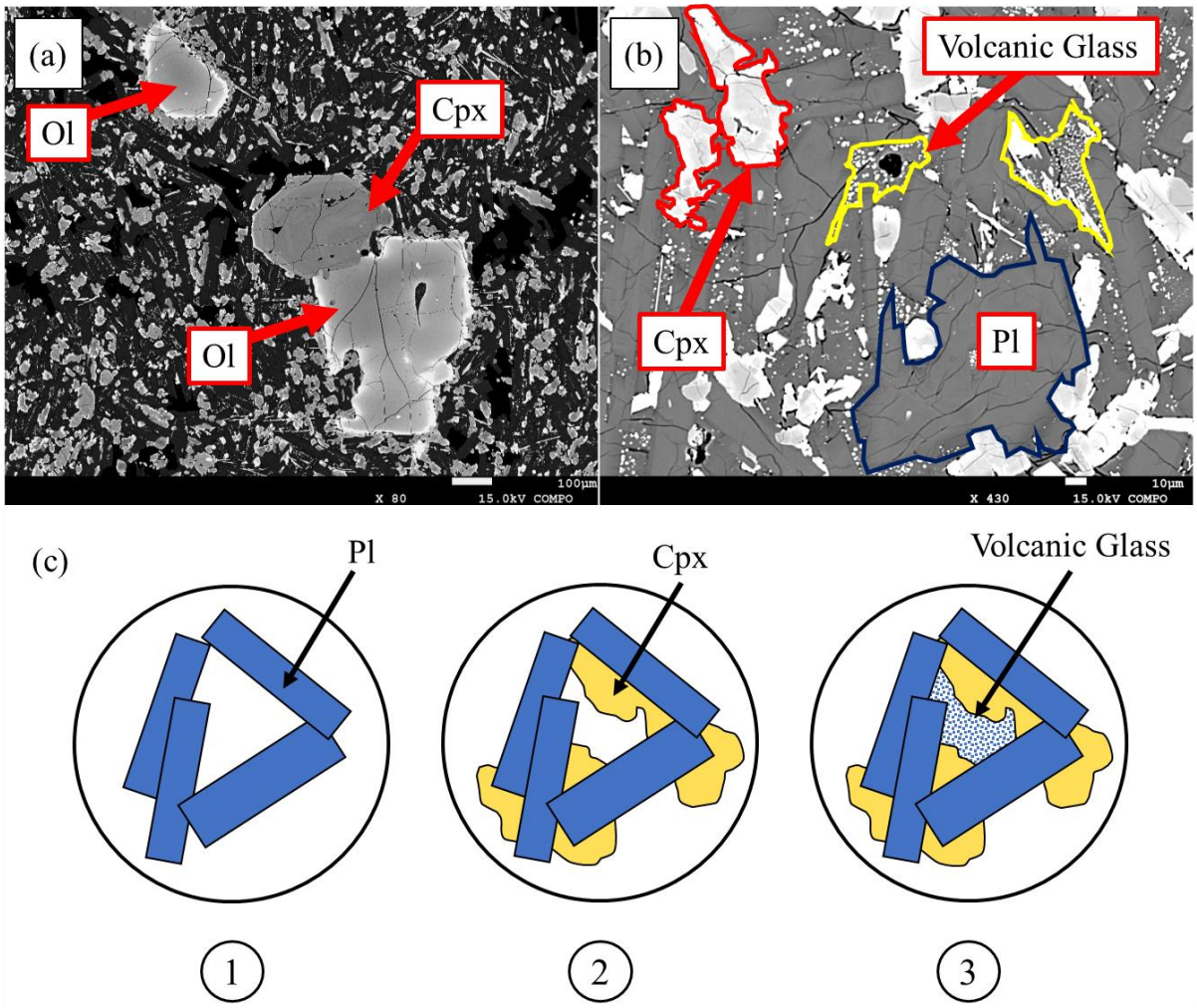

Figure 30. Backscattered electron images (BSE) of phenocrysts and groundmass components in Manguao Basalt. (a) Cpx with an 'attached' Ol. Similar with Opx phenocrysts, high-Mg# Cpx (>80) can also be observed with Ol grains partially 'engulfing' or 'attached' to it. Wispy zoning can also be observed in the interior of Cpx. (b) Groundmass components in Manguao Basalt. Pl laths dominate the groundmass. Anhedral Cpx is found between spaces of Pl laths. Blebby volcanic glass fills the interstitial spaces. (c) Illustration showing the formation of the groundmass; ① Formation of the Pl laths ② Melt trapped between laths form anhedral Cpx ③ Remaining melt forms the intersertal glass.

Plagioclase

Plagioclase (Pl) occurs as euhedral to subhedral laths dominating the microcrystalline groundmass (Fig. 9b). Crystals are unzoned and anorthite content $\{An\%^{Pl} = 100[X_{Ca}^{Pl}/(X_{Ca}^{Pl} + X_{Na}^{Pl} + X_{K}^{Pl})]\}$ ranges from 50 to 60. Pl appears to be generally restricted in the groundmass. Mineral textures of observed Pl and groundmass Cpx show earlier formation of the larger, euhedral Pl laths (Fig. 9c).

Crystallization Sequence

Based on the observed petrographic evidence, Opx and Cpx phenocrysts appear to have formed earlier than Ol. The span of Ol crystallization possibly marks the boundary between the phenocryst and groundmass formation. The skeletal textures observed in the Ol phenocrysts possibly recorded the corresponding change in the cooling rate from melt removal. On the other hand, the crystallization of Pl encompasses most of the groundmass formation. Melt trapped in between the crystal mush formed the anhedral Cpx and blebby volcanic glass. The melt parameters and conditions producing this unusual crystallization sequence (Pyroxene phenocrysts → Ol → Pl → Groundmass Cpx) were investigated further using geochemistry and MELTS simulations.

Major and Trace Element Chemistry

Average bulk major element compositions (TiO_2, Al_2O_3, FeO^t, MnO, and MgO) of Manguao Basalt samples (Table 4) show similarities with common olivine tholeiites of Wilkinson (1986). Silica (SiO_2) and alkalis (e.g., Na_2O and K_2O) are slightly higher for Manguao Basalt. The calcium (CaO) content, however, is distinctly low. Using the total-alkali-silica (TAS) diagram of Peccerillo and Taylor (1976), Manguao Basalt samples plot within the basalt to basaltic andesite fields of the subalkaline series (Fig. 10a). Miyashiro (1974) plots show the straddling of points within the boundary of tholeiitic and calc-alkaline rocks (Fig. 10b). The presence of the chert xenoliths, however, may have affected the bulk silica concentrations and shifted the plots towards the calc-alkaline field. AFM ternary diagram plots show an affinity for Fe-enrichment, characteristic of tholeiite melts (Fig. 10c).

Table 5. Major element composition of Manguao Basalt in comparison with other common basalts of Wilkinson (1986).

Manguao Basalt	No. of Analyses	SiO_2 (wt%)	TiO_2 (wt%)	Al_2O_3 (wt%)	FeO^t (wt%)	MnO (wt%)	MgO (wt%)	CaO (wt%)	Na_2O (wt%)	K_2O (wt%)	P_2O_5 (wt%)	Total
Highest Value	16	52.95	2.13	15.00	10.62	0.17	9.52	8.27	2.74	1.03	0.41	98.97
Lowest Value	16	48.37	1.94	13.69	9.05	0.14	8.03	7.72	2.46	0.55	0.28	97.61
Average		51.71	2.04	14.22	9.64	0.15	8.62	8.01	2.62	0.86	0.34	98.21
Wilkinson (1986)	No. of Analyses	SiO_2 (wt%)	TiO_2 (wt%)	Al_2O_3 (wt%)	FeO^t (wt%)	MnO (wt%)	MgO (wt%)	CaO (wt%)	Na_2O (wt%)	K_2O (wt%)	P_2O_5 (wt%)	Total
MORB-type, low K, low-Al Olivine-Tholeiite	530	50.08	1.55	15.07	9.89	0.10	8.12	11.51	2.53	0.14	0.13	98.21
MORB-type, low K, high-Al Olivine-Tholeiite	309	49.88	1.17	16.95	8.65	0.08	7.95	11.89	2.42	0.13	0.10	98.43
Olivine Tholeiite	458	49.22	2.16	14.10	11.05	0.17	8.75	10.34	2.39	0.56	0.25	97.97
Calc-Alkaline, Low-K/Na, Olivine-Basalt	395	50.15	1.35	17.89	9.23	0.14	6.57	10.05	2.82	0.76	0.21	98.32
Calc-Alkaline, Medium-K/Na, Olivine-Basalt	53	50.58	1.27	18.57	8.81	0.34	5.73	9.07	2.73	1.78	0.35	98.42

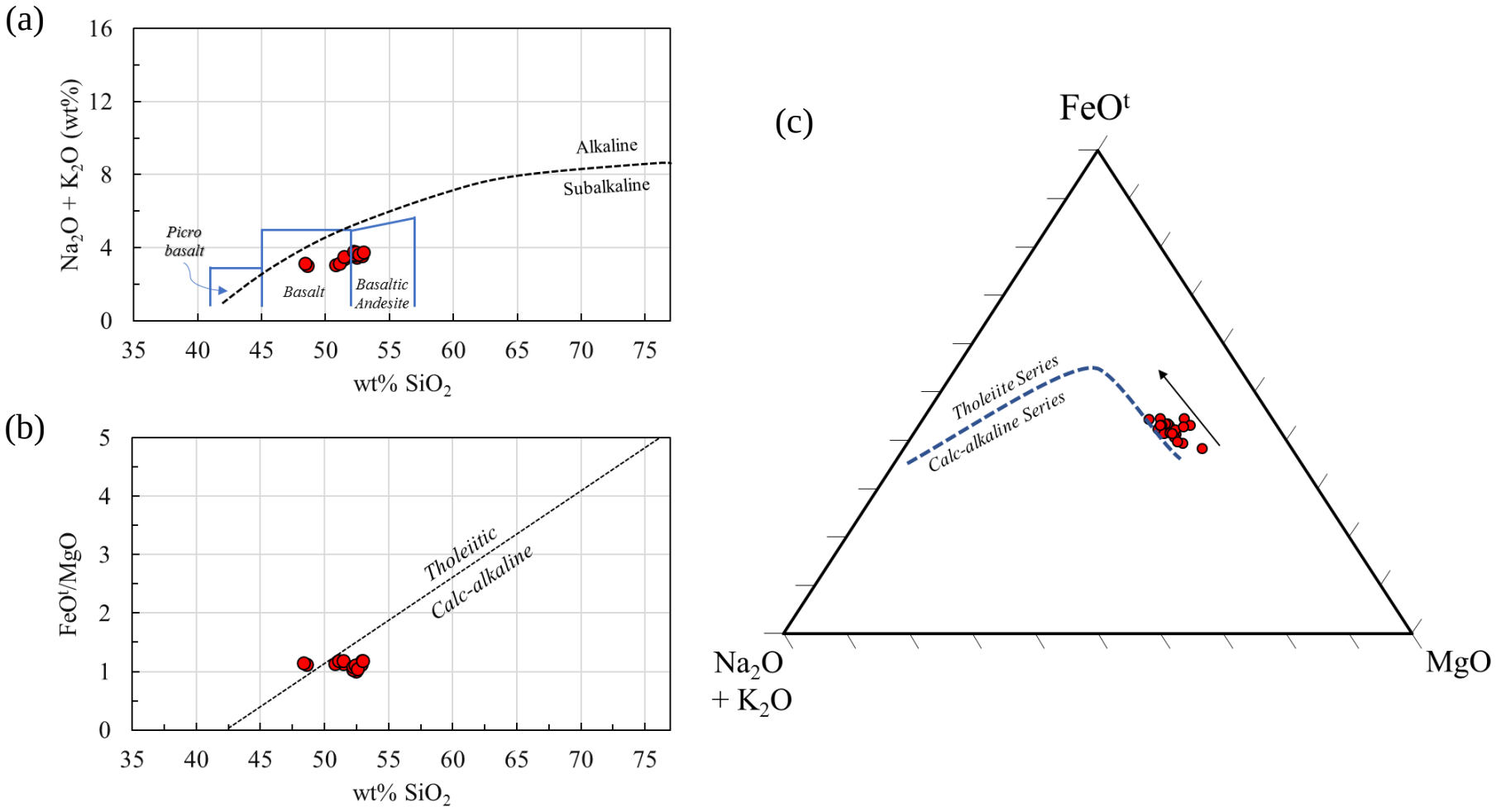

Figure 31. (a) Total Alkali vs. Silica (TAS; Peccerillo and Taylor, 1976), (b) FeO^t/MgO vs SiO_2 (Miyashiro, 1974), and (c) AFM ternary plots (Kuno, 1968) of Manguao Basalt samples. Total iron expressed as FeO^t. TAS diagram shows plotting of Manguao Basalt samples within the basalt to basaltic-andesite fields (subalkaline). Manguao Basalt plots in the Miyashiro (1974) diagram shows the 'straddling' between tholeiitic and calc-alkaline affinities. The presence of chert xenoliths, however, may have affected SiO2 bulk concentrations. AFM ternary diagram shows inclination towards Fe-enrichment; diagnostic feature of tholeiitic melts. Arrow approximates Fe-enrichment during evolution.

Whole-rock major element compositions of Manguao Basalt show increasing silica (SiO_2) and alkalis ($Na_2O + K_2O$) with decreasing MgO (Fig. 11). Total iron (FeO^t) and titanium (TiO_2), on the other hand, show a decreasing trend. More compatible trace elements (e.g., cobalt and nickel) also reflect the decreasing trend, possibly indicating the fractionation of Ol. Calcium and aluminum ratios are relatively constant, indicating the limited removal of Pl.

The whole-rock composition of Manguao Basalt is almost similar with a typical olivine basalt tholeiite. In addition, the major element trends show generic tholeiitic affinity. Therefore, producing the observed bulk composition of Manguao Basalt implies a melt source that is similar with the source of common olivine tholeiite basalts. However, the distinct low calcium content of Manguao Basalt observed from bulk compositions may be caused by the early removal of Ca-rich pyroxenes, rather than by plagioclase removal. The conditions and processes related to generating the unusual crystallization sequence were investigated further using geothermobarometers and MELTS simulations.

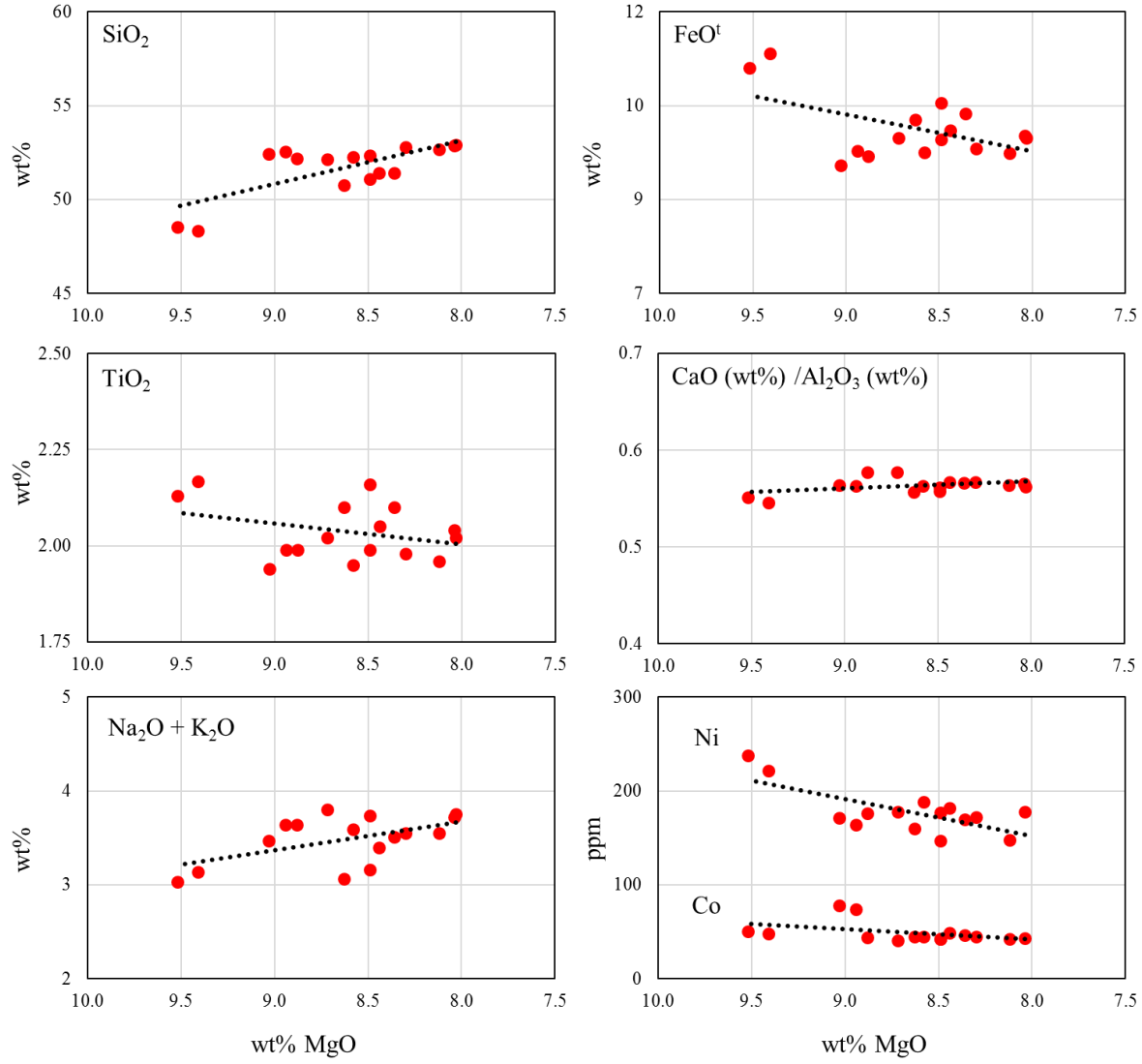

Figure 32. Selected major (SiO_2, FeO^t, TiO_2, CaO/Al_2O_3, $Na_2O + K_2O$; in wt% oxide) and trace elements (Ni and Co; in ppm) plotted on bivariate diagrams. Abscissa of all plots are in MgO (wt%). Silica (SiO_2) and alkalis ($Na_2O + K_2O$) show strong increasing trend with decreasing MgO. Total iron (FeO^t), titanium (TiO_2) and olivine-compatible trace elements (Ni and Co) show decreasing trend with decreasing MgO; possibly indicating fractionation of the ferromagnesians. CaO/Al_2O_3 ratios appear to be unaffected by decreasing MgO; possibly indicating limited plagioclase fractionation.

Pressure and Temperature Calculations

Mineral-based thermometers are consistent with the idea of early pyroxene formation (Fig. 12 and Table 5). Pressure-independent Ol-based and liquid-only thermometers (Arndt, 1977; Helz and Thornber, 1987; Putirka, 2008) show a wide range of formation temperatures (1185–1235 °C). A pressure dependent Ol thermometer from Putirka (2008) requires pressures of 1.1 to 4.6 kbar to reach this range of formation temperatures. A similar pressure-dependent Ol-based thermometer of Beattie (1993) gives a narrower temperature range (1203–1222 °C) compared with the pressure-independent thermometers. The thermometer of Beattie (1993) and aluminum-based barometers of Putirka (2008) yielded the highest obtained average Opx formation temperatures (1234–1252 °C) and pressures (3.0–5.7 kbar). P-independent Cpx thermometer of Putirka et al. (1996) shows higher average Cpx formation temperatures (1233 °C) compared with P-dependent Cpx thermometers of Nimis and Taylor (2000) and Putirka et al. (1996, 2003; 1137–1186 °C). Cpx has the widest range of formation temperatures (1103–1254 °C) as it is both present in the phenocryst and groundmass assemblages. The formation temperatures from Pl-based thermometer of Putirka (2005) show the lowest average values (1136–1154 °C).

Thermometers based on liquid-only components show a different crystallization sequence (Ol → Opx → Cpx → Pl). Ol saturation temperatures from Beattie (1993) and Yang et al. (1996) give the highest values (1200–1256 °C), while Opx saturation temperatures (Putirka, 2008) are slightly lower (1216–1243 °C). On the other hand, Cpx saturation temperatures (Putirka, 2008; 1169–1202 °C) are higher than Pl (Putirka, 2008; 1145–1167 °C), indicating an earlier formation. The discrepancies we observed in the formation temperatures are possibly related to the variables used in the respective calculations. Thermometers based on liquid-only components are more susceptible to offsets caused by small changes in bulk chemistry. Nevertheless, the formation temperatures obtained from mineral-based thermometers are consistent with the narrative of unusual crystallization sequence for Manguao Basalt.

Table 6. Calculated formation temperatures and pressures of major silicate minerals in Manguao Basalt

	Reference	Min T (°C; at 1.1 kbar) P-dependent	Max (°C; at 4.6 kbar) P-dependent	T (°C) P-independent	P (kbar)
Liquid	Ol-saturation; Helz and Thornber (1987)*			1221	
	Ol-saturation; Putirka (2008), (a) P-dependent (b) P-independent	(a) 1221	(a) 1235	(b) 1235	
	Ol-saturation; Yang et al. (1996)*	1200	1228		
	Ol-saturation; Beattie (1993)*, P-dependent	1237	1256		
	Opx-saturation; Putirka (2008)	1216	1243		
	Cpx-saturation; Putirka (2008)	1169	1202		
	Pl-saturation; Putirka (2005)*	1145	1167		
Ol	Arndt (1977)*			1185 (ave; 1136–1238)	
	Beattie (1993)*	1203 (ave; 1201–1205)	1222 (ave; 1219–1224)		
Opx	Beattie (1993)*	1234 (ave; 1219–1243)	1252 (ave; 1236–1261)		
	Putirka (2008): Opx-Liq				3.4–3.7
	Putirka (2008): Opx-Liq				3.0–3.7
	Putirka (2008): Opx-only				4.9–5.7
Cpx	Putirka et al. (1996)*			1233 (ave; 1142–1254)	
	Nimis and Taylor (2000)*	1157 (ave; 1104–1182)	1186 (ave; 1133–1212)		
	Putirka et al. (1996; 2003)*	1137 (ave; 1103–1152)	1156 (ave; 1121–1172)		
Pl	Putirka (2005)	1136 (ave; 1129–1140)	1154 (ave; 1146–1157)		

*Expressions are available and calibrated in Putirka (2008)

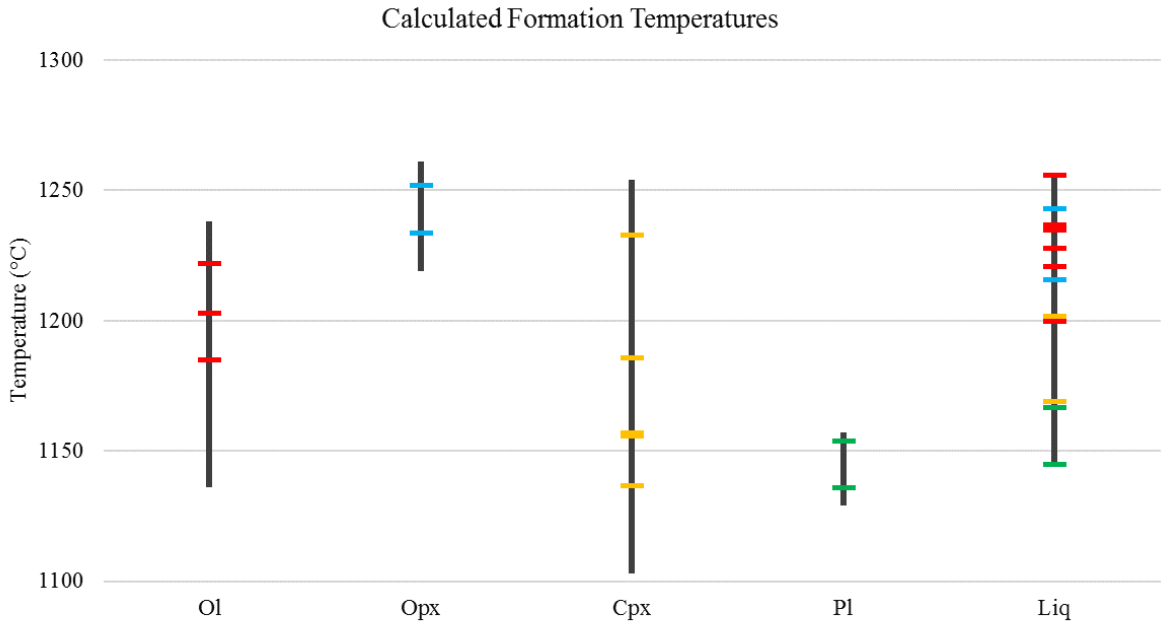

Figure 33. Summary of calculated formation temperatures of all major phases present in Manguao Basalt (P-dependent calculations were done for 1.1 and 4.6 kbar). Dark vertical bars indicate the temperature range of all calculations done for each component. Colored horizontal bars mark the average temperatures derived from different thermometric equations (details in text; summary in Table 4). A separate column is introduced for calculations involving liquid-only components (Liq). Mineral-based thermometers (Ol, Opx, Cpx and Pl) are consistent with the idea of early pyroxene formation. Thermometers based on liquid-only components show a different crystallization sequence (Ol →Opx → Cpx → Pl).

Discussion

Manguao Basalt samples are characterized by an Ol-dominated phenocryst assemblage, with minor Opx and Cpx. Groundmass is composed of Pl and pyroxenes, set in an intersertal texture. While this modal assemblage is common for basalts, petrographic evidence from observed Opx-Ol and Cpx-Ol relationships show the earlier formation of the pyroxenes. In addition, the calculated formation temperatures of pyroxene phenocrysts are also higher compared to Ol. This unusual crystallization sequence observed in Manguao Basalt implies possible partial melting and fractionation at high pressures. Experimental data from Green and Ringwood (1964) demonstrate the emergence of primary Opx in the liquidus phase at pressures of partial melting reaching 15 kbar. The crystallization of this high-pressure partial melt produces "aluminous orthopyroxene and not olivine as the first crystals"

(Green and Ringwood, 1964). The succeeding discussions focus on the potential of these high-pressure partial melts in producing the unusual crystallization sequence observed in Manguao Basalt.

Simulations of Mantle Melting

Experimental investigations on natural basalts of Green and Ringwood (1967) show that magma compositions are not determined by the depth of partial melting, but by the depth of magma segregation. In this study, we simulated two different scenarios of fertile and depleted mantle melting: (1) keeping the liquid in equilibrium with source, and (2) immediate removal of the forming melt.

Partial melting of both fertile and depleted mantle sources produced significant melt fractions as soon as the pressures drop below 11 kbar (Fig. 13). Pyroxenes are the dominant contributors to the melting fraction. Resulting primitive melt compositions are all similar (Table 3), consistent with the study of Green and Ringwood (1967). Comparing these with the average whole-rock composition of Manguao Basalt, the primitive liquids have noticeably higher CaO and MgO, but lower in titanium (TiO_2) and total iron (FeO^t).

Simulations of Melt Crystallization

The generated primitive mantle melts are too enriched in pyroxene components (i.e., higher CaO and MgO contents) to resemble the composition of Manguao Basalt. Following the idea of Green and Ringwood (1964), Opx will form earlier than Ol when the liquid crystallizes at depth. Therefore, the formation and removal of these early pyroxenes should generate an evolved melt with a composition similar to Manguao Basalt. This study simulated equilibrium and fractional crystallization of all four (4) primitive melts.

All simulations of crystallization produce evolved liquids with compositions similar to Manguao Basalt (Fig. 14). The crystallization of the pyroxenes and Ol generate trends of melt evolution that reach Manguao Basalt compositions around 1230 to 1260 °C. However, even though all crystallization simulations reach the Manguao Basalt compositions, the details from mineral chemistry of the early crystals show some remarkable differences.

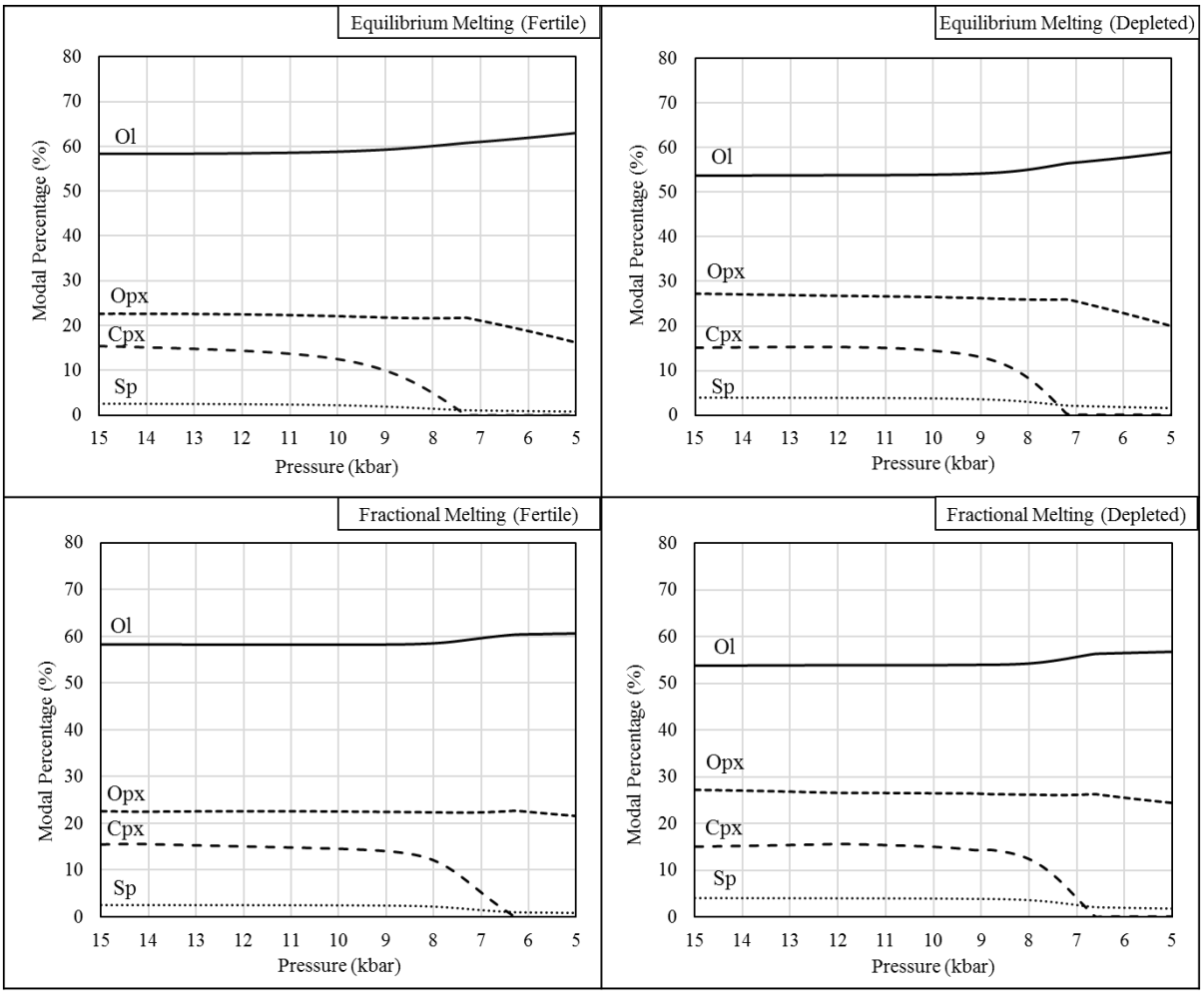

Figure 34. Evolution of fertile and depleted mantle source rocks during decompression melting (15–5 kbar, 1350 °C, and QFM buffer). Melting is controlled primarily by Cpx. Complete melting of Cpx happens between 6 to 8 kbar. Opx melting commences right after (until pressure reaches 5 kbar).

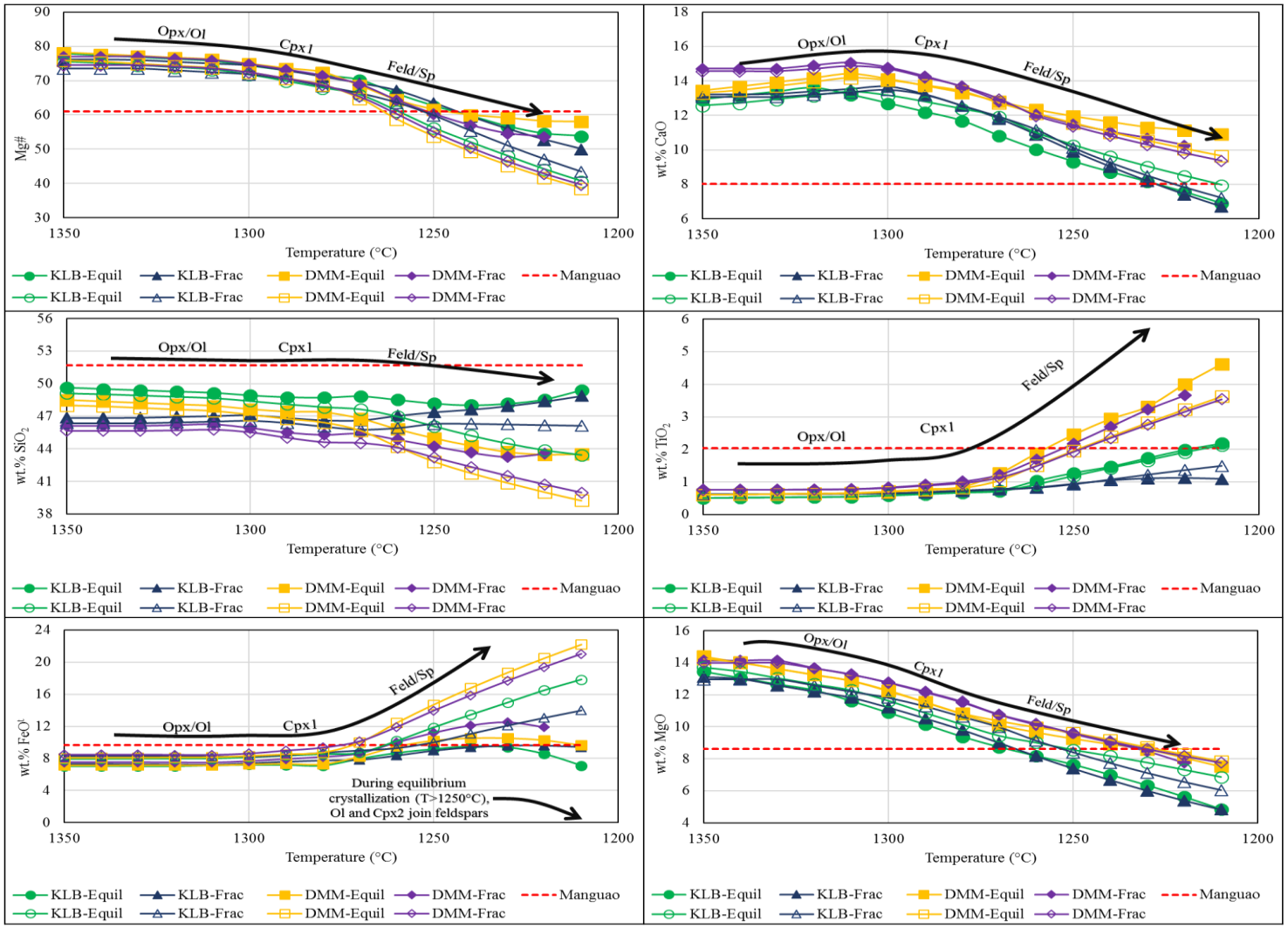

Figure 35. Melt evolution of primitive liquids during equilibrium and fractional crystallization. Melt evolution is recorded from 1350 to 1200 °C. Red dashed line on each plot shows average Manguao Basalt composition. Major element curves with filled symbols indicate melts evolving from equilibrium crystallization. Hollow symbols indicate melts evolving from fractional crystallization. Evolving melts reach similarities with Manguao Basalt composition at 1230 to 1260 °C. Dominant mineral species crystallizing/fractionated at each temperature interval is shown beside the thick arrow.

Mineral Chemistry from Fractional Crystallization

All simulations of fractional crystallization were able to produce Opx as the first crystals (Fig. 15). Opx is immediately followed by Ol in most sequences (from 1330 °C), then by Cpx (1310 °C), and finally by feldspars (1260–1280 °C). Although these simulated crystallization sequences were able to show the early Opx formation, the respective simulated Opx mineral compositions do not appear to show similarities with Manguao Basalt Opx (Table 6). Manguao Basalt Opx have lower MgO and higher total iron (FeOt) than the simulated Opx. Furthermore, the temperature window of Opx formation under fractional crystallization is short (1310–1340 °C) and higher than the calculated formation temperatures of Manguao Basalt Opx (1230–1260 °C). Hence, the immediate removal of the early-formed crystals might not be a likely scenario for Manguao Basalt.

Table 7. Evolution of Opx composition during fractional crystallization

	Opx composition during fractional crystallization (Equilibrium melt from fertile Source)					Opx composition during fractional crystallization (Equilibrium melt from depleted source)				
T (°C)	wt% SiO_2	wt% FeO^t	wt% MgO	wt% CaO	Mg#	wt% SiO_2	wt% FeO^t	wt% MgO	wt% CaO	Mg#
1340	56.09	6.55	32.91	1.80	89.95	55.89	6.58	32.84	1.75	89.90
1330	55.98	6.74	32.62	1.95	89.61	55.77	6.76	32.56	1.89	89.57
1320	55.87	6.93	32.32	2.12	89.26	55.65	6.95	32.26	2.05	89.21
1310	55.75	7.13	31.99	2.32	88.89	55.53	7.15	31.95	2.23	88.85
	Opx composition during fractional crystallization (Fractionated melt from fertile source)					Opx composition during fractional crystallization (Fractionated melt from depleted source)				
T (°C)	wt% SiO_2	wt% FeO^t	wt% MgO	wt% CaO	Mg#	wt% SiO_2	wt% FeO^t	wt% MgO	wt% CaO	Mg#
1340	56.09	6.55	32.91	1.80	89.95	55.89	6.58	32.84	1.75	89.90
1330	55.98	6.74	32.62	1.95	89.61	55.77	6.76	32.56	1.89	89.57
1320	55.87	6.93	32.32	2.12	89.26	55.65	6.95	32.26	2.05	89.21
1310	55.75	7.13	31.99	2.32	88.89	55.53	7.15	31.95	2.23	88.85

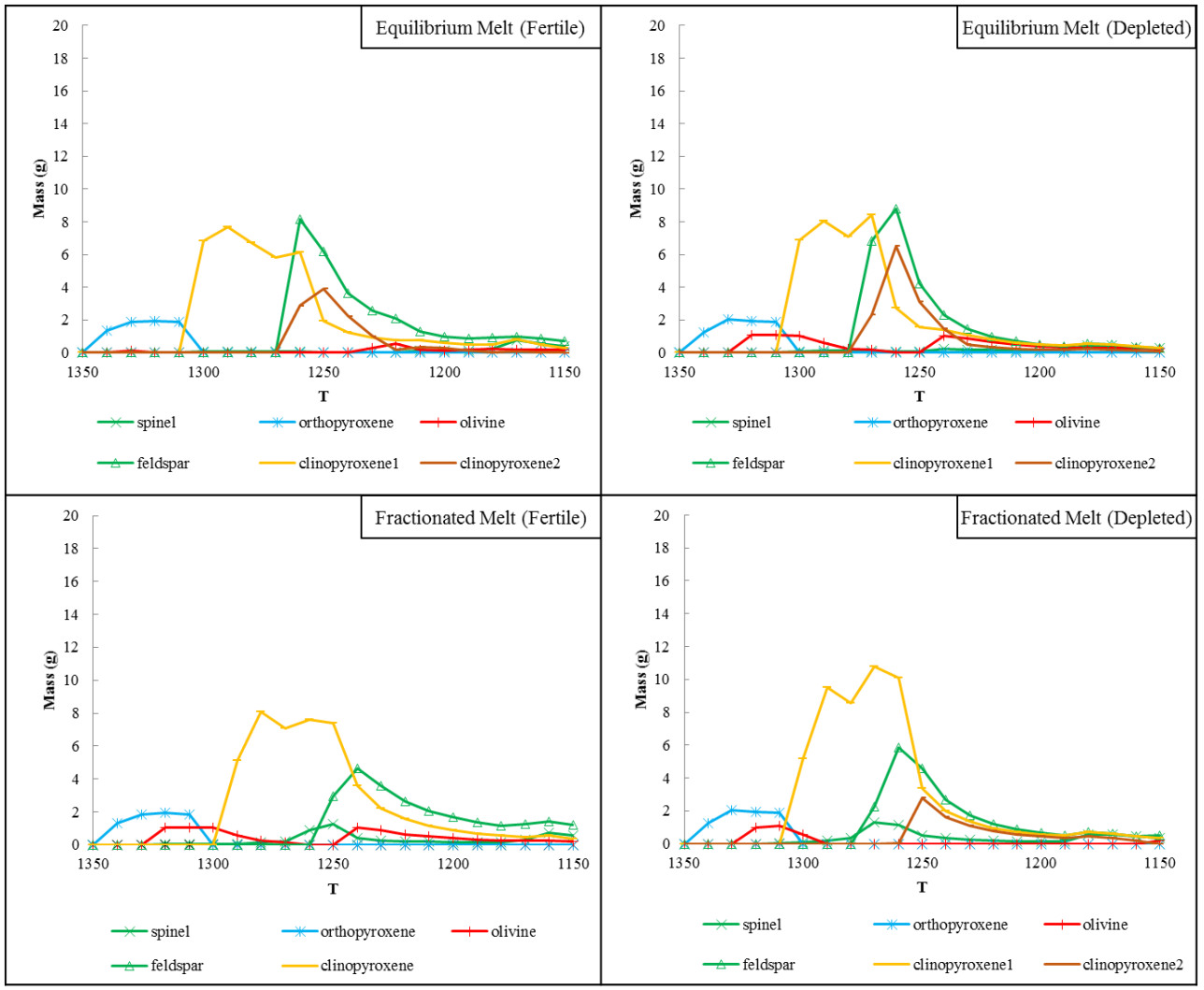

Figure 36. Fractional Crystallization of different primitive melts derived from fertile and depleted mantle sources. Crystallization commences at 1350 °C and maintains isobaric (5 kbar) condition and QFM buffer. All melts initially crystallize orthopyroxene. 'Clinopyroxene1' refers to high-Ca clinopyroxenes forming at higher temperatures. 'Clinopyroxene2' refers to low-Ca clinopyroxenes.

Mineral Chemistry from Equilibrium Crystallization

Simulations of equilibrium crystallization produce either Opx or Ol as the first crystals (Fig. 16). Melts that were kept at equilibrium with the source during mantle melting were able to form Opx earlier than Ol. Melts that were fractionated from source, on the other hand, crystallize Ol first. The crystallization of Opx or Ol continues until 1300 to 1310 °C, where Cpx starts to form. Feldspars appear last in the sequence (1260–1280 °C).

The formation of Opx and Cpx during the initial stages of crystallization is consistent with our earlier claim on the possibility of earlier pyroxene crystallization. Simulated Opx and Cpx from equilibrium crystallization show compositional similarities with those observed in Manguao Basalt (Table 7 and 8). Major oxide compositions (SiO_2, FeO^t, MgO and CaO) of simulated Opx reach similiarities with Manguao Basalt Opx at crystallization temperatures reaching 1290 to 1270°C, close to the highest temperature obtained from Manguao Basalt Opx (~ 1260 °C; P-dependent thermometer of Beattie, 1993 at 4.6 kbar). Simulated Cpx (for high Mg#; >80) reaches compositional similarities with Manguao Basalt Cpx (phenocrysts) at crystallization temperatures of 1230 to 1260 °C. The Cpx formation temperatures calculated using the P-independent thermometer of Putirka et al. (1996) shows the closest average value (1233 °C).

On the other hand, the formation of the groundmass components cannot be reconciled with any of the simulations. This is because the simulation assumed complete crystallization at isobaric conditions (5 kbar). Nevertheless, the simulations proved that keeping the equilibrium between the melt and the forming crystals is critical in producing the early Opx and Cpx in Manguao Basalt.

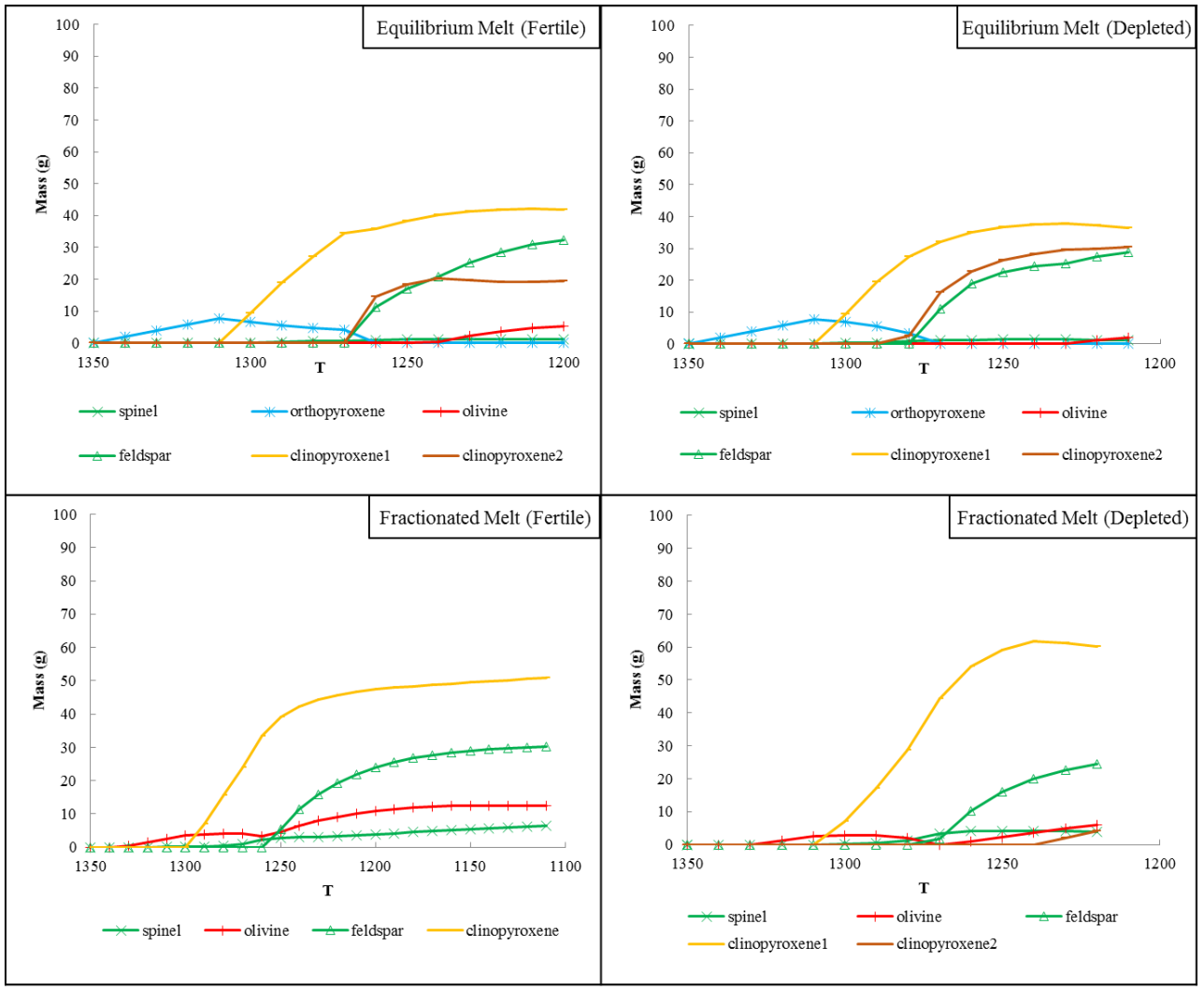

Figure 37. Equilibrium Crystallization of different primitive melts derived from fertile and depleted mantle sources. Crystallization commences at 1350 °C and maintains isobaric (5 kbar) condition and QFM buffer. Primitive melts that remained in equilibrium with the source produce Opx as the first crystals. On the other hand, primitive melts fractionated from the source produce Ol as the first crystals. 'Clinopyroxene1' refers to high-Ca clinopyroxenes forming at higher temperatures. 'Clinopyroxene2' refers to low-Ca clinopyroxenes.

Table 8. Evolution of Opx composition during equilibrium crystallization

Opx Composition during Equilibrium Crystallization (Equilibrium Melt from Fertile Source)					
T (°C)	wt% SiO_2	wt% FeO^t	wt% MgO	wt% CaO	Mg#
1340	56.19	6.23	33.13	1.82	90.46
1330	56.09	6.39	32.86	1.97	90.15
1320	55.98	6.57	32.57	2.14	89.83
1310	55.87	6.75	32.25	2.34	89.49
1300	55.58	7.07	31.97	2.24	88.97
1290	55.24	7.40	31.69	2.11	88.41
1280	54.90	7.74	31.39	1.99	87.84
1270*	54.57	8.10	31.09	1.88	87.26
1180*	53.27	11.67	28.62	1.60	81.39
1170	53.21	12.09	28.31	1.61	80.67
1160	53.20	12.23	28.24	1.59	80.47
Opx Composition during Equilibrium Crystallization (Equilibrium Melt from Depleted Source)					
T (°C)	wt% SiO_2	wt% FeO^t	wt% MgO	wt% CaO	Mg#
1340	55.99	6.25	33.06	1.77	90.40
1330	55.88	6.43	32.79	1.91	90.09
1320	55.77	6.60	32.50	2.06	89.77
1310	55.65	6.79	32.20	2.25	89.43
1300	55.33	7.10	31.90	2.15	88.90
1290	54.95	7.45	31.59	2.01	88.32
1280	54.58	7.79	31.28	1.89	87.74
1270*	53.07	11.25	28.83	1.57	82.04
1180*	53.01	11.67	28.53	1.58	81.34
1170	52.95	12.10	28.22	1.58	80.61
1160	52.92	12.33	28.07	1.57	80.24

*Opx formation below 1270 °C is replaced by low-Ca Cpx in simulations. Opx reemerges in the crystallizing phase from 1180 °C

Table 9. Evolution of Cpx composition during equilibrium crystallization

T (°C)	Cpx composition during equilibrium crystallization (Equilibrium melt from fertile source) wt% SiO_2	wt% FeO^t	wt% MgO	wt% CaO	Mg#	Cpx composition during equilibrium crystallization (Equilibrium melt from depleted source) wt% SiO_2	wt% FeO^t	wt% MgO	wt% CaO	Mg#
1260	51.14	6.96	19.02	16.04	82.96	50.55	7.34	18.61	16.18	81.87
1250	50.79	7.28	18.55	16.16	81.95	50.17	7.60	18.12	16.40	80.94
1240	50.49	7.54	18.12	16.31	81.08	49.87	7.74	17.73	16.65	80.34
1230	50.19	7.87	17.68	16.44	80.01	49.65	7.77	17.43	16.90	79.99
1220	49.89	8.14	17.27	16.62	79.10	49.38	7.86	17.10	17.18	79.49
1210	49.64	8.27	16.92	16.84	78.49	49.15	7.86	16.82	17.48	79.23
1200	49.49	8.27	16.68	17.07	78.24	49.00	7.80	16.61	17.74	79.16
1190	49.47	8.18	16.56	17.26	78.31	48.94	7.94	16.42	17.84	78.67
1180	49.39	8.35	16.34	17.35	77.72	48.87	8.11	16.21	17.92	78.10
1170	49.34	8.50	16.13	17.43	77.18	48.81	8.28	16.00	18.01	77.51
1160	49.28	8.43	15.92	17.72	77.12	48.74	8.27	15.80	18.23	77.30
1150	49.24	8.30	15.73	18.00	77.16	48.68	8.16	15.62	18.52	77.34
T (°C)	Cpx composition during equilibrium crystallization (Fractionated melt from fertile source) wt% SiO_2	wt% FeO^t	wt% MgO	wt% CaO	Mg#	Cpx composition during equilibrium crystallization (Fractionated melt from depleted source) wt% SiO_2	wt% FeO^t	wt% MgO	wt% CaO	Mg#
1260	50.15	5.51	16.65	19.57	84.36	50.17	6.91	17.96	17.06	82.25
1250	49.92	5.93	16.43	19.34	83.19	49.83	7.51	17.70	16.75	80.78
1240	49.63	6.29	16.08	19.31	82.00	49.47	7.99	17.37	16.62	79.49
1230	49.34	6.60	15.72	19.34	80.93	49.06	8.27	16.89	16.84	78.44
1220	49.08	6.85	15.36	19.42	79.98	48.70	8.43	16.47	17.11	77.71
1210	48.85	7.05	15.02	19.53	79.16	48.54	8.40	16.24	17.35	77.50
1200	48.66	7.18	14.71	19.66	78.49	48.54	8.32	16.14	17.53	77.58
1190	48.52	7.27	14.43	19.80	77.96	48.54	8.23	16.05	17.71	77.67
1180	48.42	7.31	14.19	19.95	77.57	48.53	8.26	15.92	17.83	77.46
1170	48.35	7.32	13.98	20.08	77.29	48.50	8.26	15.73	18.03	77.25
1160	48.32	7.30	13.80	20.21	77.10	48.47	8.16	15.56	18.29	77.27
1150	48.30	7.27	13.64	20.32	76.98	48.45	8.06	15.41	18.54	77.31

Akita University

Summary of results and simulations

Petrographic evidence indicates the unusual earlier formation of pyroxenes from Ol. The whole-rock major element composition of Manguao Basalt show similarities with common olivine basalt tholeiites of Wilkinson (1986). Our initial assumptions on the MELTS parameters and conditions were based on the geologic history of the PCB (i.e., limited magmatism in the region making the underlying mantle fertile), the present tectonic setup of Palawan (i.e., absence of subduction and presence of melting at upper mantle depths), and the magmatic history of the region (i.e., deep-seated melts generating the heat for Kapoas Granite formation; Encarnación and Mukasa, 1997).

The simulations done in this study provided some insights on melt formation and magmatic evolution processes responsible for the formation of Manguao Basalt:

(1) The depressurization melting of fertile (KLB-1; Davis et al., 2009) or depleted mantle source (Workman and Hart, 2005) at similar conditions (Ti = 1350 °C, starting pressure of 15 kbar and QFM buffer) produces melts with similar compositions. The resulting bulk compositions of these primitive melts are more enriched in pyroxene components (e.g., Ca and Mg) when compared to Manguao Basalt. This implies that fractionation is necessary (i.e., crystallization and removal of the early pyroxenes) to produce an evolved liquid similar with Manguao Basalt.

(2) Both equilibrium and fractional crystallization (at isobaric conditions) can generate evolved liquids that are similar with Manguao Basalt compositions. The early crystallization of the ferromagnesian minerals sufficiently evolved the remaining liquid to achieve similarities with Manguao Basalt compositions.

(3) Although different simulations show the numerous possibilities of replicating Manguao Basalt composition, the details on the mineral chemistry show the notable differences. Both equilibrium and fractional crystallization were able to produce Opx as the first crystals. However, only the equilibrated melts were able to produce Opx and Cpx with compositions similar with those observed in Manguao

Akita University

Basalt. This implies the importance of maintaining the source-melt equilibrium at some point during the formation of the first crystals.

A model for the origin of Manguao Basalt

In this study, we propose the concept of magmatic underplating as a model for visualizing the conditions and processes in the formation of Manguao Basalt (Fig. 17). The model effectively encompasses key features presented:

(1) The partial melting of the upper mantle peridotite at high pressures produces primitive melts of basaltic composition. Crystallization of these basaltic liquids at depth would produce Opx as the first crystals.

(2) The ponding of the basaltic magma at Moho depths is critical for maintaining the equilibrium between the source and melt. Melt residency at such depths is also reflected in the barometric calculations done on Opx chemistry (~ 5 kbar). Assuming a normal continental lithostatic pressure gradient (24.5 MPa/km; Cas and Simmons, 2018), this translates to approximate depths of 20 km. Geophysical investigation of the Moho region by Liu et al. (2014) shows 20 to 25 km Moho depth beneath the PCB.

(3) The crystallization of the primitive melt produces an evolved liquid similar with Manguao Basalt. The removal of the early solids depletes the liquid of pyroxene components. The corresponding magmatic evolution is recorded by the rounded zoning found in Opx and Cpx phenocrysts.

(4) Ol formation represents the subsequent crystallization from the evolved melt. Our initial assumptions on crystallization (i.e., isobaric) were made to simplify the conditions during formation of the first crystals. Hence, melt composition and prevalent conditions from Ol crystallization may no longer be represented by the simulations. The prevalent skeletal features observed in Ol phenocrysts, in addition, possibly reflect such melt removal.

(5) The model for magmatic underplating also applies to other igneous units found in the north Palawan region. The study of Encarnación and Mukasa (1997) links the presence of 'widespread basaltic volcanism' with the formation of Capoas Granite. Seismic investigations of Fan et al. (2017) reported the occurrence of low velocity (P-wave) regions that may be connected to melt emplaced at the Moho.

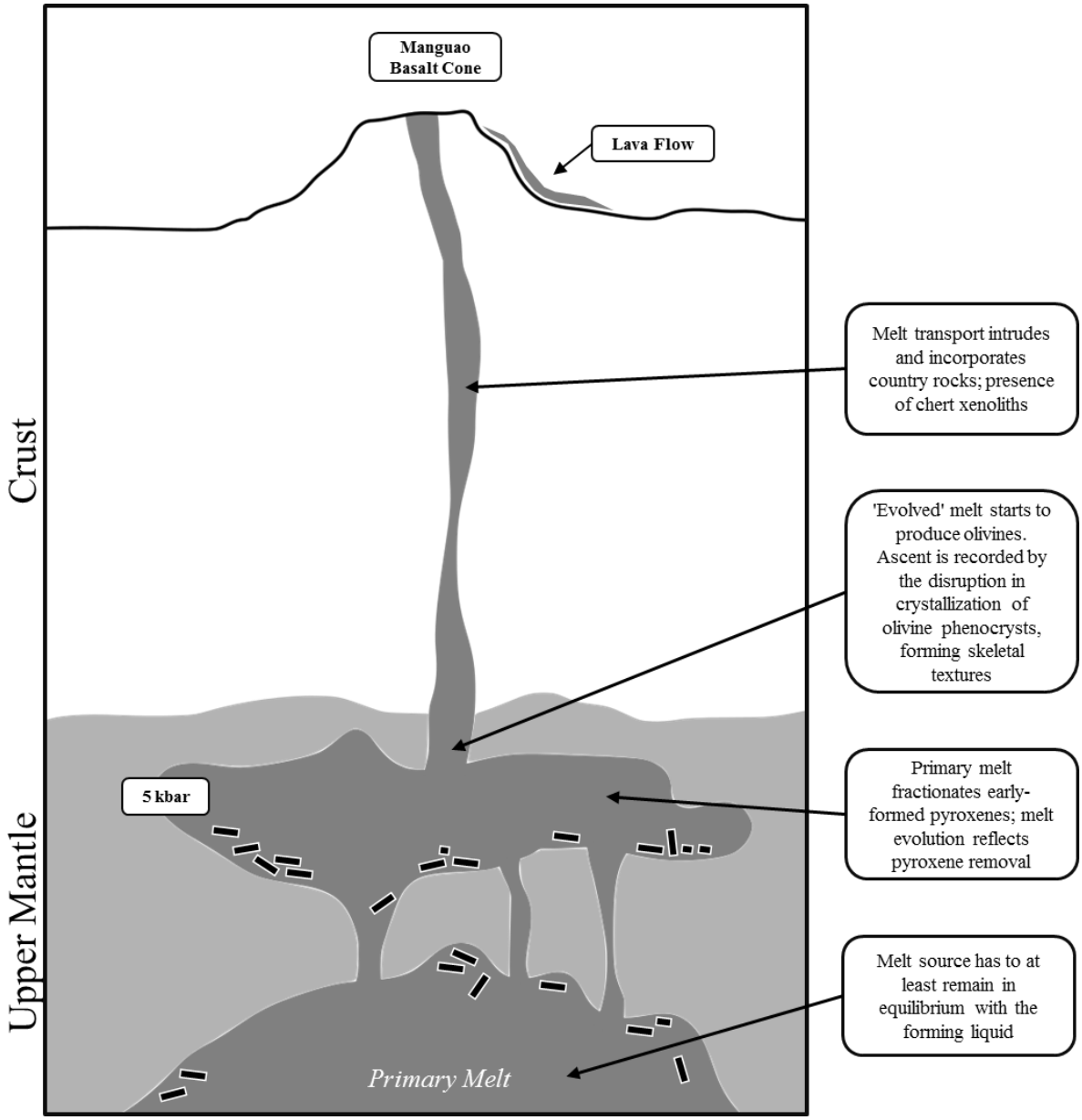

Figure 38. A model for magmatic underplating beneath Palawan microcontinent. Maintaining equilibrium conditions between the source and forming melt produces pyroxenes similar with those observed in Manguao Basalt. Subsequent crystallization and fractionation are necessary for producing evolved character of melt reflected by later-formed phases (e.g., olivine and plagioclase).

Conclusions

Manguao Basalt is a basalt-basaltic andesite lava field located on the northeast tip of Palawan, Philippines. Petrography shows samples are Ol-phyric with minor pyroxenes, set in a Pl-dominated groundmass. The petrogenesis of Manguao Basalt, in this study, is constrained by the following conditions:

(1) Manguao Basalt major element compositions show trend and affinity typical of tholeiitic melts. Major element bivariate diagrams reflect early fractionation of Ol and limited fractionation of later formed phases (e.g., Pl).

(2) Pyroxenes precede Ol in the crystallization sequence based on the evidence from petrography, mineral chemistry, and thermometry.

(3) Decompression melting of fertile or depleted mantle source produces pyroxene-saturated liquids. Major element compositions of simulated melts are very similar regardless of whether the liquid remained in equilibrium with the source. Maintaining the equilibrium between source and formed melt, however, is essential for producing Opx and Cpx similar with those observed in Manguao Basalt.

(4) Equilibrium or fractional crystallization of simulated primitive melts produce evolved liquids that reach similarities with Manguao Basalt bulk composition at 1230 to 1260 °C.

(5) Fractionation of early-formed crystals results in significant melt evolution (i.e., Ca depletion from Cpx removal) that is essential prior to later crystallization of Ol and groundmass phases.

(5) Magmatic underplating provides an excellent model for melt residency and visualizing crystallization and fractionation of melt beneath Palawan microcontinent.

References

Almasco, J.N., Rodolfo, K., Fuller, M. and Frost, G. (2000) Paleomagnetism of Palawan, Philippines. Journal of Asian Earth Sciences, 18, 369–389.

Arndt, N.T. (1977) The partitioning of nickel between olivine and ultrabasic and basic komatiite liquids. Carnegie Institution of Washington Year Book, 76, 553–557.

Aurelio, M. (2000) Tectonics of the Philippines revisited. Journal of the Geological Society of the Philippines, 55, 119–183.

Aurelio, M.A., Peña, R.E. and Taguibao, K.J.L. (2013) Sculpting the Philippine archipelago since the Cretaceous through rifting, oceanic spreading, subduction, obduction, collision and strike-slip faulting: Contribution to IGMA5000. Journal of Asian Earth Sciences, 72, 102–107.

Beattie, P. (1993) Olivine-melt and orthopyroxene-melt equilibria. Contributions to Mineralogy and Petrology, 115, 103–111.

Cas, R.A.F. and Simmons, J.M. (2018) Why Deep-Water Eruptions Are So Different From Subaerial Eruptions, Frontiers in Earth Science, 6(198), 1–21.

Davis, F.A., Tangeman, J.A., Tenner, T.J. and Hirschmann, M.M. (2009) The composition of KLB-1 peridotite. American Mineralogist, 94, 176–180.

Deer, W.A., Howie, R.A. and Zussman, J. (2013) An introduction to the Rock-forming Minerals. pp. 498, Longman, London.

Encarnación, J. and Mukasa, S.B. (1997) Age and geochemistry of an "anorogenic" crustal melt and implications for I-type granite petrogenesis. Lithos, 42, 1–13.

Fan, J., Zhao, D., Dong, D. and Zhang, G. (2017) P-wave tomography of subduction zones around the central Philippines and its geodynamic implications. Journal of Asian Earth Sciences, 146, 76–89.

Fontaine, H. (1979) Note on the Geology of the Calamian Islands, North Palawan, Philippines. Economic and Social Commision for Asia and the Pacific-Coordinating Committee for Geosciences Programmes Newsletter, 6, 40–47.

Ghiorso, M.S., Hirshcmann, M.M., Reiners, P.W., Kress V.C. (2002) The pMELTS: a revision of MELTS for improved calculation of phase relations and major element partitioning related to partial melting of the mantle to 3 GPa. Geochemistry Geophysics Geosystems, 3, 1–36.

Ghiorso, M.S. and Gualda, G.A.R. (2015) An H_2O–CO_2 mixed fluid saturation model compatible with rhyolite-MELTS. Contributions to Mineralogy and Petrology, 169(53), 1–30.

Green, D.H. and Ringwood, A.E. (1964) Fractionation of Basalt Magmas at High Pressures. Nature, 201, 1276–1279.

Green, D.H. and Ringwood, A.E. (1967) The genesis of basaltic magmas. Contributions to Mineralogy and Petrology, 15, 103–190.

Gualda, G.A.R., Ghiorso, M.S., Lemons, R.V. and Carley, T.L. (2012) Rhyolite-MELTS: A modified calibration of MELTS optimized for silica-rich, fluid-bearing magmatic systems. Journal of Petrology, 53, 875–890.

Guan, D., Ke, X. and Wang, Y. (2016) Basement structures of East and South China Seas and adjacent regions from gravity inversion. Journal of Asian Earth Sciences, 117, 242–255.

Hall, R. (1997) Cenozoic plate tectonic reconstructions of SE Asia. Geological Society, London, Special Publications, 126, 11–23.

Hall, R. (2002) Cenozoic geological and plate tectonic evolution of SE Asia and the SW Pacific: Computer-based reconstructions, model and animations. Journal of Asian Earth Sciences, 20, 353–431.

Helz, R.T. and Thornber, C.R. (1987) Geothermometry of Kilauea Iki lava lake, Hawaii. Bulletin of Volcanology, 49, 651–668.

Hirose, K. and Kushiro, I. (1993) Partial melting of dry peridotites at high pressures: Determination of compositions of melts segregated from peridotite using aggregates of diamond. Earth and Planetary Science Letters, 114, 477–489.

Holloway, N.H. (1982) North Palawan block, Philippines – its relation to Asian mainland and role in evolution of South China Sea. The American Association of Petroleum Geologists Bulletin, 66, 1355–1383.

Metal Mining Agency of Japan – Japan International Cooperation Agency (MMAJ-JICA). (1990) Report on the Mineral Exploration, Mineral deposits and Tectonics of two contrasting Geologic Environments in the Republic of the Philippines, Terminal report, pp. 83, Tokyo, Japan.

Karig, D.E. (1983) Accreted terranes in the northern part of the Philippine Archipelago. Tectonics, 2, 211–236.

Kuno, H. (1968) Differentiation of Basalt Magmas. In Basalts: The Poldervaart treatise on rocks of basaltic composition (Hess, H.H. and Poldervaart, A., Eds.). pp. 862, Interscience Publishers, New York and London, 623–688.

Liu, W.N., Li, C.F., Li, J., Fairhead, D. and Zhou, Z. (2014) Deep structures of the Palawan and Sulu Sea and their implications for opening of the South China Sea. Marine and Petroleum Geology, 58, 721–735.

Magro, G., Gherardi, F. and Bayon, F.E. (2013) Noble and reactive gases of Palinpinon geothermal field (Philippines): Origin, reservoir processes and geodynamic implications. Chemical Geology, 339, 4–15.

Militante-Matias, P.J., de Leon, M.M. and Marquez, E.J. (2000) Cretaceous environments of the Philippines. Developments in Palaeontology and Stratigraphy, 17, 181–199.

Miyashiro, A. (1974) Volcanic rock series in island arcs and active continental margins. American Journal of Science, 274, 321–355.

Morimoto, N. (1988) Nomenclature of Pyroxenes. American Mineralogist, 73, 1123–1133.

Nimis, P. and Taylor, W.R. (2000) Single clinopyroxene thermobarometry for garnet peridotites. Part I. Calibration and testing of a Cr-in-Cpx barometer and an enstatite-in-Cpx thermometer. Contributions to Mineralogy and Petrology, 139, 541–554.

Peña, R.E. (2008) Lexicon of Philippine Stratigraphy. The Geological Society of the Philippines, pp. 364, Mandaluyong, Philippines.

Peccerillo, A. and Taylor, S.R. (1976) Geochemistry of Eocene Calc-Alkaline Volcanic Rocks from the Kastamonu area, Northern Turkey. Contributions to Mineralogy and Petrology, 58, 63–81.

Pubellier, M., Aurelio, M. and Sautter, B. (2018) The life of a marginal basin depicted in a structural map of the South China Sea. Episodes, 41, 139–142.

Putirka, K., Johnson, M., Kinzler, R. and Walker, D. (1996) Thermobarometry of mafic igneous rocks based on clinopyroxene-liquid equilibria, 0-30 kbar. Contributions to Mineralogy and Petrology, 123, 92–108.

Putirka, K.D., Mikaelian, H., Ryerson, F. and Shaw, H. (2003) New igneous thermobarometers for mafic and evolved lava compositions, based on clinopyroxene + liquid equilibria. American Mineralogist, 88, 1542–1554.

Putirka, K.D. (2005) Igneous thermometers and barometers based on plagioclase + liquid equilibria: Tests of some existing models and new calibrations. American Mineralogist, 90, 336–346.

Putirka, K.D. (2008) Thermometers and Barometers for Volcanic Systems. Reviews in Mineralogy and Geochemistry, 69, 61–120.

Sajona, F.G., Maury, R.C., Pubellier, M., Leterrier, J., Bellon, H. and Cotten, J. (2000) Magmatic source enrichment by slab-derived melts in a young post-collision setting, central Mindanao (Philippines). Lithos, 54, 173–206.

Sugawara, T. (2001) Ferric iron partitioning between plagioclase and silicate liquid: thermodynamics and petrological applications. Contributions to Mineralogy and Petrology, 141, 659–686.

Suggate, S.M., Cottam, M.A., Hall, R., Sevastjanova, I., Forster, M.A., White, L.T., Armstrong, R.A., Carter, A. and Mojares, E. (2014). South China continental margin signature for sandstones and granites from Palawan, Philippines. Gondwana Research, 26, 699–718.

Taylor, B. and Hayes, D.E. (1980) The Tectonic Evolution of the South China Basin. The Tectonic and Geologic Evolution of Southeast Asian Seas and Islands. Geophysical Monograph, 23, 89–104.

Wilkinson, J.F.G. (1986) Classification and Average Chemical Compositions of Common Basalts and Andesites. Journal of Petrology, 27, 31–62.

Williams, H.H. (1997) Play concepts-northwest Palawan, Philippines. Journal of Asian Earth Sciences, 15, 251–273.

Wood, B.J. (1974) The solubility of alumina in orthopyroxene coexisting with garnet. Contributions to Mineralogy and Petrology, 46, 1–15.

Workman, R.K. and Hart, S.R. (2005) Major and trace element composition of the depleted MORB mantle (DMM). Earth and Planetary Science Letters, 231, 53–72.

Yang, H.J., Frey, F.A., Clague, D.A. and Garcia, M.O. (1996) Mineral chemistry of submarine lavas from Hilo Ridge, Hawaii: Implications for magmatic processes within Hawaiian rift zones. Contributions to Mineralogy and Petrology, 135, 355–372.

Yumul, G.P., Dimalanta, C.B., Marquez, E.J. and Queaño, K. L. (2009) Onland signatures of the Palawan microcontinental block and Philippine mobile belt collision and crustal growth process: A review. Journal of Asian Earth Sciences, 34, 610–62.

Akita University

Chapter 5: Conclusions

The Manguao Basalt is a large basaltic lava flow field located on the northern tip of Palawan Island, Philippines. Lava field exposures are excellently preserved nearshore, with lava flow features still intact in several locations. The apparent 'geomorphologically young' character of the lava flow seemingly contradicts the general tectonic framework of the Palawan Continental Block.

This study presented the occurrence of the Manguao Basalt lava flow field, provided detailed petrographic and geochemical analyses of the basaltic samples, characterized Manguao Basalt in terms of major and trace element geochemistry, and provided the first investigation of its mineral chemistry.

(1) Lava flow occurrence

The lava flow field is located on the northeastern end of Palawan Island. Lava field exposures are found in low-lying areas and channels, overlying cherts and clastic sedimentary rocks. Lava flow features and structures (e.g., levees, tumuli, and lava fronts) are preserved in nearshore exposures. The seemingly young geomorphic character of the lava flow appears to contradict the tectonic setting of the Palawan Continental Block (i.e., the aseismic nature of PCB and absence of nearby active trench).

(2) Petrography and Geochemistry

Manguao Basalt samples are vesicular and porphyritic, with observable phenocrysts (e.g., olivine and pyroxene) and xenoliths (e.g., chert). Olivine dominates the phenocryst assemblage with minor pyroxenes (orthopyroxenes and clinopyroxenes). The groundmass is plagioclase-dominated, with anhedral clinopyroxenes and glass filling the spaces between laths (intersertal textures). Mineral textures and relationships observed in thin sections show the earlier formation of the pyroxene phenocrysts compared to olivine (pyroxenes → olivine → plagioclase → groundmass pyroxenes). This unusual crystallization sequence was investigated using geochemistry and the MELTS program.

Major element geochemistry of Manguao Basalt samples shows compositions similar to common olivine tholeiite basalts of Wilkinson (1986). CIPW compositions show silica-saturation (to

oversaturation), as expected from the presence of numerous chert xenoliths. Manguao Basalt shows tholeiitic character in major element diagrams (i.e., subalkaline in TAS diagrams and characteristic early iron-enrichment in AFM). Fractionation of early-formed ferromagnesian minerals (e.g., olivine and pyroxene) and limited fractionation of later-formed minerals (e.g., plagioclase) are also reflected in the bivariate diagrams. Evidence from trace element geochemistry confirms the early olivine fractionation (i.e., Ni, and Co concentrations decreasing with lower MgO). Tectonic discrimination, using trace element diagrams, shows inconsistencies in associating Manguao Basalt with different tectonic settings (i.e., with 'within-plate' basalts, continental arc basalts, island arc basalts, and ocean island basalts). Trace element spider diagrams, however, were able to show: (1) the enriched character of Manguao Basalt, (2) the consistent positive anomalies in continent-derived trace elements (i.e., Th), and (3) the absence of the diagnostic negative anomalies in Nb and Ta.

The unusual crystallization sequence, inferred from petrographic observations, prompted the notion of further investigating the mineral chemistry of Manguao Basalt. The tholeiitic character from bulk compositions, fractionation of early-formed ferromagnesian minerals, and enriched melt character were the initial assumptions carried forth in conducting mineral chemistry investigation.

(3) Mineral Chemistry Study

Details on the mineral chemistry of Manguao Basalt components further expanded our understanding of the crystallization processes and magmatic conditions at depth. Simulations of mantle melting and crystallization using the MELTS program helped in further constraining the possible character of the mantle source, the conditions that induced its melting, and the processes inducing melt evolution.

Olivine and pyroxene (orthopyroxene and clinopyroxene) phenocrysts are the most magnesian (Mg# > 80) species found in Manguao Basalt. Magnesium number of modal components confirm the crystallization sequence inferred from petrography (orthopyroxene/clinopyroxene → olivine → plagioclase → clinopyroxene2). Compositional zoning in pyroxenes, previously unidentified in petrography, improved our understanding of the melt evolution prior to its emplacement on the surface.

Akita University

Pressure and temperature calculations from mineral and bulk chemistry data also provided supplementary information on the crystallization sequence during melt cooling.

Mineral-based thermometers are consistent with the idea of early pyroxene formation. The highest temperature of formation was obtained from orthopyroxene phenocrysts (1252 °C, average). Thermometers based on 'liquid-only' components show a different crystallization sequence (i.e., olivine having the highest average formation temperatures; 1256 °C). Highest pressure obtained from orthopyroxene barometer (~5 kbar) served as benchmark for the conditions during the initial stage of melt crystallization.

Simulations of source melting, evolution, and crystallization were done using the MELTS program of Ghiorso et al. (2002) and Ghiroso and Gualda (2015). Depressurization of fertile mantle source (composition of KLB-1 spinel lherzolite at starting pressures of 15 kbar, temperature of 1350 °C, and at QFM buffer) produced primitive melts that are saturated in pyroxene components (i.e., Mg and Ca). The corresponding melt evolution from crystallization of these melts at 5 kbar were able to reach compositional similarities with Manguao Basalt at 1230–1260 °C. The compositions of the orthopyroxenes from the simulations, however, showed some remarkable differences. Maintaining equilibrium between the melt and the early-formed minerals is critical for producing orthopyroxenes and clinopyroxenes with similar compositions found in Manguao Basalt.

A model for magmatic underplating is proposed for the origin of Manguao Basalt. The emplacement of large volumes of basaltic magma within the Moho allows for (1) maintaining equilibrium between the melt and its source, (2) keeping the magmatic conditions (e.g. pressure and melt-solid equilibrium) essential for the early pyroxene formation, and (3) providing the receptacle for fractionation until melt removal.

Implications on future studies of Manguao Basalt

The model for magmatic underplating beneath the Palawan microcontinent provides a general overview of the details on magmatic and crystallization processes during the formation of Manguao Basalt. This

Akita University

idea fits well with the current understanding of the regional tectonic setting of PCB (i.e., absence of subduction zones) and the connection with other magmatic units in the area [i.e., Capoas granite is reported to be a product of partial melting of crustal rocks, as a response to a 'widespread basaltic magmatism' post-spreading of the South China Sea; Encarnación and Mukasa, (2002)]. The validity of this model, however, is not yet investigated and discussed in the following aspects: (1) Magmatic underplating as response to cessation of SCS opening, (2) structural controls inducing volcanism in PCB, (3) and the connection of Manguao Basalt to other post-spreading SCS volcanic events. Further studies on the origin of Manguao Basalt would help in establishing a clearer view of the evolution of the Palawan Microcontinent and its relation to Philippines and the SCS geologic history.

APPENDICES

Table 1. Geothermometers and Geobarometers used in this study

Liquid-only based Equations

Helz and Thornber (1987): Ol Saturation Thermometer

$$T(°C) = 26.3MgO^{Liq} + 994.4$$

Helz and Thornber (1987) with Putirka (2008) modification: Ol Saturation Thermometer

(a) P-independent Thermometer

$$T(°C) = 754 + 190.6(Mg\#) + 25.52MgO^{Liq} + 9.585FeO^{Liq} + 14.87[(Na_2O) + (K_2O)]^{Liq} - 9.176H_2O^{Liq}$$

(b) P-dependent Thermometer

$$T(°C) = 815.3 + 265.5(Mg\#) + 15.37MgO^{Liq} + 8.61FeO^{Liq} + 6.646[(Na_2O) + (K_2O)]^{Liq} + 39.16P(GPa) - 12.83H_2C$$

Yang et al. (1996): Ol-Cpx-Pl Equilibrium of Liquid Thermometer (P-dependent)

$$T(°C) = -583 + 3141X_{SiO2}^{Liq} + 15779X_{Al2O3}^{Liq} + 1338.6X_{MgO}^{Liq} - 31440X_{SiO2}^{Liq}X_{Al2O3}^{Liq} + 77.67P(GPa)$$

Putirka (2008) based on Beattie (1993): P-dependent, Opx Saturation Thermometer

$$T(°C) = \{5573.8 + 587.9P(GPa) - 61[P(GPa)]^2\}/[5.3 - 0.633\ln(Mg\#) - 3.97C_{NM}^{L} + 0.06NF + 24.7(X_{CaO}^{Liq})^2 + 0.081H_2O^{Liq} + 0.156P(GPa)$$

Putirka (2008): Cpx Saturation Thermometer

$$\frac{10^4}{T(K)} = 6.39 + 0.076H_2O^{Liq} - 5.55X_{CaO}^{Liq}X_{SiO2}^{Liq} - 0.386\ln\left(X_{MgO}^{Liq}\right) - 0.046P(kbar) + 2.2x10^{-4}[P(kbar)]^2$$

Putirka (2005): Plagioclase Saturation Thermometer

$$\frac{10^4}{T(K)} = 10.86 - 9.7654X_{SiO2}^{Liq} + 4.241X_{CaO}^{Liq} - 55.56X_{CaO}^{Liq}X_{AlO1.5}^{Liq} + 37.50X_{KO0.5}^{Liq}X_{AlO1.5}^{Liq} + 11.206\left(X_{SiO2}^{Liq}\right)^3 - 3.151x10^{-2}[P(kbar)] + 0.1709H_2O^{Liq}$$

Olivine-based Equations

Arndt (1977): Nickel Partitioning in Olivine and Liquid Thermometer

$$T(°C) = \frac{10430}{\left[\ln\left(D_{NiO}^{Ol-Liq}\right) + 4.79\right]} - 273.15$$

Beattie (1993): Olivine-Liquid Thermometer (P-dependent), also liquid-only Thermometer

$$T(°C) = \{13603 + 4.943x10^{-7}[P(GPa)x10^9 - 10^5]\}/\left\{[6.26 + 2\ln D_{Mg}^{Ol-Liq} + 2\ln\left(1.5C_{NM}^{L}\right) + 2\ln\left(3C_{SiO2}^{L}\right) - NF]\right\} - 273.15$$

where $D_{Mg}^{Ol-Liq} = \frac{\left[0.666+0.049X_{MnO}^{Liq}-0.027X_{FeO}^{Liq}\right]}{\left[X_{MgO}^{Liq}+0.259X_{MnO}^{Liq}+0.299X_{FeO}^{Liq}\right]}$

Orthopyroxene-based Equations

Putirka (2008) based on Beattie (1993): P-dependent, Opx-Liq-based Thermometer

$$\frac{10^4}{T(°C)} = 4.07 - 0.329P(GPa) + 0.12H_2O^{Liq} + 0.567\ln\left[\frac{X_{Fm2Si2O6}^{Opx}}{\left(X_{SiO2}^{Liq}\right)^2\left(X_{FeO}^{Liq} + X_{MnO}^{Liq} + X_{MgO}^{Liq}\right)^2}\right] - 3.06X_{MgO}^{Liq} - 6.17X_{KO0.5}^{Liq} + 1.89(Mg\#) + 2.57X_{Fe}^{Opx}$$

Putirka (2008) based on Wood (1974): Al-in-orthopyroxene Barometers (a-c); (a-b) Opx-Liq, (c) Opx-only

$$\text{(a) } P(kbar) = -13.97 + 0.0129T(°C) + 0.001416T(°C)\ln\left[\frac{X_{NaAlSi2O6}^{Opx}}{X_{NaO0.5}^{Liq}X_{AlO1.5}^{Liq}\left(X_{SiO2}^{Liq}\right)^2}\right] - 19.64X_{SiO2}^{Liq} + 47.49X_{MgO}^{Liq} + 6.99X_{Fe}^{Opx} + 37.37X_{FmAl2SiO6}^{Opx} + 0.748H_2O^{Liq} + 79.67(X_{NaO0.5}^{Liq} + X_{KO0.5}^{Liq})$$

$$\text{(b) } P(kbar) = 1.788 + 0.0375T(°C) + 1.295x10^{-3}T(°C)\ln\left[\frac{X_{FmAl2SiO6}^{Opx}}{X_{FmO}^{Liq}\left(X_{AlO1.5}^{Liq}\right)^2X_{SiO2}^{Liq}}\right] - 33.42X_{AlO1.5}^{Liq} + 9.795(Mg\#) + 36.08\left(X_{NaO0.5}^{Liq} + X_{KO0.5}^{Liq}\right) + 0.784H_2O^{Liq} - 26.2X_{Si}^{Opx} + 14.21X_{Fe}^{Opx}$$

(c) $P(\text{kbar}) = 2064 + 0.321T(°C) - 343.4\ln[T(°C)] + 31.52X_{Al}^{Opx} - 12.28X_{Ca}^{Opx} - 290X_{Cr}^{Opx} + 1.54\ln(X_{Cr}^{Opx}) - 177.2(X_{Al}^{Opx} - 0.1715)^2 - 372(X_{Al}^{Opx} - 0.1715)(X_{Ca}^{Opx} - 0.0736)$

Clinopyroxene-based Equations

Putirka et al. (1996): Cpx-liquid

$$\frac{10^4}{T(K)} = 6.73 - 0.26\ln\left[\frac{X_{Jd}^{Cpx}X_{Ca}^{Liq}X_{Fm}^{Liq}}{X_{DiHd}^{Cpx}X_{Na}^{Liq}X_{Al}^{Liq}}\right] - 0.86\ln\left(\frac{X_{Mg}^{Liq}}{X_{Mg}^{Liq} + X_{Fe}^{Liq}}\right) + 0.52\ln(X_{Ca}^{Liq})$$

Putirka (2008) based on Nimis and Taylor (2000): Cpx-based Thermometer

$$T(K) = [93100 + 544P(\text{kbar})]/\{61.1 + 36.6X_{Ti}^{Cpx} + 10.9X_{Fe}^{Cpx} - 0.95(X_{Al}^{Cpx} + X_{Cr}^{Cpx} - X_{Na}^{Cpx} - X_{K}^{Cpx}) + 0.395[\ln(\alpha_{En}^{Cpx})]^2\}$$

Putirka (2008): Al-partitioning in Cpx-liquid

$$\frac{10^4}{T(K)} = 7.53 - 0.14\ln\left[\frac{X_{Jd}^{Cpx}X_{CaO}^{Liq}X_{Fm}^{Liq}}{X_{DiHd}^{Cpx}X_{Na}^{Liq}X_{Al}^{Liq}}\right] + 0.07H_2O^{Liq} - 14.9X_{CaO}^{Liq}X_{SiO2}^{Liq} - 0.08\ln(X_{TiO2}^{Liq}) - 3.62(X_{NaO0.5}^{Liq} + X_{KO0.5}^{Liq}) - 1.1(Mg\#) - 0.18\ln(X_{EnFs}^{Cpx}) - 0.027P(\text{kbar})$$

Plagioclase-based Equation

Putirka (2008) with calibration from Sugawara (2001) and Ghiorso et al. (2002): Pl Thermometer (P-dependent)

$$\frac{10^4}{T(K)} = 6.12 + 0.257\ln\left[\frac{X_{An}^{Pl}}{X_{CaO}^{Liq}(X_{AlO1.5}^{Liq})^2(X_{SiO2}^{Liq})^2}\right] - 3.166X_{CaO}^{Liq} - 3.137\left(\frac{X_{AlO1.5}^{Liq}}{X_{AlO1.5}^{Liq} + X_{SiO2}^{Liq}}\right) + 1.216(X_{Ab}^{Pl})^2 - 2.475\text{x}10^{-2}P(\text{kbar}) + 0.2166H_2O^{Liq}$$

Additional terms used in calculations:

X_Z^Y, Cation per formula unit – derived from cation fractions; Y, Mineral or Liquid Target; Z, Element or Oxide; D_{NiO}^{Ol-Liq}, Nickel partitioning between Ol and Liquid $D_{NiO}^{Ol-Liq} = \frac{X_{NiO}^{Ol}}{X_{NiO}^{Liq}}$; C_{NM}^{Liq}, Network-modifying cations of liquid (Putirka, 2008) as in Beattie (1993); $C_{NM}^{Liq} = C_{MgO}^{Liq} + C_{MnO}^{Liq} + C_{FeO}^{Liq} + C_{CaO}^{Liq} + C_{CoO}^{Liq} + C_{NiO}^{Liq}$; $C_{SiO2}^{Liq} = X_{SiO2}^{Liq}$; NF, Network Formers of Liquid (Putirka, 2008) as in Beattie (1993) $NF = \left(\frac{7}{2}\right)\ln(1 - X_{AlO1.5}^{Liq}) + 7\ln(1 - X_{TiO2}^{Liq})$; Pyroxene Components: $X_{Al(IV)}^{Opx} = 2 - X_{Si}^{Opx}$; $X_{Al(VI)}^{Opx} = X_{Al}^{Opx} - X_{Al(IV)}^{Opx}$; $X_{NaAlSi2O6}^{Opx} = X_{Al(VI)}^{Opx}$ or X_{Na}^{Opx}, whichever is less; $X_{FmTiAlSiO6}^{Opx} = X_{Ti}^{Opx}$; $X_{CrAl2SiO6}^{Opx} = X_{Cr}^{Opx}$; $X_{FmAl2SiO6}^{Opx} = X_{Al(VI)}^{Opx} - X_{NaAlSi2O6}^{Opx} - X_{CrAl2SiO6}^{Opx}$; $X_{CaFmSi2O6}^{Opx} = X_{Ca}^{Opx}$; $X_{Fm2Si2O6}^{Opx} = [(X_{Fe}^{Opx} + X_{Mn}^{Opx} + X_{Mg}^{Opx}) - X_{FmTiAlSiO6}^{Opx} - X_{FmAl2SiO6}^{Opx} - X_{CaFmSi2O6}^{Opx}]/2$

Table 2. Melt Evolution from Equilibrium Crystallization

T(°C)	Melt Composition during Equilibrium Crystallization (Equilibrium Melt from Fertile Source)						Melt Composition during Equilibrium Crystallization (Equilibrium Melt from Depleted Source)					
	wt% SiO_2	wt% TiO_2	wt% FeO^t	wt% MgO	wt% CaO	Mg#	wt% SiO_2	wt% TiO_2	wt% FeO^t	wt% MgO	wt% CaO	Mg#
1320	49.27	0.54	7.02	12.67	13.38	76.29	48.08	0.65	7.17	13.24	14.19	76.72
1310	49.15	0.55	7.01	12.28	13.60	75.75	47.95	0.66	7.16	12.86	14.44	76.21
1300	48.92	0.60	7.12	11.61	13.20	74.41	47.64	0.72	7.27	12.23	14.14	74.99
1290	48.75	0.64	7.19	10.88	12.71	72.98	47.41	0.78	7.35	11.53	13.74	73.66
1280	48.71	0.69	7.18	10.14	12.21	71.57	47.36	0.85	7.30	10.78	13.34	72.48
1270	48.83	0.74	7.09	9.38	11.69	70.21	46.77	1.26	8.24	10.12	12.82	68.64
1260	48.51	1.03	7.95	8.73	10.83	66.19	45.80	1.88	9.49	9.65	12.35	64.47
1250	48.17	1.28	8.68	8.18	10.05	62.68	44.96	2.45	10.24	9.26	11.97	61.74
1240	48.01	1.47	9.17	7.64	9.34	59.77	44.28	2.93	10.55	8.91	11.64	60.11
1230	48.15	1.73	9.51	7.00	8.74	56.74	43.70	3.31	10.54	8.60	11.33	59.26
1220	48.54	1.99	9.40	6.34	8.17	54.61	43.47	4.00	10.28	8.07	11.15	58.33
1210	49.39	2.18	8.56	5.62	7.58	53.93	43.51	4.62	9.65	7.52	10.92	58.15
1200	50.62	2.30	7.11	4.85	6.91	54.85	-	-	-	-	-	-
	Melt Composition during Equilibrium Crystallization (Fractional Melt from Fertile Source)						Melt Composition during Equilibrium Crystallization (Fractional Melt from Depleted Source)					
T(°C)	wt% SiO_2	wt% TiO_2	wt% FeO^t	wt% MgO	wt% CaO	Mg#	wt% SiO_2	wt% TiO_2	wt% FeO^t	wt% MgO	wt% CaO	Mg#
1320	46.96	0.64	7.29	12.58	13.40	75.46	46.21	0.77	7.49	13.66	14.92	76.49
1310	47.03	0.65	7.26	12.19	13.54	74.95	46.28	0.78	7.46	13.27	15.09	76.03
1300	47.11	0.65	7.23	11.81	13.68	74.44	45.94	0.83	7.65	12.74	14.81	74.82
1290	46.87	0.69	7.40	11.20	13.23	72.95	45.51	0.91	7.92	12.15	14.29	73.24
1280	46.64	0.74	7.60	10.52	12.57	71.15	45.30	1.01	8.18	11.52	13.66	71.52
1270	46.64	0.79	7.76	9.80	11.82	69.25	45.41	1.22	8.62	10.75	12.85	68.97
1260	47.05	0.84	7.84	8.99	10.90	67.16	44.85	1.68	10.00	10.13	12.09	64.36
1250	47.39	0.94	8.35	8.16	9.93	63.53	44.22	2.18	11.21	9.56	11.51	60.33
1240	47.62	1.05	8.96	7.39	9.03	59.54	43.64	2.70	12.13	9.03	11.06	57.04
1230	47.94	1.11	9.37	6.68	8.20	55.96	43.25	3.22	12.54	8.48	10.69	54.67
1220	48.37	1.12	9.58	6.01	7.43	52.80	43.54	3.66	11.91	7.77	10.28	53.76
1210	48.88	1.09	9.59	5.40	6.72	50.08	-	-	-	-	-	-
1200	49.46	1.03	9.41	4.84	6.08	47.82	-	-	-	-	-	-

Table 3. Melt evolution from Fractional Crystallization

	Melt Composition during Fractional Crystallization (Equilibrium Melt from Fertile Source)						Melt Composition during Fractional Crystallization (Equilibrium Melt from Depleted Source)					
T(°C)	wt% SiO_2	wt% TiO_2	wt% FeO^t	wt% MgO	wt% CaO	Mg#	wt% SiO_2	wt% TiO_2	wt% FeO^t	wt% MgO	wt% CaO	Mg#
1320	48.80	0.53	7.98	12.66	13.16	73.88	47.63	0.64	8.12	13.24	13.96	74.40
1310	48.68	0.54	8.00	12.28	13.38	73.25	47.48	0.65	8.14	12.86	14.20	73.81
1300	48.41	0.58	8.15	11.63	13.17	71.78	47.15	0.69	8.30	12.26	14.06	72.48
1290	48.10	0.62	8.35	10.87	12.80	69.88	46.76	0.75	8.52	11.53	13.77	70.71
1280	47.85	0.67	8.54	10.14	12.38	67.92	46.43	0.81	8.72	10.83	13.43	68.87
1270	47.64	0.71	8.71	9.44	11.94	65.89	45.67	1.04	9.98	10.35	12.74	64.90
1260	46.97	0.92	10.17	9.01	11.00	61.22	44.19	1.51	12.43	9.96	12.13	58.82
1250	46.07	1.18	11.87	8.56	10.29	56.25	42.82	1.96	14.71	9.62	11.57	53.83
1240	45.20	1.42	13.43	8.17	9.64	52.03	41.76	2.39	16.78	9.17	11.04	49.36
1230	44.46	1.66	14.96	7.77	9.04	48.07	40.86	2.82	18.70	8.70	10.55	45.35
1220	43.85	1.90	16.50	7.32	8.50	44.15	40.02	3.23	20.51	8.26	10.09	41.80
1210	43.41	2.12	17.84	6.86	7.97	40.69	39.24	3.62	22.22	7.84	9.66	38.62
1200	43.04	2.33	19.09	6.43	7.47	37.52	38.52	4.00	23.81	7.43	9.26	35.76
	Melt Composition during Fractional Crystallization (Fractional Melt from Fertile Source)						Melt Composition during Fractional Crystallization (Fractional Melt from Depleted Source)					
T(°C)	wt% SiO_2	wt% TiO_2	wt% FeO^t	wt% MgO	wt% CaO	Mg#	wt% SiO_2	wt% TiO_2	wt% FeO^t	wt% MgO	wt% CaO	Mg#
1320	46.43	0.63	8.28	12.58	13.21	73.02	45.69	0.76	8.47	13.64	14.71	74.17
1310	46.50	0.64	8.26	12.19	13.35	72.45	45.76	0.77	8.45	13.25	14.87	73.66
1300	46.57	0.64	8.24	11.81	13.49	71.87	45.52	0.81	8.63	12.77	14.72	72.52
1290	46.38	0.67	8.41	11.27	13.20	70.48	45.02	0.88	9.00	12.19	14.22	70.73
1280	46.05	0.72	8.72	10.61	12.57	68.46	44.61	0.96	9.36	11.56	13.71	68.78
1270	45.79	0.76	9.01	9.97	11.93	66.37	44.53	1.13	10.15	10.77	12.97	65.41
1260	45.93	0.82	9.29	9.12	11.18	63.64	44.11	1.48	11.92	10.19	11.99	60.38
1250	46.29	0.92	10.02	8.39	10.13	59.90	43.20	1.92	13.95	9.61	11.38	55.10
1240	46.30	1.07	11.08	7.73	9.26	55.42	42.33	2.35	15.86	9.09	10.83	50.52
1230	46.25	1.22	12.12	7.11	8.51	51.12	41.50	2.76	17.67	8.61	10.31	46.49
1220	46.19	1.36	13.09	6.55	7.83	47.14	40.71	3.16	19.38	8.17	9.83	42.91
1210	46.13	1.49	14.00	6.04	7.22	43.46	39.96	3.54	21.01	7.76	9.38	39.69
1200	46.07	1.62	14.87	5.57	6.67	40.04	39.27	3.92	22.57	7.37	8.95	36.78

Table 4. Evolution of Ol composition during equilibrium crystallization

	Ol Composition during Equilibrium Crystallization (Equilibrium Melt from Fertile Source)					Ol Composition during Equilibrium Crystallization (Equilibrium Melt from Depleted Source)				
T (°C)	wt% SiO_2	wt% FeO^t	wt% MgO	wt% CaO	Mg#	wt% SiO_2	wt% FeO^t	wt% MgO	wt% CaO	Mg#
1240	39.73	14.39	44.25	0.39	84.58	38.76	16.02	39.98	0.40	81.65
1230	39.48	15.37	43.17	0.38	83.36	38.52	16.42	38.94	0.39	80.87
1220	39.26	16.23	42.21	0.38	82.26	38.37	16.63	38.28	0.38	80.40
1210	39.10	16.85	41.51	0.37	81.45	38.25	17.15	37.74	0.37	79.69
1200	39.02	17.17	41.16	0.35	81.03	38.11	17.83	37.13	0.36	78.79
1190	39.01	17.22	41.12	0.34	80.98	37.96	18.52	36.50	0.36	77.85
1180	38.88	17.81	40.58	0.33	80.25	37.88	18.86	36.13	0.35	77.35
1170	38.75	18.53	39.98	0.32	79.37	37.83	18.94	35.93	0.33	77.18
1160	38.70	18.72	39.77	0.31	79.11	37.78	19.01	35.73	0.32	77.02
1150	38.67	18.82	39.63	0.30	78.97	37.74	19.07	35.53	0.31	76.86
1140	38.63	18.90	39.50	0.29	78.84	37.69	19.13	35.32	0.30	76.70
1130	38.60	18.98	39.36	0.28	78.71	37.64	19.17	35.10	0.29	76.55
	Ol Composition during Equilibrium Crystallization (Fractionated Melt from Fertile Source)					Ol Composition during Equilibrium Crystallization (Fractionated Melt from Depleted Source)				
T (°C)	wt% SiO_2	wt% FeO^t	wt% MgO	wt% CaO	Mg#	wt% SiO_2	wt% FeO^t	wt% MgO	wt% CaO	Mg#
1240	39.99	13.68	45.36	0.42	85.53	39.75	14.37	44.34	0.41	84.62
1230	39.81	14.54	44.58	0.41	84.53	39.47	15.43	43.11	0.40	83.28
1220	39.65	15.32	43.88	0.40	83.63	39.20	16.37	41.94	0.39	82.04
1210	39.51	15.99	43.28	0.40	82.83	38.99	17.07	41.02	0.39	81.07
1200	39.39	16.55	42.78	0.39	82.17	38.90	17.36	40.62	0.37	80.66
1190	39.30	17.00	42.39	0.38	81.64	38.88	17.41	40.53	0.36	80.58
1180	39.23	17.33	42.09	0.38	81.24	38.86	17.41	40.45	0.34	80.56
1170	39.18	17.57	41.88	0.37	80.95	38.77	17.74	40.08	0.33	80.11
1160	39.15	17.74	41.73	0.36	80.75	38.68	18.12	39.66	0.32	79.60
1150	39.12	17.85	41.62	0.35	80.61	38.62	18.25	39.42	0.31	79.39
1140	39.11	17.92	41.56	0.34	80.52	38.56	18.36	39.18	0.30	79.18
1130	39.10	17.96	41.52	0.33	80.48	38.51	18.47	38.93	0.29	78.98

Table 5. Evolution of Pl composition during equilibrium crystallization

	Pl Composition during Equilibrium Crystallization (Equilibrium Melt from Fertile Source)						Pl Composition during Equilibrium Crystallization (Equilibrium Melt from Depleted Source)					
T (°C)	wt% SiO_2	wt% Al_2O_3	wt% CaO	wt% Na_2O	wt% K_2O	An%	wt% SiO_2	wt% Al_2O_3	wt% CaO	wt% Na_2O	wt% K_2O	An%
1250	49.51	32.38	15.16	2.90	0.04	74.11	47.03	34.06	17.12	1.76	0.02	84.18
1240	50.18	31.93	14.63	3.20	0.06	71.42	47.22	33.93	16.97	1.85	0.03	83.40
1230	50.84	31.48	14.11	3.48	0.09	68.74	47.34	33.85	16.88	1.89	0.04	82.93
1220	51.42	31.08	13.64	3.72	0.14	66.41	47.34	33.85	16.88	1.88	0.06	82.92
1210	51.86	30.77	13.28	3.88	0.21	64.61	47.32	33.85	16.88	1.86	0.08	82.96
1200	52.13	30.56	13.05	3.95	0.31	63.44	47.32	33.85	16.88	1.85	0.10	82.97
1190	52.15	30.55	13.04	3.96	0.31	63.38	47.32	33.85	16.88	1.85	0.10	82.96
1180	52.18	30.53	13.01	3.97	0.31	63.25	47.32	33.84	16.88	1.85	0.10	82.94
1170	52.20	30.51	13.00	3.98	0.31	63.17	47.33	33.84	16.88	1.85	0.10	82.93
1160	52.23	30.50	12.97	3.99	0.31	63.06	47.33	33.84	16.87	1.85	0.10	82.92
1150	52.26	30.47	12.95	4.01	0.31	62.93	47.33	33.84	16.87	1.85	0.10	82.91
1140	52.29	30.45	12.92	4.02	0.32	62.79	47.33	33.84	16.87	1.86	0.10	82.90
1130	49.51	32.38	15.16	2.90	0.04	74.11	47.03	34.06	17.12	1.76	0.02	84.18
	Pl Composition during Equilibrium Crystallization (Fractionated Melt from Fertile Source)						Pl Composition during Equilibrium Crystallization (Fractionated Melt from Depleted Source)					
T (°C)	wt% SiO_2	wt% Al_2O_3	wt% CaO	wt% Na_2O	wt% K_2O	An%	wt% SiO_2	wt% Al_2O_3	wt% CaO	wt% Na_2O	wt% K_2O	An%
1250	49.15	32.63	15.45	2.73	0.05	75.58	47.43	33.79	16.81	1.95	0.02	82.58
1240	49.90	32.12	14.85	3.07	0.06	72.55	47.81	33.53	16.51	2.11	0.04	81.01
1230	50.64	31.62	14.27	3.39	0.08	69.58	48.08	33.34	16.29	2.22	0.06	79.90
1220	51.36	31.13	13.70	3.71	0.11	66.67	48.24	33.22	16.15	2.27	0.11	79.20
1210	52.06	30.65	13.14	4.02	0.14	63.85	48.34	33.15	16.07	2.29	0.16	78.80
1200	52.73	30.19	12.60	4.31	0.17	61.14	48.36	33.13	16.05	2.30	0.16	78.69
1190	53.37	29.74	12.09	4.59	0.21	58.57	48.39	33.11	16.02	2.31	0.16	78.56
1180	53.98	29.33	11.60	4.84	0.25	56.14	48.43	33.09	16.00	2.33	0.16	78.41
1170	54.55	28.93	11.14	5.08	0.30	53.85	48.47	33.06	15.96	2.34	0.16	78.25
1160	55.09	28.55	10.70	5.29	0.36	51.68	48.51	33.03	15.93	2.36	0.17	78.09
1150	55.60	28.20	10.29	5.50	0.42	49.63	48.55	33.01	15.90	2.38	0.17	77.93
1140	56.09	27.85	9.89	5.68	0.48	47.67	48.58	32.98	15.87	2.39	0.17	77.78
1130	56.56	27.52	9.51	5.86	0.55	75.58	48.62	32.96	15.84	2.41	0.17	77.64

Table 6. Summary of mineral compositions from Manguao Basalt and MELTS simulations (Opx and Ol)

	Opx			Ol				
wt% oxide	Manguao Basalt Opx (ave)	Fertile-EqMelting Opx	Dep-EqMelting Opx	Manguao Basalt Ol (ave)	Fertile-EqMelting Ol	Fertile-FrMelting Ol	Depleted-EqMelting Ol	Depleted-FrMelting Ol
SiO_2	54.75	53.20–56.19	52.92–55.99	38.68	36.99–39.73	38.56–40.91	36.13–38.76	36.56–40.83
TiO_2	0.39	0.03–0.33	0.03–0.42	0.02	-	-	-	-
Al_2O_3	1.48	2.52–4.35	2.82–4.72	0.01	-	-	-	-
FeO^t	11.68	6.22–13.53	6.25–13.49	18.86	14.39–20.05	9.04–20.65	16.02–19.76	9.45–20.11
MnO	0.23	-	-	0.23	1.24–10.51	0.19–1.43	4.84–15.47	0.21–12.80
MgO	28.82	27.93–33.13	27.91–33.06	41.41	32.33–44.25	39.28–49.35	28.50–39.98	30.40–48.99
CaO	2.08	0.93–2.34	0.90–2.24	0.18	0.12–0.39	0.09–0.52	0.13–0.40	0.12–0.52
Na_2O	0.04	0.02–0.05	0.01–0.03	0.01	-	-	-	-
K_2O	0.01	-	-	-	-	-	-	-
Cr_2O_3	0.39	-	-	0.04	-	-	-	-

Table 6. Summary of mineral compositions from Manguao Basalt and MELTS simulations (Cpx and Pl)

	Cpx						Pl				
wt% oxide	Mg# >80 (ave)	Mg# <80 (ave)	Fertile-EqMelting Cpx	Fertile-FrMelting Cpx	Depleted-EqMelting Cpx	Depleted-FrMelting Cpx	Manguao Basalt Pl (ave)	Fertile-EqMelting Pl	Fertile-FrMelting Pl	Depleted-EqMelting Pl	Depleted-FrMelting Pl
SiO_2	52.71	52.47	49.04–52.75	48.30–51.27	48.22–52.42	48.25–51.49	54.19	48.80–52.93	49.15–58.77	46.36–47.35	46.34–48.91
TiO_2	0.67	0.91	0.09–1.10	0.19–1.15	0.10–1.43	0.16–1.36	0.14	-	-	-	-
Al_2O_3	1.91	1.91	4.41–7.48	5.91–8.36	4.82–7.75	5.66–7.96	27.87	30.01–32.86	25.98–32.63	33.83–34.51	32.76–34.53
FeO^t	6.73	11.74	5.72–12.71	4.54–7.32	5.78–8.28	4.76–8.42	0.64	-	-	-	-
MnO	0.18	0.30	-	-	-	-	0.01	-	-	-	-
MgO	17.59	20.43	13.74–23.12	13.18–17.40	13.69–20.69	13.55–18.20	0.16	-	-	-	-
CaO	19.01	11.50	6.52–21.44	19.31–20.74	15.98–22.01	16.61 – 21.81	11.4	12.41–15.73	7.72–15.45	16.86–17.65	15.61–17.67
Na_2O	0.24	0.16	0.16–0.62	0.23–0.99	0.11–0.34	0.13 – 0.44	4.74	2.58–4.30	2.73–6.72	1.46–1.89	1.45–2.53
K_2O	-	0.01	-	-	-	-	0.31	0.03–0.35	0.05–0.81	0.01–0.11	0.01–0.19
Cr_2O_3	0.67	0.26	-	-	-	-	-	-	-	-	-